Large neutral amino acid levels tune perinatal neuronal excitability and survival

Graphical abstract

Highlights

- The cerebral cortex undergoes metabolic reprogramming throughout development

- Large neutral amino acids are essential for the perinatal neuronal metabolic state

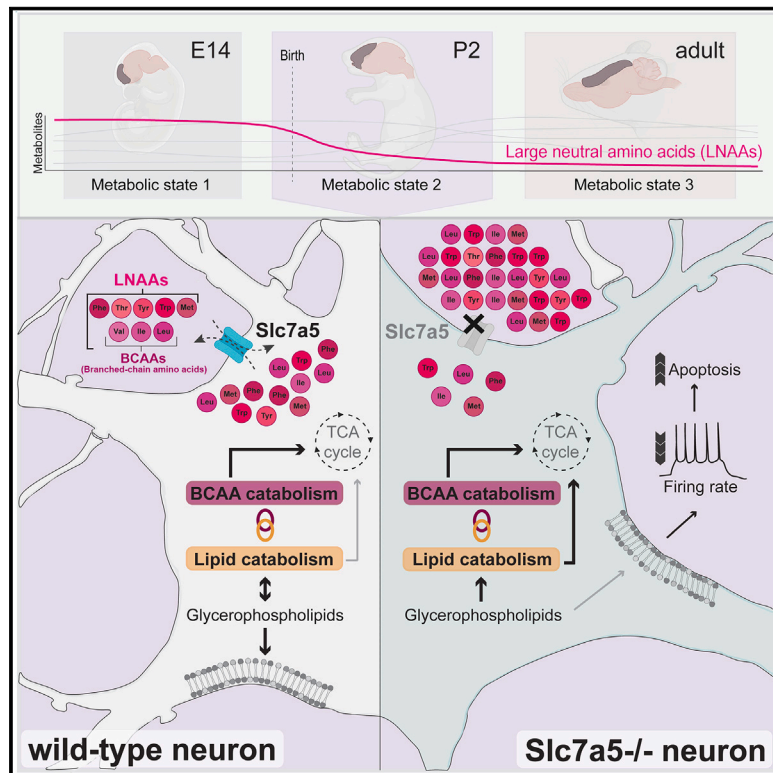- Deleting Slc7a5 in neurons links branched-chain amino acids and lipid metabolism

- Reduced large neutral amino acid levels alter neuronal excitability and survival

Authors

Lisa S. Knaus, Bernadette Basilico, Daniel Malzl, ..., Jörg Menche, Simon Hippenmeyer, Gaia Novarino

Correspondence

gaia.novarino@ista.ac.at

In brief

Metabolic profiling of the developing cerebral cortex reveals an essential role of large neutral amino acids in modulating the neuronal metabolic state, excitability, and survival at perinatal stages.

CellPress

Article

Large neutral amino acid levels tune perinatal neuronal excitability and survival

Lisa S. Knaus,[1] Bernadette Basilico,[1,7] Daniel Malzl,[2,7] Maria Gerykova Bujalkova,[3] Mateja Smogavec,[3] Lena A. Schwarz,[1] Sarah Gorkiewicz,[1] Nicole Amberg,[1] Florian M. Pauler,[1] Christian Knittl-Frank,[4] Marianna Tassinari,[1] Nuno Maulide,[4,5] Thomas Rülicke,[6] Jörg Menche,[2] Simon Hippenmeyer,[1] and Gaia Novarino[1,8,*]

[1]Institute of Science and Technology Austria (ISTA), Am Campus 1, 3400 Klosterneuburg, Austria
[2]Max Perutz Labs, Dr.-Bohr-Gasse 9, 1030 Vienna, Austria
[3]Institute of Medical Genetics, Medical University of Vienna, Währinger Straße 10, 1090 Vienna, Austria
[4]Institute of Organic Chemistry, University of Vienna, Währinger Strasse 38, 1090 Vienna, Austria
[5]University of Vienna, Research Platform NeGeMac, Währinger Strasse 38, 1090 Vienna, Austria
[6]University of Veterinary Medicine Vienna, Veterinärplatz 1, 1210 Vienna, Austria
[7]These authors contributed equally
[8]Lead contact
*Correspondence: gaia.novarino@ista.ac.at
https://doi.org/10.1016/j.cell.2023.02.037

SUMMARY

Little is known about the critical metabolic changes that neural cells have to undergo during development and how temporary shifts in this program can influence brain circuitries and behavior. Inspired by the discovery that mutations in SLC7A5, a transporter of metabolically essential large neutral amino acids (LNAAs), lead to autism, we employed metabolomic profiling to study the metabolic states of the cerebral cortex across different developmental stages. We found that the forebrain undergoes significant metabolic remodeling throughout development, with certain groups of metabolites showing stage-specific changes, but what are the consequences of perturbing this metabolic program? By manipulating Slc7a5 expression in neural cells, we found that the metabolism of LNAAs and lipids are interconnected in the cortex. Deletion of Slc7a5 in neurons affects the postnatal metabolic state, leading to a shift in lipid metabolism. Additionally, it causes stage- and cell-type-specific alterations in neuronal activity patterns, resulting in a long-term circuit dysfunction.

INTRODUCTION

Human cortical development entails the timely coordination of a number of steps that are devised to generate a precise range of correctly positioned and functionally integrated neuronal cells. These steps are guided and regulated by a network of genes whose mutations can underlie neurodevelopmental and neuropsychiatric disorders.[1] Challenging environmental conditions may also account for pathological variations of neurodevelopment but the identification of such factors is complicated and less understood.[2–5] Genetic conditions, however, offer tractable entry points to isolate some of the extrinsic factors influencing the assembly of the brain.

We recently identified mutations in the gene *SLC7A5*, encoding a large neutral amino acid (LNAA) transporter (LAT1), as a rare cause of autism spectrum disorders.[6] Most of the LNAAs are essential; thus, their presence in the human body depends on dietary intake. However, it remains largely unknown whether and how the level of these amino acids (AAs) changes over time in the brain and how fluctuations in their amount may influence the course of neurodevelopment. In fact, little is known

about the metabolic program unfolding during brain development and the specific nutrient dependencies that this entails. For example, there are little data on how brain metabolism changes immediately after birth. This period is interesting since the brain undergoes a series of maturation processes while the organism has to adapt to new feeding and environmental conditions. Understanding how specific nutrients can influence brain maturation may be key in preventing or correcting aspects of certain neurodevelopmental conditions.

Here, we profiled the metabolome of the mouse cerebral cortex at various developmental stages, thereby defining significant longitudinal changes. Based on these results, we identified a perinatal time window when the forebrain exhibits an increased dependency on LNAAs. Thus, we studied the effect of perturbing the perinatal metabolic state by limiting the amount of these essential AAs in neural cells. In doing so, we identified a pivotal and unexpected function of LNAAs during a temporal window crucial for cortical network refinement. Precisely, we found that altering the levels of LNAAs in cortical neurons changes their lipid metabolism along with excitability and survival probability in a cell-autonomous manner, specifically early after birth. Our
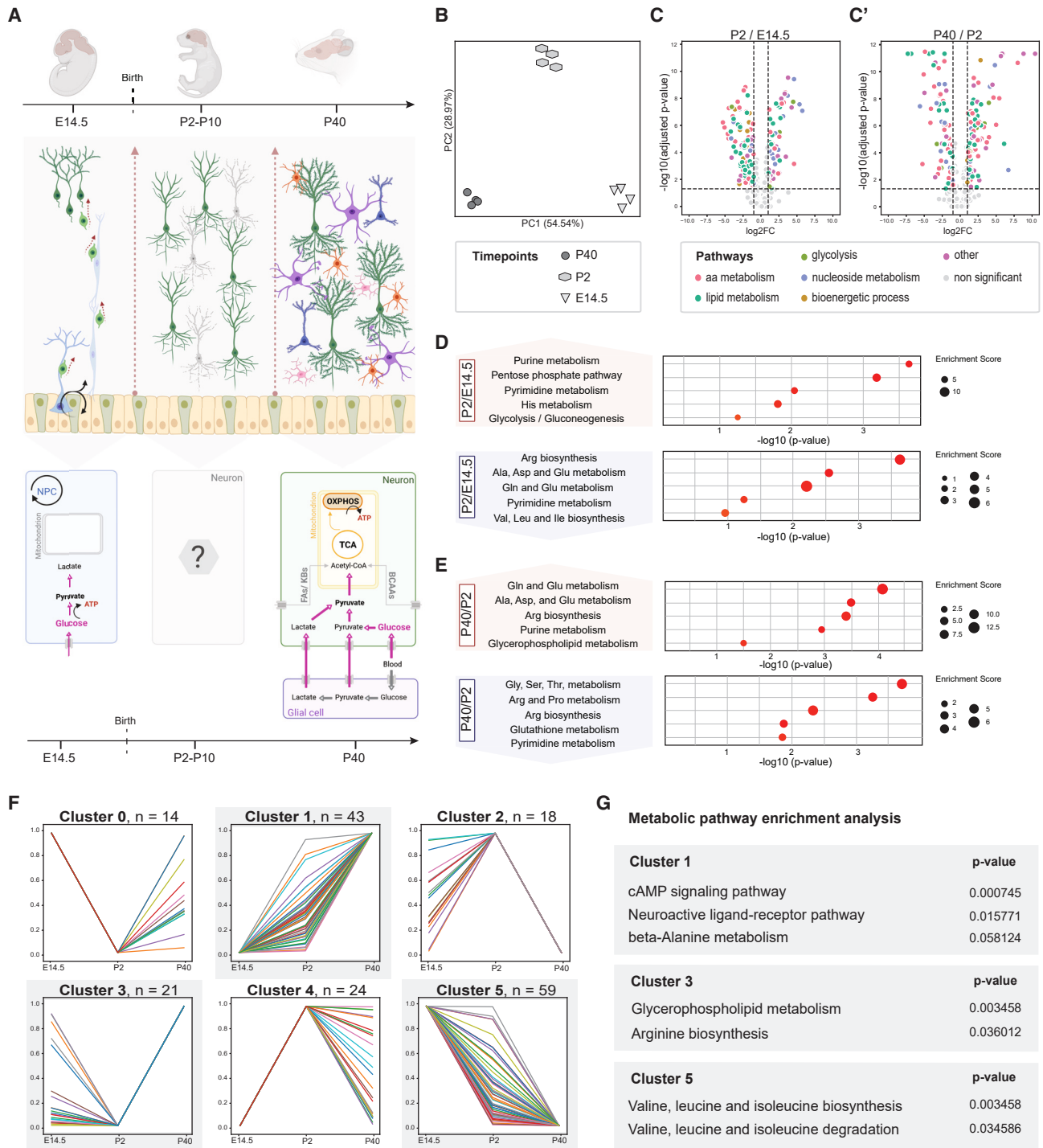
Figure 1. Metabolome profiling of the forebrain across time highlights developmental stage-specific metabolic states

(A) Schematic description of ATP synthesis strategies in the cortex at different developmental stages. Top left: at E14.5, neural progenitor cells (NPCs) produce intermediate progenitors and migrating immature excitatory neurons, generating the different cortical layers. Bottom left: for ATP synthesis, NPCs rely on anaerobic glycolysis, a cytoplasmic biochemical process converting glucose into lactate. Top middle: perinatally, the cortical network, mainly consisting of maturing excitatory and inhibitory neurons, undergoes significant refinement. Glial cells are detectable but immature. Bottom middle: the metabolic landscape of maturing neurons is largely unknown. Top right: a mature cortical network, including pyramidal (green), inhibitory neurons (blue) and glial cells (astrocytes [purple], oligodendrocytes [orange] and microglia [pink]). Bottom right: mature neurons utilize glucose to produce ATP via aerobic glycolysis. Since endogenous pyruvate is insufficient to meet energy demand, neurons depend on metabolic support by glial cells (TCA, tricarboxylic acid cycle; OXPHOS, oxidative phosphorylation).

(legend continued on next page)

results offer a model of how mammalian neurons coordinate the expression of a nutrient-associated gene with the regulation of neuronal activity to ensure proper brain development. Altering these processes during a limited but critical time window results in permanent cortical circuit defects.

RESULTS

Metabolome profiling reveals distinctive metabolic states of the cerebral cortex across development

Little is known about the metabolic program adopted by the maturing brain. For example, we know that neural progenitor cells (NPCs) mainly rely on anaerobic glycolysis (Figure 1A left).[7,8] In contrast, mature neurons meet their ATP demand through oxidative phosphorylation (OXPHOS) (Figure 1A right), but due to their high energy requirement and their inability to store glycogen,[9,10] they rely on astrocytes to provide metabolic support.[11,12] However, it is unknown how maturing neurons meet their energy demand at intermediate developmental stages when they lack full glial support (Figure 1A middle).

To gain an understanding of the metabolic states and transitions occurring during brain maturation, we analyzed the metabolome of the wild-type mouse cerebral cortex obtained at three different time points: embryonic day 14.5 (E14.5), postnatal day 2 (P2), and postnatal day 40 (P40). These time points coincide with different feeding strategies and are enriched for neural cells in different states: NPCs and immature (E14.5), maturing (P2), and mature (P40) neurons (Figure 1A). By employing two independent high-performance liquid chromatography (HPLC) detection strategies (see STAR Methods), we quantified 346 metabolites. Principal-component analysis (PCA) of the results separated the samples based on sampling age (Figure 1B), indicating that the cerebral cortex at each of these three time points is in a distinct metabolic state. The metabolic reorganization of the developing cortex is extensive, with the level of 273 out of 346 metabolites changing over time (Figures 1C and 1C′). The variability across animals of the same age was small (Figure S1A), indicating that the observed changes are tightly regulated. Compared with E14.5, at P2, the level of 137 metabolites is significantly decreased and that of 60 increased (Figure 1C). At P40, 202 metabolites show a different level than at P2, with an approximately equal number of metabolites showing increased or decreased levels (Figure 1C′). Enrichment analysis revealed an overrepresentation of purine- and pentose phosphate-related metabolites among those increasing at P2 (compared with E14.5) and enrichment of AA-related metabolites among those decreasing (Figure 1D). At P40, we detected a substantial increase in glutamine and glutamate-related metabolites and a

decrease in a different set of AAs (Figure 1E), disclosing a stage-specific regulation of AA metabolism. To better understand the quality of these changes over time, we plotted the developmental trajectories of the detected metabolites (Figure S2 gray trajectories; Data S1). Employing a Gaussian mixture model (GMM), we clustered all measured metabolites based on their time trajectories. Next, focusing on Kyoto Encyclopedia of Genes and Genomes (KEGG)-annotated metabolites (n = 179) (Figure 1F), we assessed whether different trajectory-related groups were enriched for particular classes of metabolites (Figure 1G; Data S2). This analysis revealed a predictable enrichment for neuroactive and cAMP signaling pathways in the cluster representing metabolites with ascending trajectories over time (cluster 1, Figures 1F and 1G), with the majority of the metabolites steeply increasing between P2 and P40. Furthermore, we found that cluster 5, comprising metabolites with declining trajectories over time, is enriched for branched-chain AAs (BCAAs) and BCAA-related metabolites (Figures 1F and 1G). This cluster sparked our interest since BCAAs are substrates of the SLC7A5 transporter. The decline over time of these and a few other AAs (i.e., Figure S2; gray trajectories, metabolite [M] 016, M017, M030, M062, and M086) could indicate either a decreasing brain intake or an increasing utilization by neural cells as they mature. Either way, this observation further suggests that neural cells have distinctive AA demands at different developmental stages. Finally, the only other cluster enriched for specific classes of metabolites is cluster 3, which displays a drop in glycerophospholipid (GPL)- and arginine-related metabolite levels, specifically at P2 (Figures 1F and 1G).

Perturbation of LNAA uptake leads to perinatal disruption of lipid metabolism

Knowing that the level of BCAAs and BCAA-related metabolites changes during brain maturation, we investigated the consequences of limiting BCAA supply to neural cells. Therefore, we ablated *Slc7a5*, the main LNAA transporter, in these cells. Indeed, although Slc7a5 has been described as a blood-brain barrier (BBB) transporter,[6] we found that, in the cerebral cortex, it is also expressed in excitatory neurons and glial cells of all layers, particularly perinatally (Figures 2A–2C′, S1B, and S1C), coinciding with the time window displaying a drop in BCAA levels (Figures 1F and 1G cluster 5). In addition, while patients with *SLC7A5* mutations present with microcephaly, the deletion of *Slc7a5* from the BBB in mice (*Slc7a5fl/fl;Tie2-Cre* positive [+] mice) does not lead to a reduction in brain size.[6] This suggests a function of *SLC7A5*, and its substrates, in cell types other than the endothelial cells of the BBB. Thus, we crossed floxed *Slc7a5* mice (*Slc7a5fl*) with *Emx1*-Cre animals. *Emx1*-Cre mice

(B) Principal-component analysis of the metabolome of E14.5, P2, and P40 wild-type mouse cortices.

(C and C′) Volcano plots showing differentially abundant metabolites across developmental stages.

(D and E) Metabolic pathway enrichment analysis of all significantly upregulated (red) or downregulated (blue) metabolites at P2 compared with E14.5 (D) and P40 compared with P2 (E).

(F) Clustering of all metabolites based on their trajectory over time; (x axis: age; y axis: scaled abundance).

(G) Metabolic pathway enrichment analysis (Data S2) revealed an overrepresentation of metabolites related to "cAMP signaling pathway" (p < 0.00075; adj-p < 0.021), "β-alanine metabolism" (p < 0.059; adj-p < 0.4) and "neuroactive ligand-receptor pathway" (p < 0.016; adj-p < 0.22) in cluster 1. Cluster 3 is enriched for "glycerophospholipid metabolism" (p < 0.013; adj-p < 0.24) and "arginine biosynthesis" (p < 0.037; adj-p < 0.25). Cluster 5 is enriched for "valine, leucine, and isoleucine biosynthesis (p < 0.0035; adj-p < 0.22) and -degradation" (p < 0.035; adj-p < 0.89).

See also Figures S1 and S2.
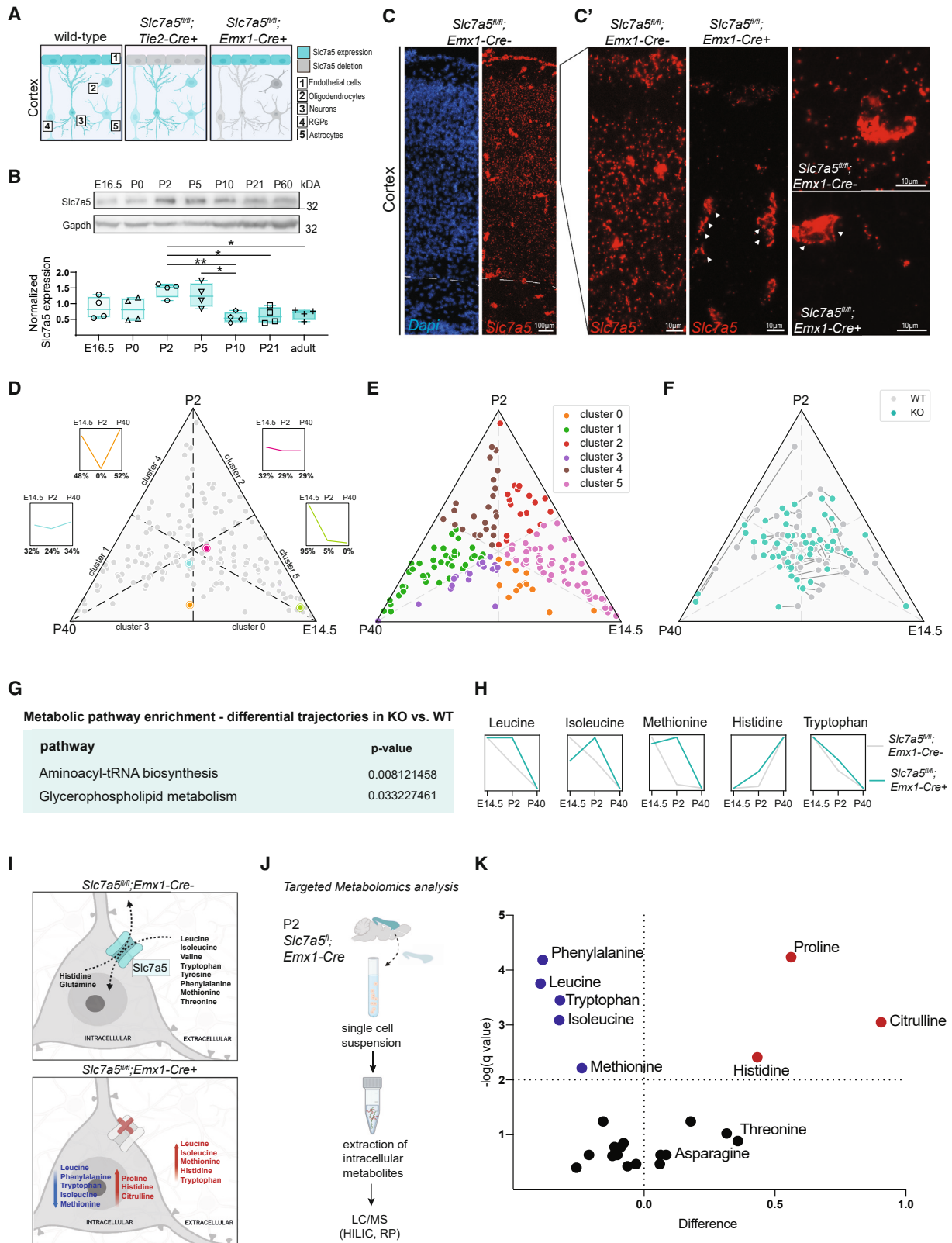
express the Cre recombinase in the radial glial cells of the dorsal telencephalon from E9.5 onward,[13] thereby inducing *Slc7a5* deletion in NPCs and their progeny, including the excitatory neurons of the neocortex and hippocampus as well as in the glial cells of the pallium (Figures 2A and S1D), but not in the endothelial cells of the BBB (Figure 2C'). Next, we analyzed the metabolome of the cerebral cortex of *Slc7a5^{fl/fl}*;*Emx1-Cre+* mice over time and compared it with that of wild-type animals. This approach allowed us to resolve (1) the cause of the drop in LNAAs (particularly BCAAs) observed in P2 wild-type cortical lysates (Figure S2, gray trajectories M016, M017, M030, M062, and M086) and (2) the impact of deregulating these AAs on the metabolism of the cerebral cortex. The effect of *Slc7a5* deletion on the overall metabolite profile is relatively minimal (Figure S1E). To investigate whether *SLC7A5* mutations affect specific groups of metabolites, we performed an enrichment analysis of the KEGG-annotated metabolites showing divergent temporal trajectories (r < 0.975) in mutants and controls (Figures 2D–2H and S2; Data S1 and S2). As expected, this analysis identified the pool of AAs transported by Slc7a5, grouped into the term "aminoacyl-tRNA biosynthesis" (Figure 2G), as the major class of affected metabolites in mutant animals. However, the deletion of *Slc7a5* alters the levels of these AAs in cortical tissue only at P2 (Figure 2H), indicating a function of Slc7a5 in neonatal mice.

Furthermore, the level of these AAs is higher, not lower, in mutants compared with controls (Figure 2H), suggesting that in the absence of Slc7a5, the LNAAs accumulate in the extracellular space and are not consumed by neural cells (Figure 2I). To test this possibility, we quantified AAs in neural cells isolated from P2 control and mutant cortices (Figure 2J), thereby measuring their intracellular amount. Indeed, the levels of the primary Slc7a5 substrates are significantly reduced in mutant cells. In contrast, the level of histidine, the counter AA,[14] is increased (Figure 2K). Thus, the lack of Slc7a5 at P2 impairs the transport of LNAAs into neural cells resulting in their net decreased consumption. These results also indicate that the drop in AA levels observed in P2 control samples (Figure 2H) reflects an increased utilization by neural cells.

Although the BCAAs are a source of acetyl-CoA, an essential compound for the tricarboxylic acid (TCA) cycle,[15] we observed only a very mild reduction in the levels of some of the energy storage- and transfer-related metabolites (Figures S3A–S3F), suggesting compensatory mechanisms. Indeed, while a derailment of energy homeostasis has been associated with increased levels of oxidative stress,[16–18] the ratio between reduced and oxidized glutathione was not altered in *Slc7a5*-mutant cells (Figure S3G). Further, the decrease in intracellular LNAAs does not lead to defects in AA sensing and protein synthesis pathways, such as the mammalian target of rapamycin (mTOR), the adenosine-monophosphate-activated protein kinase (AMPK), or the unfolded protein response (UPR) signaling cascades (Figure S4).[19–24]

However, we found that loss of *Slc7a5* in neurons affects the levels of metabolites related to "GPLs" (Figure 2G; Data S2). Specifically, a PCA of all the detected lipid-related metabolites disclosed that while at E14.5 and P40 mutant and control samples cluster together, P2 samples separate by genotype (Figure S3H), thereby suggesting a time-point-specific alteration in lipid composition due to the loss of *Slc7a5*, but how are BCAA and lipid metabolism linked? To better comprehend how a change in BCAA levels can disrupt lipid metabolism, we first identified the exact lipid classes affected by *Slc7a5* deletion. Thus, we performed a comparative untargeted lipidomic analysis of P2 *Slc7a5^{fl/fl}*;*Emx1-Cre+* and *Slc7a5^{fl/fl}*;*Emx1-Cre−* cortical tissue and dissociated cells (Data S3). These analyses revealed a specific reduction of GPLs in mutant cortical cells, along with an increase of triacylglycerols (TGs) in *Slc7a5* deficient cortical tissue (Figures 3A and 3B). Members of the GPLs are the main components of the phospholipid bilayer of biological membranes.[25] TGs, on the other hand, account for the majority of dietary fats and represent a way to store energy.[26] Sites of TG synthesis and storage are the liver and adipose tissue,[27,28] but they can be mobilized rapidly in case of energy or fatty acid (FA) demand by the brain.[29,30] To determine whether detected alterations are specific to any cell type, we compared our results with a dataset of human cortical cell-type-specific lipids.[31] Interestingly, several of the lipids differentially abundant in Slc7a5 mutants are neuron enriched, while astrocyte-enriched lipids are not affected in mutants (Figure 3C).

Next, to uncover the molecular mechanisms underlying the alterations in the cortical lipid profile, we performed a comparative

Figure 2. The neonatal metabolic state is dependent on *Slc7a5* expression

(A) *Slc7a5* expression in the cerebral cortex of wild-type (left), *Slc7a5^{fl/fl}*;*Tie2-Cre+* (middle), or *Slc7a5^{fl/fl}*;*Emx1-Cre+* (right) mice.

(B) Gapdh-normalized Slc7a5 levels in cortical samples obtained from *Slc7a5^{fl/fl}*;*Tie2-Cre+* animals across development (n = 4 mice per genotype per time point; *p < 0.05; **p < 0.01; unpaired two-tailed t test).

(C and C') *Slc7a5* mRNA expression in P2 murine wild-type somatosensory cortex (SSCtx) (C and C' [left]). In *Slc7a5^{fl/fl}*;*Emx1-Cre+* SSCtx (C' [right]), *Slc7a5* expression is preserved at the BBB (arrows) (scale bars, 100 μm and 10 μm).

(D–F) Ternary plot classification of metabolites in wild-type and mutant cortex. (D) The localization of each metabolite (dot) within the ternary plot is determined by its previously determined cluster affiliation (Figure 1F) and its exact unscaled trajectory, defined as the ratio between the three time points. (E) Ternary plot of KEGG-annotated metabolites in wild-type mice. (F) Compared with controls (gray dots), mutants display changes in the trajectory of some metabolites (cyan dots).

(G) Metabolic pathway enrichment analysis of the KEGG-annotated metabolites displaying an altered trajectory in mutants (Data S2).

(H) Stage-specific accumulation of Slc7a5 substrates in *Slc7a5^{fl/fl}*;*Emx1-Cre+* cortical tissue (n = 4 animals per genotype per time point; Pearson's coefficient: Data S1; x axis: age; y axis: scaled abundance).

(I) Slc7a5 facilitates the flux of BCAAs and LNAAs across the neuronal membrane (top). Loss of *Slc7a5* causes extracellular accumulation and intracellular depletion of LNAAs (bottom).

(J) Experimental workflow of the targeted intracellular metabolomic analysis.

(K) Volcano plot of the AAs measured in *Slc7a5* mutant and control cells. AAs showing significantly lower (blue) or higher (red) levels in *Slc7a5^{−/−}* cells are indicated (n = 7 per genotype; FDR cutoff: 1%).

See also Figures S1 and S2.
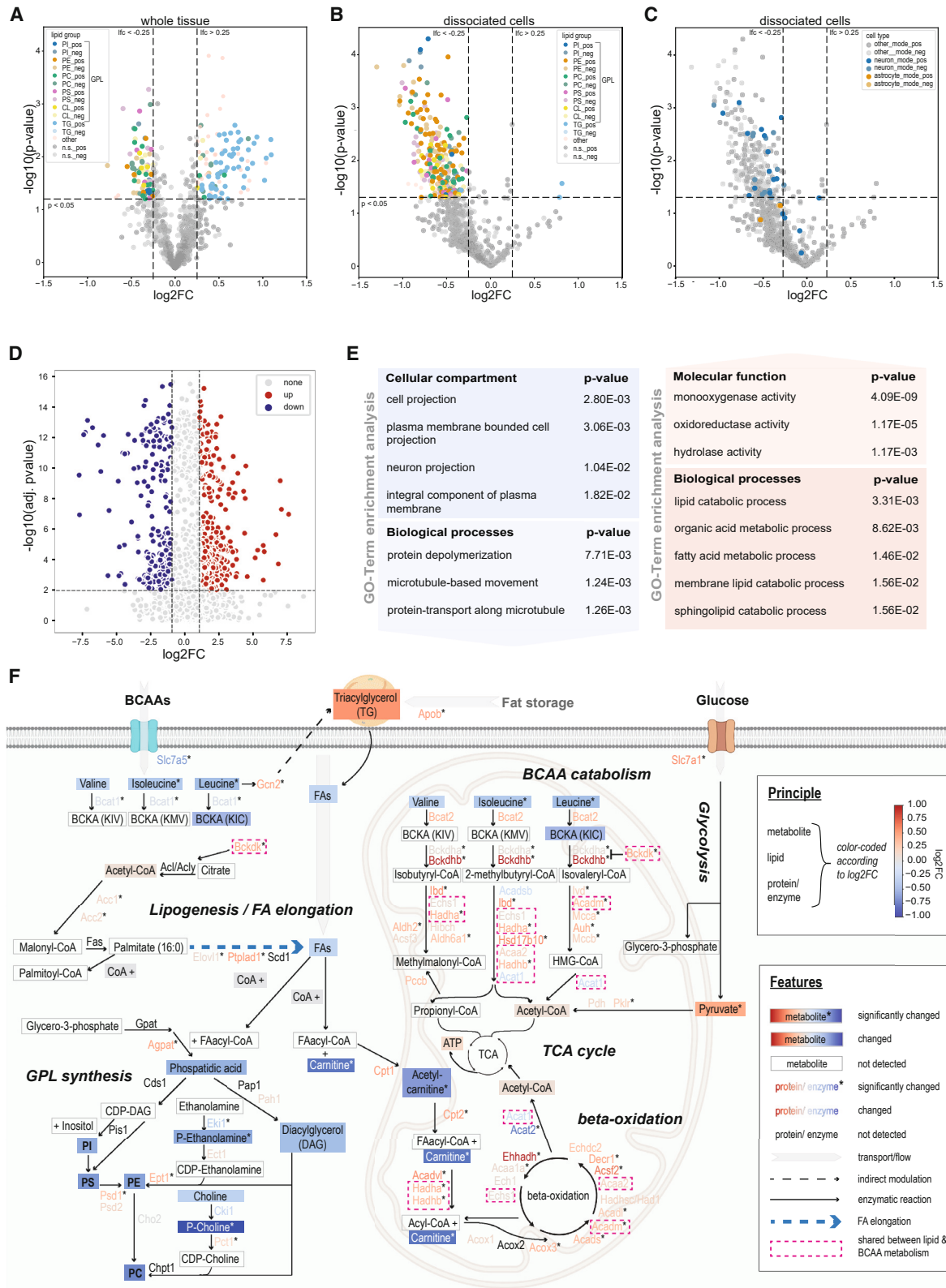
(legend on next page)

proteomic study of perinatal control and mutant cerebral cortices (Figures 3D and S3I). We identified 1,202 proteins deregulated in mutant samples, comprising 954 upregulated and 248 downregulated proteins in the *Slc7a5*$^{fl/fl}$;*Emx1-Cre+* cortex (Figure 3D). Gene ontology (GO) enrichment analysis returned proteins involved in lipid metabolism as being the most significant and numerous among the upregulated proteins (Figure 3E right), while among the downregulated GO terms, we found an enrichment for neuron projection and membrane-associated proteins (Figure 3E left; Data S4). Those GO terms were reproducible at the mRNA expression level (Figure S3J; Data S5) and linked to the reduction of GPLs[32] (Figures 3A and 3B). Importantly, we did not observe changes in the B1/B3 integrin signaling cascade.[33] Indeed, a co-immunoprecipitation experiment of Slc7a5 from neural cells, while confirming its interaction with Slc3a2,[34] excluded interactions with components of the B1/B3 integrin pathway (Data S6).

Finally, to identify the connection between BCAA and GPL metabolism, we integrated the proteomic, lipidomic, and metabolomic results focusing on potential convergent pathways (Figure 3F). Via this integration, we recognized that *Slc7a5* mutant cells, probably due to the shortage of BCAAs, prioritize mitochondrial BCAA catabolism, part of the ATP production machinery, over cytoplasmic BCAA catabolic reactions (i.e., Bcat2 vs. Bcat1; Figure 3F). Most importantly, about half of the enzymes involved in BCAA metabolism in the mitochondria are also involved in FA β-oxidation, thereby disclosing a molecular overlap between BCAA and lipid catabolism (Figure 3F). The reduction of the intracellular BCAA levels leads to a compensatory upregulation of several of these shared enzymes (e.g., Acaa2, Acadm, and Echs1), thereby increasing FA β-oxidation and causing a drop in FAs. These results suggest that neurons at the perinatal stage rely on BCAAs as substrates for ATP production (Figure S3K). In their absence, FAs are redirected from GPL synthesis into β-oxidation (Figure 3F). The observed increase in tissue TGs reflects the increased demand for FAs to support β-oxidation and ATP production. Indeed, the increase of TGs in mutant cortical tissue is accompanied by the upregulation of Gcn2 and Apob. Gcn2 is a kinase acting as a sensor for intracellular BCAA levels.[35] Low levels of BCAAs induce Gcn2 autophosphorylation, resulting in the inhibition of its protein turnover.[36,37] Interestingly, Gcn2 has also been involved in the mobilization of TGs from fat storage in response to brain energy demand.[30,38] Apob constitutes the primary lipoprotein transporting dietary lipids across tissues.[39] Finally, *Slc7a5* mutants also show an increased level of Bckdk, a regulator of the BCAA cata-

bolic pathway also implicated in the phosphorylation of cytoplasmic Acl, a key enzyme in citrate-based lipogenesis.[40]

These findings suggest an increased perinatal dependency of neural cells on LNAAs. Decreased availability of these AAs reveals a direct link between BCAAs and lipid metabolism in the brain.

Lack of the AA transporter SLC7A5 leads to stage-specific neuronal cell loss

Can the perinatal metabolic shift displayed by *Slc7a5* mutant neural cells explain some clinical issues reported in patients? *Slc7a5*$^{fl/fl}$;*Emx1-Cre+* mice are born at Mendelian ratios, are viable and at birth do not display obvious growth defects compared with their wild-type littermates (i.e., *Slc7a5*$^{fl/fl}$;*Emx1-Cre−* or *Slc7a5*$^{fl/+}$;*Emx1-Cre+* mice) (Figure S5A). In agreement with *Slc7a5* expression profile (Figure S1B) and the AA profile, which changes only postnatally, *Slc7a5*$^{fl/fl}$;*Emx1-Cre+* mutants are born with normal brain size (Figures S5B and S5C), indicating that *Slc7a5* is dispensable in the NPCs of the forebrain. Thus, *SLC7A5* mutations do not lead to microcephaly by hindering the generation of an appropriate number of neurons. However, by P40, the brain of *Slc7a5*$^{fl/fl}$;*Emx1-Cre+* mice is significantly smaller than that of their control littermates (Figures 4A, 4A′, and S5D). Histological analysis revealed a reduction in the thickness of the cerebral cortex of P40 *Slc7a5*$^{fl/fl}$;*Emx1-Cre+* animals (Figures 4B and 4B′), with layers II and III being the drivers of this difference (Figures S5E–S5G′). By monitoring the brain weight over time, we found that the difference in brain size between control and *Slc7a5* mutant animals appears during the first postnatal week (Figure 4C) and remains stable from P10 onward, coinciding with the increased *Slc7a5* expression levels in neural cells perinatally (Figures 2A and 2B). This time course supports a temporal dependence of *Slc7a5* function in postnatal neurodevelopment. To test whether the phenotype reflects an increase in postnatal neural cell death, we assessed the protein level of cleaved (Cl)-caspase-3, a pro-apoptotic marker, on cortical samples obtained from control and mutant mice across development. Compared with controls, mutants show a significant increase in Cl-caspase-3, specifically at P2 and P5 (Figure 4D). In line with the reduction of layers II–III thickness (Figures S5E–S5G′), most apoptotic cells are localized in the upper cortical layers (Figures S5H and S5I). Importantly, the period affected by the surge in Cl-caspase-3 levels corresponds to the phase of programmed cell death targeting cortical excitatory neurons. This is an innate process required to refine the number of neurons in the cerebral cortex.[41] Specifically, to obtain a calibrated

---

Figure 3. BCAA deprivation alters neuronal lipid metabolism

(A and B) Volcano plots of deregulated lipids in *Slc7a5* mutant cortical tissue (A) and dissociated cells (B). Lipids showing significantly lower or higher levels are color-coded according to their annotated class (PI, phosphatidylinositol; PE, phosphatidylethanolamine; PC, phosphatidylcholine; PS, phosphatidylserine; CL, cardiolipin; TG, triacylglycerol; _pos, detected in positive mode; _neg, detected in negative mode; n = 5 per genotype; p value cutoff: 0.05; Data S3).

(C) Same plot as in (B) with neuron-enriched (blue) or astrocyte-enriched lipids (orange) highlighted (Data S3).

(D) Volcano plot of proteins deregulated (1% false discovery rate (FDR) cutoff) in the P5 *Slc7a5*$^{fl/fl}$;*Emx1-Cre+* cortex.

(E) GO-term enrichment analysis of up- and downregulated proteins at 2% FDR (Data S4).

(F) Integration of the proteomic, metabolomic, and lipidomic data of P2 cortical tissue and cells. The schematic depicts enzymes associated with the metabolic pathways: "BCAA catabolism," "FA degradation" (β-oxidation), "FA synthesis/elongation," "glycolysis," and "glycerophospholipid synthesis." Changes in expression or abundance due to *Slc7a5* depletion are color-coded (blue: decreased; red: increased; *p < 0.05). Enzymes shared by the BCAA and FA pathways are highlighted by a dashed rectangle.
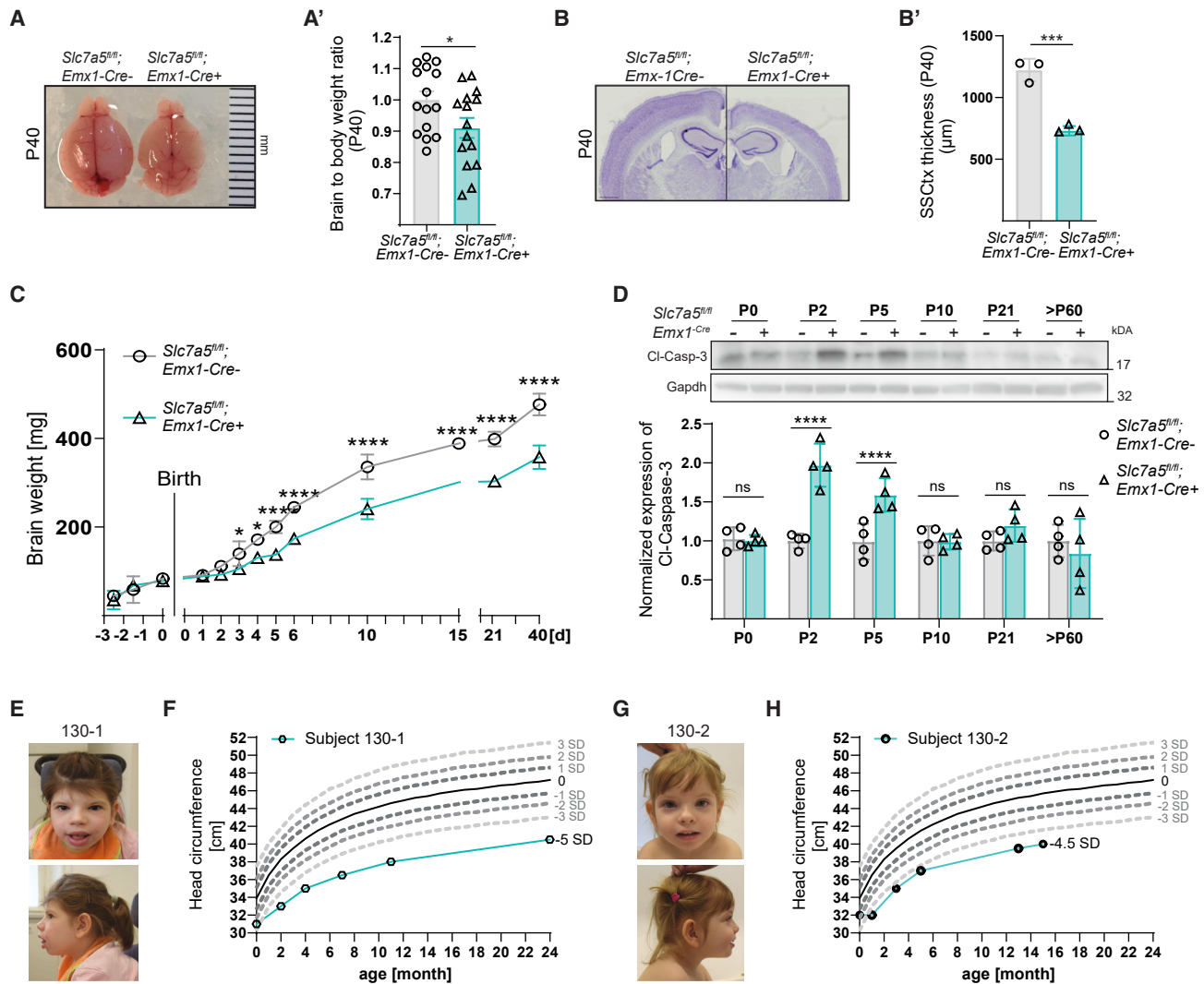
See also Figures S3 and S4.

Figure 4. *Slc7a5* mutations cause postnatal microcephaly

(A) Pictures of adult *Slc7a5^{fl/fl};Emx1-Cre+* and control brains. (A′) Brain-to-body weight ratio of adult *Slc7a5^{fl/fl};Emx1-Cre+* mice and littermate controls (means ± SEM; n = 15 mice per genotype; *p < 0.05; unpaired two-tailed t test).

(B and B′) Representative images (B) and quantification (B′) of Nissl-stained coronal sections of P40 mutant and control SSCtx (means ± SD; n = 3 littermates per genotype; ***p < 0.001; unpaired two-tailed t test; scale bar, 1,500 μm).

(C) *Slc7a5^{fl/fl};Emx1-Cre+* mice develop postnatal microcephaly during the first 10 days after birth (means ± SD; n ≥ 3 littermates per genotype/time point; *p < 0.05; ***p < 0.001; ****p < 0.0001; multiple unpaired two-tailed t test).

(D) Gapdh-normalized cleaved-caspase-3 expression in mutant and wild-type cortex across development (means ± SD; n = 4 mice per genotype time point; ^{ns}p > 0.05; ****p < 0.00001; multiple unpaired two-tailed t test).

(E and G) Frontal and lateral images of patient 130-1 and 130-2, diagnosed with *SLC7A5* compound heterozygous pathogenic variants.

(F and H) Measurements of the head circumference of the two patients showing the progression of microcephaly.

See also Figure S5 and Table S1.

network, cortical neurons are generated in excess and subsequently eliminated by two waves of apoptosis, one of which occurs early after birth. Additionally, previous studies have shown that to obtain an optimal pyramidal/inhibitory neuron ratio, the wave of apoptosis affecting cortical excitatory neurons around P5 is followed by an adjustment in the number of inhibitory neurons.[42] Thus, although *Slc7a5^{fl/fl};Emx1-Cre+* mice only lack *Slc7a5* expression in the excitatory neurons of the forebrain, the number of inhibitory cells might be indirectly affected.

Indeed, compared with their littermate controls, adult *Slc7a5^{fl/-fl};Emx1-Cre+* animals have a significantly lower number of inhibitory neurons, particularly in the upper cortical layers (Figures S5J and S5K). In contrast, non-neuronal cells are unaffected (Figures S5L–S5O), indicating that *Slc7a5* is important specifically for neuronal functions.

Next, we asked whether the critical temporal window identified in mice is also sensitive to the loss of *SLC7A5* function in humans. Thus, having identified patients with mutations in

SLC7A5, we measured their head size for several weeks from birth on (Figures 4E–4H). Patients 130-1 and 130-2 are siblings from a non-consanguineous family presenting with the clinical feature of SLC7A5 deficiency (Figure S5P). Trio-whole exome sequencing (WES) analysis of both siblings and their parents identified compound heterozygous pathogenic variants in the SLC7A5 gene: the previously described and functionally assessed missense variant c.1124C>T, p.(Pro375Leu)[6] and a novel intragenic deletion of exons 5 to 10. Parents are heterozygous carriers. Patient 130-1 showed microcephaly at birth (−3 SD). The microcephaly progressively worsened to −5 SD at the age of 7 months (Figure 4F). The clinical history and presentation of the younger sibling, patient 130-2, are essentially similar. A mild microcephaly was diagnosed at birth (−2.5 SD), progressively deteriorating to −4.5 SD at the age of 6–7 months (Figure 4H). The phenotypic comparison of published patients[6] revealed that the constant features associated with biallelic pathogenic SLC7A5 variants include microcephaly, developmental and motor delay, seizures, and autistic features (Table S1). Notably, the pathological variants identified in patients are mostly missense mutations that impact the transport capacity, not the expression, of the transporter.[6] Thus, the human data indicate that the transport of SLC7A5 substrate is key to the patient's clinical presentation. Therefore, SLC7A5 mutations likely result in decreased BCAA uptake and lead to microcephaly during the period of cortical refinement and programmed cell death in mice and humans.

Pyramidal neuron loss is due to cell-autonomous deficiency of Slc7a5

Next, we investigated whether Slc7a5-deficiency-linked neuronal cell death is due to a cell-autonomous or non-cell-autonomous effect. Assessing this was important, especially since in the absence of Slc7a5 AAs accumulate in the extracellular space, which could be harmful to the tissue. To perform a quantitative assessment, we used the mosaic analysis with double markers (MADM) system, which enables concurrent fluorescent labeling and gene knockout in sparse single-cell clones in vivo.[43,44] Specifically, two reciprocally chimeric marker genes (GT and TG alleles) are targeted to identical loci upstream of Slc7a5. The marker genes are part of the so-called MADM cassette (M8), which consists of split coding sequences for eGFP and tdTomato fluorescent proteins interspaced by a loxP site (Figure S6). Following Cre-recombinase-mediated interchromosomal recombination, the sequence for eGFP and tdTomato are reconstituted. Due to an innately low stochastic interchromosomal recombination rate, the green (eGFP+), red (tdTomato+), and yellow (eGFP+/tdTomato+) labeling are confined to individual sparse clones. In our experimental setup, the Cre recombinase expression is coupled with the Emx-1 promotor. This facilitates MADM labeling and deletion of Slc7a5 in single telencephalic radial glia progenitors (RGPs) and their progeny (Figure 5A), thereby generating cortex-specific genetic mosaics. To analyze potential cell-autonomous effects of the loss of Slc7a5 in the developing neocortex, we assessed the relative abundance of green (eGFP, Slc7a5−/−) and red (tdTomato, Slc7a5+/+) excitatory neurons at different time points of postnatal development (P0, P5, and P40) in mosaic-MADM (MADM-8$^{GT/}$

^{TG,Slc7a5};Emx1-Cre+) and control-MADM (MADM-8$^{GT/TG}$;Emx1-Cre+) animals (Figures 5B–5D'). While at P0 we did not observe significant changes in the ratio of green to red cells (Figures 5B and 5B'), supporting that Slc7a5 deficiency does not affect the proliferative phase of cortical development, by P5, there are significantly fewer Slc7a5−/− than Slc7a5+/+ excitatory neurons (Figures 5C and 5C'). Further, mosaic-MADM animals present fewer Slc7a5−/− (green) neurons in upper cortical layers (LII–LIV) compared with control (red) cells, while neurons in the lower layers (LV and LVI) are not affected by Slc7a5 deletion. The same analysis done at P40 revealed a slightly more profound reduction of mutant neuronal cells in mosaic-MADM cortices (Figures 5D and 5D'). We concluded that the deletion of Slc7a5 leads to a cell-autonomous increase in neuronal cell loss immediately after birth.

LNAA-dependent metabolic reprogramming controls neuronal excitability in neonatal mice

What mechanisms could underlie the stage- and cell-type-specific phenotype observed in Slc7a5$^{fl/fl}$;Emx1-Cre+ mice? Considering that neuronal excitability can determine the survival of cortical pyramidal cells during the postnatal wave of programmed cell death,[41,42] we hypothesized that abnormal AA and lipid metabolism might ultimately lead to changes in excitability. Indeed, alterations in neuronal lipid composition, especially in GPLs, can directly affect membrane formation and structure.[25] Furthermore, protein-lipid interactions and post-translational modifications can modulate the clustering and activity of many ion channels.[45–48] In particular, palmitoylation, a FA-dependent posttranslational modification mediated by palmitoyltransferases, is an important regulatory mechanism in neurons.[49–51] Indeed, we found that three palmitoyltransferases are deregulated in Slc7a5 mutants (Figure S7A). These include Zdhhc17, which specifically modifies proteins involved in neuronal functions. Additionally, approximately half of the downregulated proteins associated with the GO-term "integral component of the plasma membrane" (Figure 3E) are regulated by palmitoylation. Among these, we found Ank2, which is palmitoylated to support membrane scaffolding of the voltage-gated sodium channel Nav1.2[52]; Kcnd2, a potassium channel involved in the regulation of action potential (AP) backpropagation[53,54]; and Snap25, one of the top targets of Zdhhc17 involved in various neuronal functions[55,56] (Figure S7A). Thus, we assessed the intrinsic excitability of layers II and III pyramidal neurons from the somatosensory cortex (SSCtx) of mutant and control animals at P6–P7 by performing whole-cell current-clamp recordings while applying a series of current steps to elicit APs. Recordings from Slc7a5$^{fl/fl}$;Emx1-Cre+, Slc7a5^{fl+};Emx1-Cre+ and wild-type littermates revealed a substantial reduction in neuronal firing in Slc7a5$^{fl/fl}$;Emx1-Cre+ animals (Figures 6A, S7B, and S7C). Since both metabolic abnormalities and reduced neuronal survival in Slc7a5$^{fl/fl}$;Emx1-Cre+ mice are limited to the first days after birth, we performed current-clamp recordings at P25–P26 to assess whether the neuronal excitability defect is restricted to the same time window. Indeed, at P25–P26 Slc7a5$^{fl/fl}$;Emx1-Cre+ samples are indistinguishable from controls (Figures 6B and S7D), underscoring the importance of Slc7a5 in modulating neuronal excitability early after birth. While the transient nature
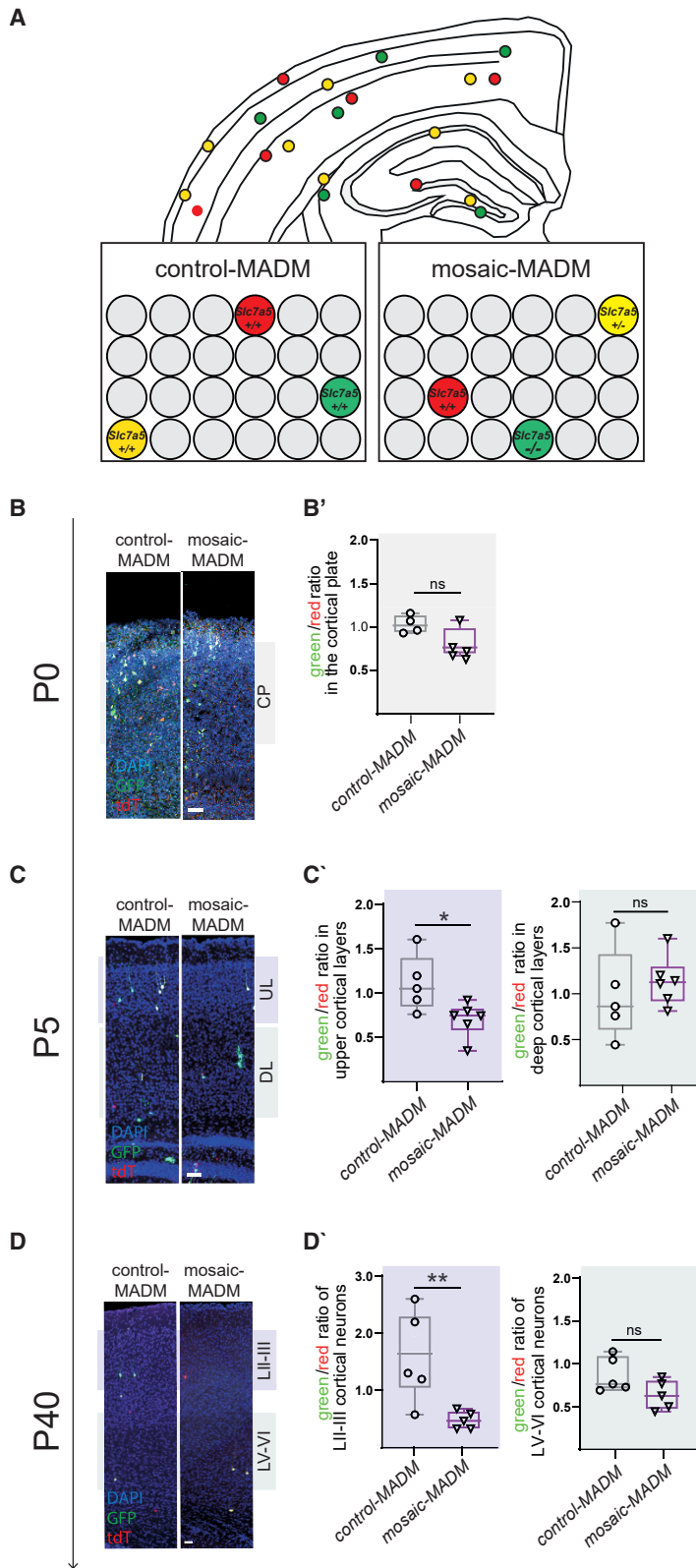
Figure 5. Loss of *Slc7a5* leads to a cell-autonomous reduction of cortical upper-layer neurons

(A) Schematic representation and genotypes of cells of control-MADM (*MADM-8^{GT/TG};Emx1-Cre+*) and mosaic-MADM (*MADM-8^{GT/TG,Slc7a5};Emx1-Cre+*) cortex.

(B) Coronal sections and (B') quantification of green/red cell ratio of MADM-labeled neurons in the cortical plate of P0 mosaic- and control-MADM littermates.

(C) Coronal sections and (C') quantification of green/red cell ratio of MADM-labeled upper layer (left) and lower layer (right) excitatory neurons in P5 mosaic- and control-MADM littermates.

(D) Coronal sections and (D') quantification of green/red cell ratio of MADM-labeled upper layer (left) and lower layer (right) excitatory neurons in P40 mosaic- and control-MADM littermates (P0: n = 4; P2 and P40: n = 5 [P2 and P40] animals per genotype; average of >5 slices per animal; $^{ns}p > 0.05$;$^{**}p < 0.001$; Mann-Whitney test; scale bars, 100 μm).
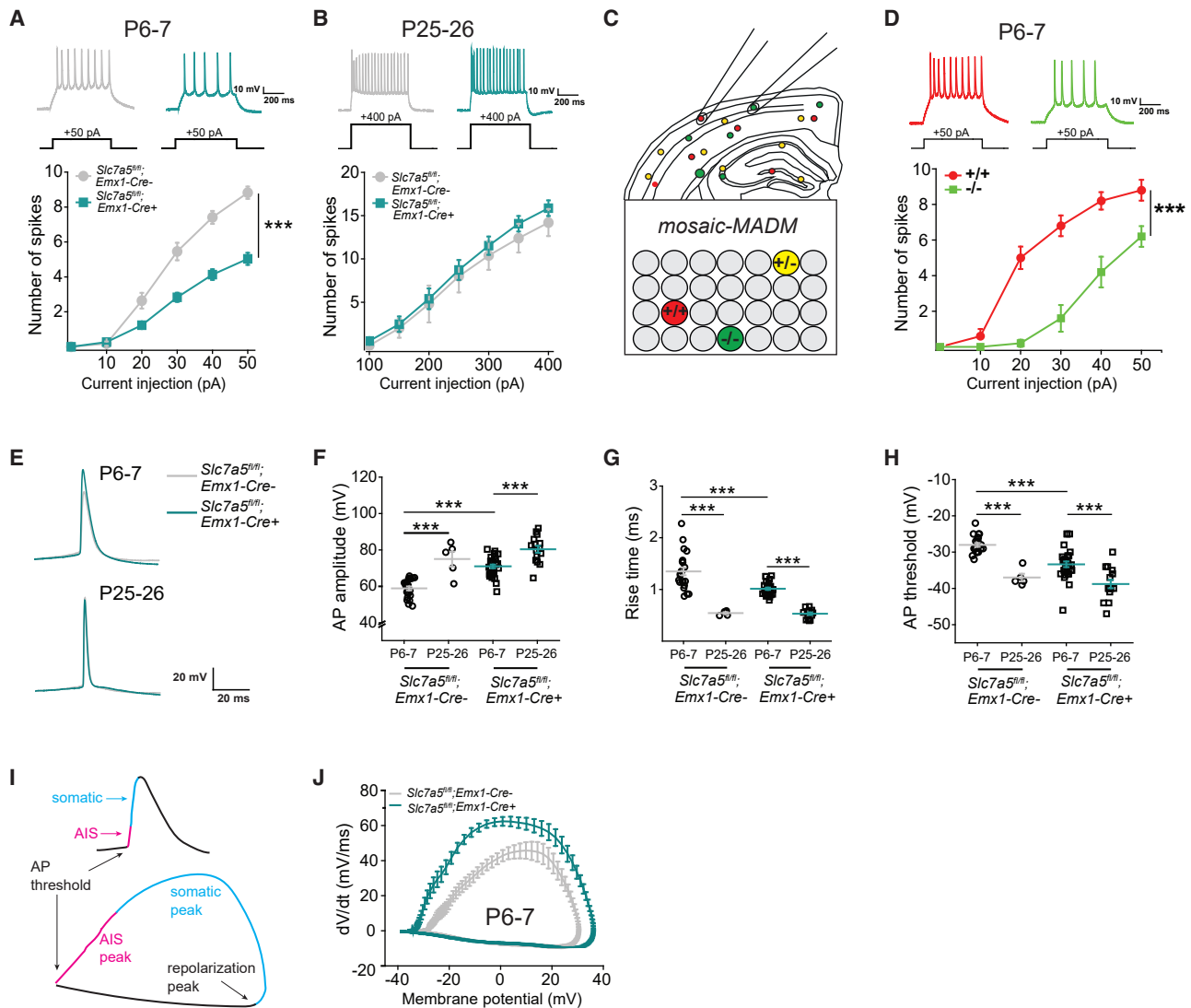
See also Figure S6.

Figure 6. Intracellular AA levels modulate neuronal excitability perinatally

(A and B) Current-clamp recordings from LII/LIII pyramidal neurons in (A) P6–P7 *Slc7a5$^{fl/fl}$;Emx1-Cre+* and *Slc7a5$^{fl/fl}$;Emx1-Cre−* SSCtx (*Slc7a5$^{fl/fl}$;Emx1Cre−*: n = 22 cells/3 mice; *Slc7a5$^{fl/fl}$;Emx1-Cre+*: n = 30 cells/3 mice; two-way ANOVA: genotype $F_{(1,311)}$ = 123.01 ***$p < 0.001$, current step $F_{(5,311)}$ = 205.3 ***$p < 0.001$, interaction $F_{(5,311)}$ = 16.75 ***$p < 0.001$) and (B) P25–P26 (*Slc7a5$^{fl/fl}$;Emx1Cre−*: n = 5 cells/3 mice; *Slc7a5$^{fl/fl}$;Emx1-Cre+*: n = 15 cells/3 mice; two-way ANOVA: genotype $F_{(1,139)}$ = 1.84 $^{ns}p > 0.5$, current step $F_{(6,139)}$ = 34.87 $^{ns}p > 0.5$, interaction $F_{(6,139)}$ = 0.07 $^{ns}p > 0.5$).

(C and D) Schematic (C) and results (D) of patch clamp recordings from green (*Slc7a5$^{−/−}$*) and red (*Slc7a5$^{+/+}$*) LII/LIII pyramidal neurons from the same P6–P7 mosaic-MADM animal (*Slc7a5$^{+/+}$*: n = 5 cells; *Slc7a5$^{−/−}$*: n = 7 cells from 5 mice; two-way ANOVA: genotype $F_{(1,65)}$ = 116.05 ***$p < 0.001$, current step $F_{(5,65)}$ = 79.22 ***$p < 0.001$, interaction $F_{(5,65)}$ = 11.16 ***$p < 0.001$).

(E) Representative action potential (AP) traces from the data shown in (A) and (B).

(F–H) The AP amplitude (F), AP rise time (G), and AP threshold (H) are transiently affected in Slc7a5 deficient LII/LIII pyramidal neurons at P6–P7 (numbers as in A) compared with age-matched littermates and P25–P26 time point (numbers as in B; two-way ANOVA for AP amplitude: genotype $F_{(1,71)}$ = 23.15 ***$p < 0.001$, time point $F_{(1,71)}$ = 52.57 ***$p < 0.001$, interaction $F_{(1,71)}$ = 3.24 $^{ns}p > 0.5$, Holm-Sidak post hoc ***$p < 0.001$). Two-way ANOVA for AP rise time: genotype $F_{(1,71)}$ = 7.32 ***$p < 0.001$, time point $F_{(1,71)}$ = 101.21 ***$p < 0.001$, interaction $F_{(1,71)}$ = 6.4 *$p < 0.05$, Holm-Sidak post hoc ***$p < 0.001$. Two-way ANOVA for AP threshold: genotype $F_{(1,71)}$ = 10.56 **$p < 0.01$, time point $F_{(1,71)}$ = 42.93 ***$p < 0.001$, interaction $F_{(1,71)}$ = 2.61 $^{ns}p > 0.5$, Holm-Sidak post hoc ***$p < 0.001$.

(I) AP plotted as voltage vs. time (top) and dV/dt vs. voltage (phase-plane plot, bottom). Phases of the AP are color-coded to highlight the initiation of the AP in the axon initial segment (AIS; pink), the propagation in the somatodendritic compartment (blue), and the repolarization peak.

(J) Phase-plane plot of data shown in (A) reveals defects in the AIS and the somatodendritic compartment in LII/LIII pyramidal neurons of *Slc7a5$^{fl/fl}$;Emx1-Cre+* animals.

See also Figure S7.

of the phenotype suggests a rather direct link between the metabolic state of the neuron and its excitability, it remained a possibility that the observed electrophysiological abnormalities were due to plasticity effects associated with network properties. However, should the reduced excitability directly be connected to, or even cause Slc7a5-dependent neuronal cell loss, we expected this phenotype to be cell autonomous. Thus, we returned to the mosaic-MADM mouse model (Figure 6C) and performed current-clamp recordings from $Slc7a5^{-/-}$ (green) and $Slc7a5^{+/+}$ (red) excitatory neurons in the same animal. Indeed, the AP firing rate is significantly reduced in LII and LIII $Slc7a5^{-/-}$ neurons from the SSCtx at P6–P7 (Figure 6D), indicating that $Slc7a5$ expression controls neuronal excitability cell-autonomously at early stages after birth. To understand the bases of the reduced firing rate caused by $Slc7a5$ deletion, we analyzed the AP properties. We inferred that $Slc7a5$ mutant neurons at P6–P7 do not fire less because they are more immature than wild-type neurons since they show AP features more comparable to those observed in older (i.e., P25–P26) control neurons (Figure 6E). Indeed, compared with controls, mutant neurons at P6–P7 display larger amplitude (Figure 6F), faster rise time (Figure 6G), and more hyperpolarized AP threshold (Figure 6H), matching the AP features observed in control neurons at P25–P26 and suggesting a different modulation of the voltage-gated channels involved in the initiation and rising phase of APs. In agreement, dendrites of mutant layer II and III pyramidal neurons present with a more mature spine morphology compared with controls (Figures S7E–S7I), therefore excluding a maturation delay. Nonetheless, other properties such as the resting membrane potential, the inter-spike interval (ISI) ratio, the AP decay time and half width are unchanged at P6–P7 (Figures S7J–S7M). We further examined the AP waveform using the phase-plane plot analysis (Figure 6I) to evaluate the dynamic changes of the membrane potential over time (dV/dt; Figure 6J). Our analysis revealed a striking increase in the velocity of the AP, highlighting a potential defect at the axon initial segment (AIS) and a faster AP backpropagation in the somatodendritic compartment of mutant neurons (Figures 6I and 6J), linking to the reduction of Kcnd2 protein level (Figure S7A). Accelerated AP backpropagation can also point toward defects in dendritic arborization.[57] Indeed, while the soma size is not affected (Figures S7N and S7O), we found a slight decrease in dendritic number and length in $Slc7a5^{fl/fl};Emx1-Cre+$ mice perinatally (Figures S7P and S7Q). However, these morphological alterations persist until adulthood (Figures S7R and S7S) and, therefore, are not associated with changes in excitability. Furthermore, while the unchanged resting membrane potential would exclude a role of ATP-dependent potassium channels, the electrophysiology data point to changes in the properties of multiple channels, probably through a different modulation and/or distribution of voltage-gated sodium (e.g., Nav1.2) and potassium channels (e.g., A-type), potentially explained by the downregulation of the detected palmitoylated proteins (Figure S7A).

Slc7a5 deficient animals show persistent behavioral defects

To assess whether the alterations observed in $Slc7a5$ mutant animals during the period of cortical circuit refinement lead to permanent behavioral abnormalities, we subjected adult $Slc7a5^{fl/fl};Emx1-Cre+$ and control animals to behavioral tests. In an open field, mutant animals present with increased horizontal (Figures 7A–7B′) and vertical explorative behavior (Figure 7C) but no anxiety-like behaviors (Figure 7D). Since SLC7A5 patients present with severe motor deficits, we assessed locomotion features in $Slc7a5^{fl/fl};Emx1-Cre+$ mice. Indeed, mutant mice exhibit moderate motor deficits (Figure 7E), such as decreased stride and stance length (Figures 7F–7F″), as well as hind limb clasping behavior (Figures 7G and 7G′). Next, we tested $Slc7a5^{fl/fl};Emx1-Cre+$ mice for social interest and social-memory behaviors. We found that $Slc7a5^{fl/fl};Emx1-Cre+$ mice have indications of sociability and social-memory impairments (Figures 7H–7K′). In summary, our analyses show that $Slc7a5$ deficiency in neurons causes persistent behavioral dysfunctions.

DISCUSSION

Neurons are generated in large amounts early during embryonic brain development, but a significant fraction of them are removed at subsequent developmental stages.[58–60] The removal of these cells must be highly selective and therefore regulated by tight mechanisms, possibly integrating both extrinsically and intrinsically driven processes. While a complete view of the factors directing this process is still missing, the literature suggests that neuronal activity might be used as a measure of neuronal integration in the circuitry and therefore is a determinant of the refinement of the perinatal network.[42,58] However, the potential upstream signaling and the pattern of neuronal activity determining this phenomenon remain unclear. Identifying extrinsic and intrinsic factors that can modulate neuronal properties at this developmental stage is critical since disrupting the refinement process can permanently affect brain circuits.

Here, we focused on the metabolic program of neural cells of the cerebral cortex as a measure of the intrinsic fit of a neuron and a determinant of its integration in the cortical circuit. Although metabolism is a crucial element of cellular fitness, there is no detailed description of how the levels of various metabolites change in the forebrain over time. By obtaining a metabolomic profile of the cortex at various developmental stages, we provide a comprehensive view of the metabolites detected in this brain region and their changes over the course of development. As several metabolites are linked to neurodevelopmental conditions, our data can be important to evaluate potential critical time windows in the context of brain disorders. For example, our analysis underscored a downward trajectory for essential LNAAs, with their levels decreasing significantly in the cerebral cortex at the perinatal period. By deleting $Slc7a5$, a LNAA transporter whose mutations cause autism and microcephaly, we tested the importance of regulating those AAs for the metabolic and physiological state of neural cells. We found that SLC7A5 expression is a decisive factor in specifying cortical neurons' metabolic state at perinatal stages. In this context, it is intriguing to observe that $Slc7a5$ transcription in neurons is induced by hypoxia,[61,62] a physiological state fetuses experience during and shortly after birth.[63] What happens if the typical levels of SLC7A5 substrates are not met during this developmental window? We report that decreased levels of BCAAs are coupled
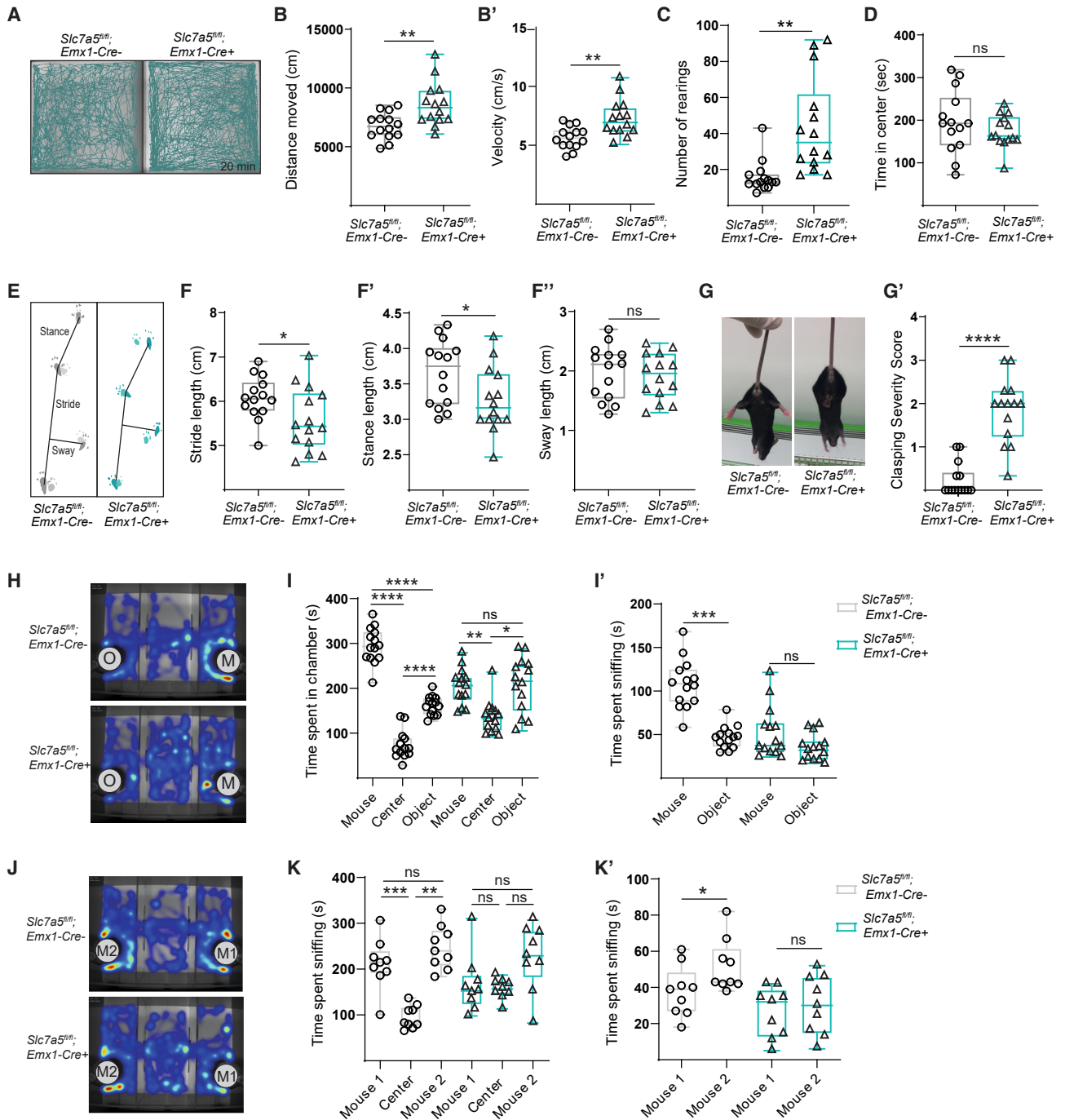
Figure 7. Loss of *Slc7a5* in cortical excitatory neurons causes persistent behavioral dysfunctions

(A–D) *Slc7a5^fl/fl^;Emx1-Cre+* animals are hyperactive. (A) Representative traces of mutant and wild-type animals moving 20 min in an open field. (B) Quantification of the total distance traveled, (B′) velocity, (C) number of rearings, and (D) time spent in center during one open field session (n = 14 mice per genotype; two-tailed unpaired t test).

(E–F″) *Slc7a5^fl/fl^;Emx1-Cre+* animals display a mild gait defect. (E) Representative control and mutant strides. Quantification of stride (F), stance (F′), and sway (F″) length (n = 14 per genotype, *p < 0.05; two-tailed unpaired t test).

(G) Hind limb clasping observed in *Slc7a5^fl/fl^;Emx1-Cre+* mice. (G′) Scoring of hind limb clasping severity (from 0–1 [normal] to 3 [most severe] (n = 14 animals per genotype; ****p < 0.00001; two-tailed unpaired t test).

(legend continued on next page)

with a disturbance of lipid metabolism. Previous studies have suggested a connection between BCAAs and lipids in some cell types[40,64–66] and pathological conditions.[67–69] While the exact trigger of the molecular reprogramming we observed in the absence of Slc7a5 remains to be investigated, our analysis demonstrates that in neural cells, the two pathways are tightly connected. Furthermore, our results indicate that neurons at perinatal stages use BCAAs as a main source of ATP production. This would explain the surge in *Slc7a5* expression at this stage and the dispensability of the mitochondrial pyruvate transporter in immature neurons.[70] Further, *Slc7a5* deletion leads to a cell-autonomous change in neuronal excitability, providing an elegant example of coupling the fitness of a cell with its integration in the neuronal network. Our mosaic analysis further suggests that intrinsic excitability can directly affect neuronal survival probability at this developmental stage. The exact mechanisms underlying the reduced neuronal excitability remain unclear. Our transcriptomic analysis did not uncover changes in ion channel expression in *Slc7a5*-deficient neurons. However, our proteomics data indicate changes in membrane-associated palmitoylated proteins in perinatal mutant mice. Thus, the most plausible explanation is that the shift in lipid profile observed in *Slc7a5* deficient cells leads to a different clustering and modulation of ion channels involved in neuronal excitability. In addition, a shift in the ratio of specific GPL subclasses can affect membrane properties such as its fluidity and curvature,[25] which can further modulate neuronal excitability.[45,47,71]

Altogether, our analysis highlights the importance of dietary-obtained factors, such as essential AAs, for neurodevelopment. The similar trajectory of the microcephaly onset observed in mice and humans with *SLC7A5* mutations suggests that although our metabolic profile describes changes in the murine brain, humans and mice may employ a similar metabolic program across time. Furthermore, the stage and cell-type specificity of the observed phenotypes point to the importance of performing longitudinal studies evaluating environmental, metabolically relevant factors that can influence specific stages of brain development and that may interact with genetic factors underlying human neurodevelopmental conditions.

Limitations of the study

There is a minimal number of tools available to assess metabolic pathways with the needed time and spatial resolution. Consequently, our study describes tissue-wide metabolic states but does not uncover cell-type-specific or short-lasting changes. Gene knockouts represent a powerful tool for studying facets of metabolism in specific cell populations *in vivo*, as done here for *Slc7a5*. Yet, given the interconnection between different arms of metabolism, establishing causality remains challenging. In the future, it would be interesting to dissect the exact contribution of different signaling pathways and subsets of metabolites to the phenotype observed in *Slc7a5* mutant mice. Efforts to obtain

metabolomic data under various conditions to implement exhaustive models of metabolism may also represent one way to address this challenge. Finally, although by comparing mice and individuals with *SLC7A5* mutations, we inferred similarities between species, the described metabolic states presumably also include mouse-specific changes. Studying mechanisms regulating human-specific brain metabolism is still challenging since most of the available tools involve *in vitro* systems. This poses some problems since excessive amounts of micro- and macronutrients in cell culture media can drive metabolism to different programs than *in vivo*. Hence, to better understand human brain metabolism, a combination of diverse model systems will be necessary.

STAR★METHODS

Detailed methods are provided in the online version of this paper and include the following:

- KEY RESOURCES TABLE
- RESOURCE AVAILABILITY
  - Lead contact
  - Materials availability
  - Data and code availability
- EXPERIMENTAL MODEL AND SUBJECT DETAILS
  - Animals
  - Human subjects
- METHOD DETAILS
  - Whole-exome sequencing analysis of patient samples
  - Immunofluorescence
  - Immunohistochemistry stainings
  - RNAscope Assay
  - Isolation and quantification of MADM-labelled tissue
  - Electron microscopy
  - Western Blot
  - Untargeted metabolomics of whole cortical tissue
  - Targeted intracellular metabolomics
  - Parallel untargeted lipidomics and metabolomics
  - Proteomic analysis
  - Bulk RNA-sequencing of cortical tissue
  - Analysis of the untargeted metabolomics dataset
  - Analysis of single-cell RNA sequencing data
  - Electrophysiology
  - Biocytin filling of neurons
  - Behavioral analysis
- QUANTIFICATION AND STATISTICAL ANALYSIS

SUPPLEMENTAL INFORMATION

Supplemental information can be found online at https://doi.org/10.1016/j.cell.2023.02.037.

(H–K′) *Slc7a5fl/fl;Emx1-Cre+* mice present defects in sociability. (H) Representative heatmaps of control (top) and mutant (bottom) behavior during the first round of the three-chamber sociability test (TCST). (I) Quantification of time spent in the chamber and (I′) time spent sniffing (n = 14 mice per genotype; ****p < 0.00001, **p < 0.01; *p < 0.05; nsp > 0.05; one-way ANOVA and Sidak's multiple comparison test). (J) Representative heat maps of control (top) and mutant (bottom) behavior during the second round of the TCST. (K) Quantification of time spent in the chamber and (K′) time spent sniffing (n = 9 mice per genotype; females only; ***p < 0.0001, **p < 0.01; *p < 0.05; nsp > 0.05; one-way ANOVA and Sidak's multiple comparison test).

AUTHOR CONTRIBUTIONS

L.S.K., B.B., L.A.S., S.G., C.K.-F., and M.T. performed experiments. D.M. analyzed the metabolomics, lipidomics, and proteomics datasets. G.N. conceived and supervised the study. M.G.B. and M.S. recruited and characterized patients. N.A., F.M.P., T.R., and S.H. generated the MADM lines and supported data analysis. N.M. and J.M. contributed to the interpretation of the results. G.N. wrote the paper together with L.S.K. All authors read and approved the final version of the manuscript.

DECLARATION OF INTERESTS

G.N. is a co-founder of Solgate.

INCLUSION AND DIVERSITY

We support inclusive, diverse, and equitable conduct of research. We worked to ensure sex balance in the selection of non-human subjects. Further, one or more of the authors of this paper self-identifies as an underrepresented ethnic minority in their field of research and within their geographical location.

REFERENCES

1. Parenti, I., Rabaneda, L.G., Schoen, H., and Novarino, G. (2020). Neurodevelopmental disorders: from genetics to functional pathways. Trends Neurosci. *43*, 608–621. https://doi.org/10.1016/j.tins.2020.05.004.

2. Galler, J.R., Bringas-Vega, M.L., Tang, Q., Rabinowitz, A.G., Musa, K.I., Chai, W.J., Omar, H., Abdul Rahman, M.R., Abd Hamid, A.I., Abdullah, J.M., et al. (2021). Neurodevelopmental effects of childhood malnutrition: A neuroimaging perspective. Neuroimage *231*, 117828. https://doi.org/10.1016/j.neuroimage.2021.117828.

3. Rock, K.D., and Patisaul, H.B. (2018). Environmental mechanisms of neurodevelopmental toxicity. Curr. Environ. Health Rep. *5*, 145–157. https://doi.org/10.1007/s40572-018-0185-0.

4. Ross, E.J., Graham, D.L., Money, K.M., and Stanwood, G.D. (2015). Developmental consequences of fetal exposure to drugs: what we know and what we still must learn. Neuropsychopharmacology *40*, 61–87. https://doi.org/10.1038/npp.2014.147.

5. Stankovic, I.N., and Colak, D. (2022). Prenatal drugs and their effects on the developing brain: insights from three-dimensional human organoids. Front. Neurosci. *16*, 848648.

6. Tărlungeanu, D.C., Deliu, E., Dotter, C.P., Kara, M., Janiesch, P.C., Scalise, M., Galluccio, M., Tesulov, M., Morelli, E., Sonmez, F.M., et al. (2016). Impaired amino acid transport at the blood brain barrier is a cause of autism spectrum disorder. Cell *167*, 1481–1494.e18. https://doi.org/10.1016/j.cell.2016.11.013.

7. Bond, A.M., Ming, G.-L., and Song, H. (2015). Adult mammalian neural stem cells and neurogenesis: five decades later. Cell Stem Cell *17*, 385–395. https://doi.org/10.1016/j.stem.2015.09.003.

8. Candelario, K.M., Shuttleworth, C.W., and Cunningham, L.A. (2013). Neural stem/progenitor cells display a low requirement for oxidative metabolism independent of hypoxia inducible factor-1alpha expression. J. Neurochem. *125*, 420–429. https://doi.org/10.1111/jnc.12204.

9. Duran, J., Gruart, A., López-Ramos, J.C., Delgado-García, J.M., and Guinovart, J.J. (2019). Glycogen in astrocytes and neurons: physiological and pathological aspects. Adv. Neurobiol. *23*, 311–329. https://doi.org/10.1007/978-3-030-27480-1_10.

10. Vilchez, D., Ros, S., Cifuentes, D., Pujadas, L., Vallès, J., García-Fojeda, B., Criado-García, O., Fernández-Sánchez, E., Medraño-Fernández, I., Domínguez, J., et al. (2007). Mechanism suppressing glycogen synthesis in neurons and its demise in progressive myoclonus epilepsy. Nat. Neurosci. *10*, 1407–1413. https://doi.org/10.1038/nn1998.

11. Mason, S. (2017). Lactate shuttles in neuroenergetics-homeostasis, allostasis and beyond. Front. Neurosci. *11*, 43. https://doi.org/10.3389/fnins.2017.00043.

12. Philips, T., and Rothstein, J.D. (2017). Oligodendroglia: metabolic supporters of neurons. J. Clin. Invest. *127*, 3271–3280. https://doi.org/10.1172/JCI90610.

13. Gorski, J.A., Talley, T., Qiu, M., Puelles, L., Rubenstein, J.L.R., and Jones, K.R. (2002). Cortical excitatory neurons and glia, but not GABAergic neurons, are produced in the Emx1-expressing lineage. J. Neurosci. *22*, 6309–6314.

14. Napolitano, L., Scalise, M., Galluccio, M., Pochini, L., Albanese, L.M., and Indiveri, C. (2015). LAT1 is the transport competent unit of the LAT1/CD98 heterodimeric amino acid transporter. Int. J. Biochem. Cell Biol. *67*, 25–33. https://doi.org/10.1016/j.biocel.2015.08.004.

15. Ye, Z., Wang, S., Zhang, C., and Zhao, Y. (2020). Coordinated modulation of energy metabolism and inflammation by branched-chain amino acids and fatty acids. Front. Endocrinol. *11*, 617.

16. Aon, M.A., Cortassa, S., and O'Rourke, B. (2010). Redox-optimized ROS balance: a unifying hypothesis. Biochim. Biophys. Acta *1797*, 865–877. https://doi.org/10.1016/j.bbabio.2010.02.016.

17. Murphy, M.P. (2009). How mitochondria produce reactive oxygen species. Biochem. J. *417*, 1–13. https://doi.org/10.1042/BJ20081386.

18. Robb, E.L., Hall, A.R., Prime, T.A., Eaton, S., Szibor, M., Viscomi, C., James, A.M., and Murphy, M.P. (2018). Control of mitochondrial superoxide production by reverse electron transport at complex I. J. Biol. Chem. *293*, 9869–9879. https://doi.org/10.1074/jbc.RA118.003647.

19. Iurlaro, R., and Muñoz-Pinedo, C. (2016). Cell death induced by endoplasmic reticulum stress. FEBS Journal *283*, 2640–2652. https://doi.org/10.1111/febs.13598.

20. Nwadike, C., Williamson, L.E., Gallagher, L.E., Guan, J.L., and Chan, E.Y.W. (2018). AMPK inhibits ULK1-dependent autophagosome formation and lysosomal acidification via distinct mechanisms. Mol. Cell. Biol. *38*. e00023–e00018. https://doi.org/10.1128/MCB.00023-18.

21. Riggs, A.C., Bernal-Mizrachi, E., Ohsugi, M., Wasson, J., Fatrai, S., Welling, C., Murray, J., Schmidt, R.E., Herrera, P.L., and Permutt, M.A. (2005). Mice conditionally lacking the Wolfram gene in pancreatic islet beta cells exhibit diabetes as a result of enhanced endoplasmic reticulum stress and apoptosis. Diabetologia *48*, 2313–2321. https://doi.org/10.1007/s00125-005-1947-4.

22. Takahara, T., Amemiya, Y., Sugiyama, R., Maki, M., and Shibata, H. (2020). Amino acid-dependent control of mTORC1 signaling: a variety of regulatory modes. J. Biomed. Sci. *27*, 87. https://doi.org/10.1186/s12929-020-00679-2.

23. Wortel, I.M.N., van der Meer, L.T., Kilberg, M.S., and van Leeuwen, F.N. (2017). Surviving stress: modulation of ATF4-mediated stress responses in normal and malignant cells. Trends Endocrinol. Metab. *28*, 794–806. https://doi.org/10.1016/j.tem.2017.07.003.

24. Zhang, S., Lin, X., Hou, Q., Hu, Z., Wang, Y., and Wang, Z. (2021). Regulation of mTORC1 by amino acids in mammalian cells: A general picture of recent advances. Anim. Nutr. *7*, 1009–1023. https://doi.org/10.1016/j.aninu.2021.05.003.

25. Holthuis, J.C.M., and Menon, A.K. (2014). Lipid landscapes and pipelines in membrane homeostasis. Nature *510*, 48–57. https://doi.org/10.1038/nature13474.

26. Felber, J.P., and Golay, A. (1995). Regulation of nutrient metabolism and energy expenditure. Metabolism *44*, 4–9. https://doi.org/10.1016/0026-0495(95)90201-5.

27. Foufelle, F., and Ferré, P. (2013). Mechanism of storage and synthesis of fatty acids and triglycerides in White adipocytes. In Physiology and Physiopathology of Adipose Tissue, J.-P. Bastard and B. Fève, eds. (Springer), pp. 101–121. https://doi.org/10.1007/978-2-8178-0343-2_8.

28. Alves-Bezerra, M., and Cohen, D.E. (2017). Triglyceride metabolism in the liver. Compr. Physiol. *8*, 1–8. https://doi.org/10.1002/cphy.c170012.

29. Bruce, K.D., Zsombok, A., and Eckel, R.H. (2017). Lipid processing in the brain: A key regulator of systemic metabolism. Front. Endocrinol. *8*, 60.

30. Xu, X., Hu, J., McGrath, B.C., and Cavener, D.R. (2013). GCN2 in the brain programs PPARγ2 and triglyceride storage in the liver during perinatal development in response to maternal dietary fat. PLoS One *8*, e75917. https://doi.org/10.1371/journal.pone.0075917.

31. Bhaduri, A., Neumann, E.K., Kriegstein, A.R., and Sweedler, J.V. (2021). Identification of lipid heterogeneity and diversity in the developing human brain. JACS Au *1*, 2261–2270. https://doi.org/10.1021/jacsau.1c00393.

32. Farooqui, A.A., Horrocks, L.A., and Farooqui, T. (2000). Glycerophospholipids in brain: their metabolism, incorporation into membranes, functions, and involvement in neurological disorders. Chem. Phys. Lipids *106*, 1–29. https://doi.org/10.1016/S0009-3084(00)00128-6.

33. Feral, C.C., Nishiya, N., Fenczik, C.A., Stuhlmann, H., Slepak, M., and Ginsberg, M.H. (2005). CD98hc (SLC3A2) mediates integrin signaling. Proc. Natl. Acad. Sci. USA *102*, 355–360. https://doi.org/10.1073/pnas.0404852102.

34. Yan, R., Zhao, X., Lei, J., and Zhou, Q. (2019). Structure of the human LAT1–4F2hc heteromeric amino acid transporter complex. Nature *568*, 127–130. https://doi.org/10.1038/s41586-019-1011-z.

35. Castilho, B.A., Shanmugam, R., Silva, R.C., Ramesh, R., Himme, B.M., and Sattlegger, E. (2014). Keeping the eIF2 alpha kinase Gcn2 in check. Biochim. Biophys. Acta *1843*, 1948–1968. https://doi.org/10.1016/j.bbamcr.2014.04.006.

36. Gold, L.T., and Masson, G.R. (2022). GCN2: roles in tumour development and progression. Biochem. Soc. Trans. *50*, 737–745. https://doi.org/10.1042/BST20211252.

37. Wei, C., Lin, M., Jinjun, B., Su, F., Dan, C., Yan, C., Jie, Y., Jin, Z., Zi-Chun, H., and Wu, Y. (2015). Involvement of general control nonderepressible kinase 2 in cancer cell apoptosis by posttranslational mechanisms. Mol. Biol. Cell *26*, 1044–1057. https://doi.org/10.1091/mbc.E14-10-1438.

38. She, P., Bunpo, P., Cundiff, J.K., Wek, R.C., Harris, R.A., and Anthony, T.G. (2013). General control nonderepressible 2 (GCN2) kinase protects oligodendrocytes and white matter during branched-chain amino acid deficiency in mice. J. Biol. Chem. *288*, 31250–31260. https://doi.org/10.1074/jbc.M113.498469.

39. Young, S.G. (1990). Recent progress in understanding apolipoprotein B. Circulation *82*, 1574–1594. https://doi.org/10.1161/01.CIR.82.5.1574.

40. White, P.J., McGarrah, R.W., Grimsrud, P.A., Tso, S.-C., Yang, W.-H., Haldeman, J.M., Grenier-Larouche, T., An, J., Lapworth, A.L., Astapova, I., et al. (2018). The BCKDH kinase and phosphatase integrate BCAA and lipid metabolism via regulation of ATP-citrate lyase. Cell Metab. *27*, 1281–1293.e7. https://doi.org/10.1016/j.cmet.2018.04.015.

41. Blanquie, O., Yang, J.-W., Kilb, W., Sharopov, S., Sinning, A., and Luhmann, H.J. (2017). Electrical activity controls area-specific expression of neuronal apoptosis in the mouse developing cerebral cortex. eLife *6*, e27696. https://doi.org/10.7554/eLife.27696.

42. Wong, F.K., Bercsenyi, K., Sreenivasan, V., Portalés, A., Fernández-Otero, M., and Marín, O. (2018). Pyramidal cell regulation of interneuron survival sculpts cortical networks. Nature *557*, 668–673. https://doi.org/10.1038/s41586-018-0139-6.

43. Contreras, X., Amberg, N., Davaatseren, A., Hansen, A.H., Sonntag, J., Andersen, L., Bernthaler, T., Streicher, C., Heger, A., Johnson, R.L., et al. (2021). A genome-wide library of MADM mice for single-cell genetic mosaic analysis. Cell Rep. *35*, 109274. https://doi.org/10.1016/j.celrep.2021.109274.

44. Zong, H., Espinosa, J.S., Su, H.H., Muzumdar, M.D., and Luo, L. (2005). Mosaic analysis with double markers in mice. Cell *121*, 479–492. https://doi.org/10.1016/j.cell.2005.02.012.

45. Zheng, H., Liu, W., Anderson, L.Y., and Jiang, Q.-X. (2011). Lipid-dependent gating of a voltage-gated potassium channel. Nat. Commun. *2*, 250. https://doi.org/10.1038/ncomms1254.

46. Duncan, A.L., Song, W., and Sansom, M.S.P. (2020). Lipid-dependent regulation of ion channels and G protein–coupled receptors: insights from structures and simulations. Annu. Rev. Pharmacol. Toxicol. *60*, 31–50. https://doi.org/10.1146/annurev-pharmtox-010919-023411.

47. Tillman, T.S., and Cascio, M. (2003). Effects of membrane lipids on ion channel structure and function. Cell Biochem. Biophys. *38*, 161–190. https://doi.org/10.1385/CBB:38:2:161.

48. Curran, J., and Mohler, P.J. (2015). Alternative paradigms for ion channelopathies: disorders of ion channel membrane trafficking and posttranslational modification. Annu. Rev. Physiol. *77*, 505–524. https://doi.org/10.1146/annurev-physiol-021014-071838.

49. Resh, M.D. (2013). Covalent lipid modifications of proteins. Curr. Biol. *23*, R431–R435. https://doi.org/10.1016/j.cub.2013.04.024.

50. Chen, B., Sun, Y., Niu, J., Jarugumilli, G.K., and Wu, X. (2018). Protein lipidation in cell signaling and diseases: function, regulation and therapeutic opportunities. Cell Chem. Biol. *25*, 817–831. https://doi.org/10.1016/j.chembiol.2018.05.003.

51. Globa, A.K., and Bamji, S.X. (2017). Protein palmitoylation in the development and plasticity of neuronal connections. Curr. Opin. Neurobiol. *45*, 210–220. https://doi.org/10.1016/j.conb.2017.02.016.

52. Fujiwara, Y., Kondo, H.X., Shirota, M., Kobayashi, M., Takeshita, K., Nakagawa, A., Okamura, Y., and Kinoshita, K. (2016). Structural basis for the membrane association of ankyrinG via palmitoylation. Sci. Rep. *6*, 23981. https://doi.org/10.1038/srep23981.

53. Kim, J., Wei, D.-S., and Hoffman, D.A. (2005). Kv4 potassium channel subunits control action potential repolarization and frequency-dependent broadening in rat hippocampal CA1 pyramidal neurones. J. Physiol. *569*, 41–57. https://doi.org/10.1113/jphysiol.2005.095042.

54. Cassinelli, S., Viñola-Renart, C., Benavente-Garcia, A., Navarro-Pérez, M., Capera, J., and Felipe, A. (2022). Palmitoylation of voltage-gated ion channels. Int. J. Mol. Sci. *23*, 9357. https://doi.org/10.3390/ijms23169357.

55. Tomasoni, R., Repetto, D., Morini, R., Elia, C., Gardoni, F., Di Luca, M., Turco, E., Defilippi, P., and Matteoli, M. (2013). SNAP-25 regulates spine formation through postsynaptic binding to p140Cap. Nat. Commun. *4*, 2136. https://doi.org/10.1038/ncomms3136.

56. MacDonald, P.E., Wang, G., Tsuk, S., Dodo, C., Kang, Y., Tang, L., Wheeler, M.B., Cattral, M.S., Lakey, J.R.T., Salapatek, A.M.F., et al. (2002). Synaptosome-associated protein of 25 kilodaltons modulates Kv2.1 voltage-dependent K(+) channels in neuroendocrine islet beta-cells through an interaction with the channel N terminus. Mol. Endocrinol. *16*, 2452–2461. https://doi.org/10.1210/me.2002-0058.

57. Vetter, P., Roth, A., and Häusser, M. (2001). Propagation of action potentials in dendrites depends on dendritic morphology. J. Neurophysiol. *85*, 926–937. https://doi.org/10.1152/jn.2001.85.2.926.

58. Dekkers, M.P.J., Nikoletopoulou, V., and Barde, Y.-A. (2013). Cell biology in neuroscience: death of developing neurons: new insights and implications for connectivity. J. Cell Biol. *203*, 385–393. https://doi.org/10.1083/jcb.201306136.

59. Southwell, D.G., Paredes, M.F., Galvao, R.P., Jones, D.L., Froemke, R.C., Sebe, J.Y., Alfaro-Cervello, C., Tang, Y., Garcia-Verdugo, J.M., Rubenstein, J.L., et al. (2012). Intrinsically determined cell death of developing cortical interneurons. Nature *491*, 109–113. https://doi.org/10.1038/nature11523.

60. Nikolić, M., Gardner, H.A., and Tucker, K.L. (2013). Postnatal neuronal apoptosis in the cerebral cortex: physiological and pathophysiological mechanisms. Neuroscience *254*, 369–378. https://doi.org/10.1016/j.neuroscience.2013.09.035.

61. Fitzgerald, E., Roberts, J., Tennant, D.A., Boardman, J.P., and Drake, A.J. (2021). Metabolic adaptations to hypoxia in the neonatal mouse forebrain can occur independently of the transporters SLC7A5 and SLC3A2. Sci. Rep. *11*, 9092. https://doi.org/10.1038/s41598-021-88757-9.

62. Onishi, Y., Hiraiwa, M., Kamada, H., Iezaki, T., Yamada, T., Kaneda, K., and Hinoi, E. (2019). Hypoxia affects Slc7a5 expression through HIF-2α in differentiated neuronal cells. FEBS Open Bio *9*, 241–247. https://doi.org/10.1002/2211-5463.12559.

63. Huch, A., Huch, R., Schneider, H., and Rooth, G. (1977). Continuous transcutaneous monitoring of fetal oxygen tension during labour. Br. J. Obstet. Gynaecol. *84*, 1–39. https://doi.org/10.1111/j.1471-0528.1977.tb16231.x.

64. Bishop, C.A., Schulze, M.B., Klaus, S., and Weitkunat, K. (2020). The branched-chain amino acids valine and leucine have differential effects on hepatic lipid metabolism. FASEB J. *34*, 9727–9739. https://doi.org/10.1096/fj.202000195R.

65. Wallace, M., Green, C.R., Roberts, L.S., Lee, Y.M., McCarville, J.L., Sanchez-Gurmaches, J., Meurs, N., Gengatharan, J.M., Hover, J.D., Phillips, S.A., et al. (2018). Enzyme promiscuity drives branched-chain fatty acid synthesis in adipose tissues. Nat. Chem. Biol. *14*, 1021–1031. https://doi.org/10.1038/s41589-018-0132-2.

66. Crown, S.B., Marze, N., and Antoniewicz, M.R. (2015). Catabolism of branched chain amino acids contributes significantly to synthesis of odd-chain and even-chain fatty acids in 3T3-L1 adipocytes. PLoS One *10*, e0145850. https://doi.org/10.1371/journal.pone.0145850.

67. Rossmeislová, L., Gojda, J., and Smolková, K. (2021). Pancreatic cancer: branched-chain amino acids as putative key metabolic regulators? Cancer Metastasis Rev. *40*, 1115–1139. https://doi.org/10.1007/s10555-021-10016-0.

68. Newgard, C.B. (2012). Interplay between lipids and branched-chain amino acids in development of insulin resistance. Cell Metab. *15*, 606–614. https://doi.org/10.1016/j.cmet.2012.01.024.

69. Lerin, C., Goldfine, A.B., Boes, T., Liu, M., Kasif, S., Dreyfuss, J.M., De Sousa-Coelho, A.L., Daher, G., Manoli, I., Sysol, J.R., et al. (2016). Defects in muscle branched-chain amino acid oxidation contribute to impaired lipid metabolism. Mol. Metab. *5*, 926–936. https://doi.org/10.1016/j.molmet.2016.08.001.

70. Petrelli, F., Scandella, V., Montessuit, S., Zamboni, N., Martinou, J.-C., and Knobloch, M. (2022). Mitochondrial pyruvate metabolism regulates the activation of quiescent adult neural stem cells https://doi.org/10.1101/2022.05.31.494137.

71. Schmidt, D., Jiang, Q.-X., and MacKinnon, R. (2006). Phospholipids and the origin of cationic gating charges in voltage sensors. Nature *444*, 775–779. https://doi.org/10.1038/nature05416.

72. Di Bella, D.J., Habibi, E., Stickels, R.R., Scalia, G., Brown, J., Yadollahpour, P., Yang, S.M., Abbate, C., Biancalani, T., Macosko, E.Z., et al. (2021). Molecular logic of cellular diversification in the mouse cerebral cortex. Nature *595*, 554–559. https://doi.org/10.1038/s41586-021-03670-5.

73. Yuan, W., Ma, S., Brown, J.R., Kim, K., Murek, V., Trastulla, L., Meissner, A., Lodato, S., Shetty, A.S., Levin, J.Z., et al. (2022). Temporally divergent regulatory mechanisms govern neuronal diversification and maturation in the mouse and marmoset neocortex. Nat. Neurosci. *25*, 1049–1058. https://doi.org/10.1038/s41593-022-01123-4.

74. Sinclair, L.V., Rolf, J., Emslie, E., Shi, Y.-B., Taylor, P.M., and Cantrell, D.A. (2013). Control of amino-acid transport by antigen receptors coordinates the metabolic reprogramming essential for T cell differentiation. Nat. Immunol. *14*, 500–508. https://doi.org/10.1038/ni.2556.

75. Schneider, C.A., Rasband, W.S., and Eliceiri, K.W. (2012). NIH Image to ImageJ: 25 years of image analysis. Nat. Methods *9*, 671–675. https://doi.org/10.1038/nmeth.2089.

76. Tsugawa, H., Cajka, T., Kind, T., Ma, Y., Higgins, B., Ikeda, K., Kanazawa, M., VanderGheynst, J., Fiehn, O., and Arita, M. (2015). MS-DIAL: data-independent MS/MS deconvolution for comprehensive metabolome analysis. Nat. Methods *12*, 523–526. https://doi.org/10.1038/nmeth.3393.

77. Tyanova, S., Temu, T., and Cox, J. (2016). The MaxQuant computational platform for mass spectrometry-based shotgun proteomics. Nat. Protoc. *11*, 2301–2319. https://doi.org/10.1038/nprot.2016.136.

78. Ritchie, M.E., Phipson, B., Wu, D., Hu, Y., Law, C.W., Shi, W., and Smyth, G.K. (2015). limma powers differential expression analyses for RNA-sequencing and microarray studies. Nucleic Acids Res. *43*, e47. https://doi.org/10.1093/nar/gkv007.

79. Hao, Y., Hao, S., Andersen-Nissen, E., Mauck, W.M., Zheng, S., Butler, A., Lee, M.J., Wilk, A.J., Darby, C., Zager, M., et al. (2021). Integrated analysis of multimodal single-cell data. Cell *184*, 3573–3587.e29. https://doi.org/10.1016/j.cell.2021.04.048.

80. Wearne, S.L., Rodriguez, A., Ehlenberger, D.B., Rocher, A.B., Henderson, S.C., and Hof, P.R. (2005). New techniques for imaging, digitization and analysis of three-dimensional neural morphology on multiple scales. Neuroscience *136*, 661–680. https://doi.org/10.1016/j.neuroscience.2005.05.053.

81. Afgan, E., Baker, D., Batut, B., van den Beek, M., Bouvier, D., Čech, M., Chilton, J., Clements, D., Coraor, N., Grüning, B.A., et al. (2018). The Galaxy platform for accessible, reproducible and collaborative biomedical analyses: 2018 update. Nucleic Acids Res. *46*, W537–W544. https://doi.org/10.1093/nar/gky379.

82. Dobin, A., Davis, C.A., Schlesinger, F., Drenkow, J., Zaleski, C., Jha, S., Batut, P., Chaisson, M., and Gingeras, T.R. (2013). STAR: ultrafast universal RNA-seq aligner. Bioinformatics *29*, 15–21. https://doi.org/10.1093/bioinformatics/bts635.

83. Love, M.I., Huber, W., and Anders, S. (2014). Moderated estimation of fold change and dispersion for RNA-seq data with DESeq2. Genome Biol. *15*, 550. https://doi.org/10.1186/s13059-014-0550-8.

84. Falcon, S., and Gentleman, R. (2007). Using GOstats to test gene lists for GO term association. Bioinformatics *23*, 257–258. https://doi.org/10.1093/bioinformatics/btl567.

85. Pedregosa, F., Varoquaux, G., Gramfort, A., Michel, V., Thirion, B., Grisel, O., Blondel, M., Prettenhofer, P., Weiss, R., Dubourg, V., et al. (2011). Scikit-learn: machine learning in python. J. Mach. Learn. Res. *12*, 2825–2830.

86. McKinney, W. (2010). Data structures for statistical computing in python. Proceedings of the Python in Science Conference, 56–61. https://doi.org/10.25080/Majora-92bf1922-00a.

87. Harris, C.R., Millman, K.J., van der Walt, S.J., Gommers, R., Virtanen, P., Cournapeau, D., Wieser, E., Taylor, J., Berg, S., Smith, N.J., et al. (2020). Array programming with NumPy. Nature *585*, 357–362. https://doi.org/10.1038/s41586-020-2649-2.

88. Seabold, S., and Perktold, J. (2010). Statsmodels: econometric and statistical modeling with python. Proceedings of the Python in Science Conference, 92–96. https://doi.org/10.25080/Majora-92bf1922-011.

89. Virtanen, P., Gommers, R., Oliphant, T.E., Haberland, M., Reddy, T., Cournapeau, D., Burovski, E., Peterson, P., Weckesser, W., Bright, J., et al. (2020). SciPy 1.0: fundamental algorithms for scientific computing in Python. Nat. Methods *17*, 261–272. https://doi.org/10.1038/s41592-019-0686-2.

90. Waskom, M.L. (2021). seaborn: statistical data visualization. J. Open Source Software *6*, 3021. https://doi.org/10.21105/joss.03021.

91. Hunter, J.D. (2007). Matplotlib: A 2D graphics environment. Comput. Sci. Eng. *9*, 90–95. https://doi.org/10.1109/MCSE.2007.55.

92. Kisanuki, Y.Y., Hammer, R.E., Miyazaki, J., Williams, S.C., Richardson, J.A., and Yanagisawa, M. (2001). Tie2-Cre transgenic mice: a new model for endothelial cell-lineage analysis in vivo. Dev. Biol. *230*, 230–242. https://doi.org/10.1006/dbio.2000.0106.

93. Richards, S., Aziz, N., Bale, S., Bick, D., Das, S., Gastier-Foster, J., Grody, W.W., Hegde, M., Lyon, E., Spector, E., et al. (2015). Standards and guidelines for the interpretation of sequence variants: a joint consensus recommendation of the American College of Medical Genetics and Genomics and the Association for Molecular Pathology. Genet. Med. *17*, 405–424. https://doi.org/10.1038/gim.2015.30.

94. Wang, F., Flanagan, J., Su, N., Wang, L.-C., Bui, S., Nielson, A., Wu, X., Vo, H.-T., Ma, X.-J., and Luo, Y. (2012). RNAscope: a novel in situ RNA analysis platform for formalin-fixed, paraffin-embedded tissues. J. Mol. Diagn. *14*, 22–29. https://doi.org/10.1016/j.jmoldx.2011.08.002.

95. Dieterle, F., Ross, A., Schlotterbeck, G., and Senn, H. (2006). Probabilistic quotient normalization as robust method to account for dilution of complex biological mixtures. Application in 1H NMR metabonomics. Anal. Chem. *78*, 4281–4290. https://doi.org/10.1021/ac051632c.

96. Drotleff, B., and Lämmerhofer, M. (2019). Guidelines for selection of internal standard-based normalization strategies in untargeted lipidomic profiling by LC-HR-MS/MS. Anal. Chem. *91*, 9836–9843. https://doi.org/10.1021/acs.analchem.9b01505.

97. Lee, S.H., Valtschanoff, J.G., Kharazia, V.N., Weinberg, R., and Sheng, M. (2001). Biochemical and morphological characterization of an intracellular membrane compartment containing AMPA receptors. Neuropharmacology *41*, 680–692. https://doi.org/10.1016/s0028-3908(01)00124-1.

98. Moy, S.S., Nadler, J.J., Young, N.B., Perez, A., Holloway, L.P., Barbaro, R.P., Barbaro, J.R., Wilson, L.M., Threadgill, D.W., Lauder, J.M., et al. (2007). Mouse behavioral tasks relevant to autism: phenotypes of 10 inbred strains. Behav. Brain Res. *176*, 4–20. https://doi.org/10.1016/j.bbr.2006.07.030.

99. Carter, R.J., Morton, J., and Dunnett, S.B. (2001). Motor coordination and balance in rodents. Curr. Protoc. Neurosci. *Chapter*, Unit 8.12. https://doi.org/10.1002/0471142301.ns0812s15.

100. Guyenet, S.J., Furrer, S.A., Damian, V.M., Baughan, T.D., La Spada, A.R., and Garden, G.A. (2010). A simple composite phenotype scoring system for evaluating mouse models of cerebellar ataxia. J. Vis. Exp. *39*, 1787.

STAR★METHODS

KEY RESOURCES TABLE

REAGENT or RESOURCE	SOURCE	IDENTIFIER
Antibodies		
Rat monoclonal Anti-Ctip2	Abcam	Cat#ab18465; RRID:AB_2064130
Rabbit polyclonal Anti-Cux1	Santa Cruz	Cat#sc-13024; RRID:AB_2261231
Rabbit polyclonal Anti-Iba1	FUJIFILM Wako	Cat#019 19741; RRID:AB_839504
Rabbit monoclonal Anti-Gfap	Cell Signaling Technologies	Cat#12389; RRID:AB_2631098
Mouse monoclonal Anti-Parvalbumin	Chemicon	Cat#MAB1572;RRID:AB_2174013
Rabbit polyclonal Anti-Cleaved-Caspase-3	Cell Signaling Technologies	Cat#9661; RRID:AB_2341188
Rabbit polyclonal Anti Human LAT1 (SLC7A5)	Transgenic Inc.	Cat#KE026; RRID:AB_1627093
Rabbit polyclonal Anti-Gapdh	Millipore Merck	Cat#ABS16; RRID:AB_10806772
Rabbit monoclonal Anti-S6 ribosomal protein	Cell Signaling Technologies	Cat#2217; RRID:AB_331355
Rabbit monoclonal Anti-phosphoS6 ribosomal protein[240-244]	Cell Signaling Technologies	Cat#5364; RRID:AB_10694233
Rabbit polyclonal Anti-phosphoS6 ribosomal protein[235-236]	Cell Signaling Technologies	Cat#2211; RRID:AB_331679
Rabbit monoclonal Anti-4eibp1	Cell Signaling Technologies	Cat#9644; RRID:AB_2097841
Rabbit monoclonal Anti-phospho4ebp1	Cell Signaling Technologies	Cat#2855; RRID:AB_560835
Rabbit polyclonal Anti-Atf4	Proteintech	Cat#10835; RRID:AB_2058600
Rabbit polyclonal Anti-Lamp1	Abcam	Cat#ab24170; RRID:AB_775978
Rabbit polyclonal Anti-Lc3-I/II	Millipore Merck	Cat#ABC929; RRID: N/A
Rabbit polyclonal Anti-Eif2a	Cell Signaling Technologies	Cat#9722; RRID:AB_2230924
Rabbit polyclonal Anti-phosphoEif2a	Cell Signaling Technologies	Cat#9721; RRID:AB_330951
Rabbit polyclonal Anti-AMPK	Cell Signaling Technologies	Cat#2532; RRID:AB_330331
Rabbit monoclonal Anti-phosphoAMPK	Cell Signaling Technologies	Cat#2535; RRID:AB_331250
Rabbit normal IgG control	Cell Signaling Technologies	Cat#2729; RRID:AB_1031062
Rabbit IgG HRP Linked Whole Ab	Cytiva	Cat#NA934; RRID:AB_772206
Donkey anti-Rabbit IgG (H+L) Highly Cross-Adsorbed Secondary Antibody, Alexa Fluor™ 488	Invitrogen™	Cat#A-21206; RRID:AB_2535792
Goat anti-Rabbit IgG (H+L) Highly Cross-Adsorbed Secondary Antibody, Alexa Fluor™ 594	Invitrogen™	Cat#A-11037; RRID:AB_2534095
Donkey anti-Rat IgG (H+L) Highly Cross-Adsorbed Secondary Antibody, Alexa Fluor™ 594	Invitrogen™	Cat#A-21209; RRID:AB_2535795
Goat anti-Mouse IgG (H+L) Highly Cross-Adsorbed Secondary Antibody, Alexa Fluor™ Plus 488	Invitrogen™	Cat#A-32723; RRID:AB_2633275
Streptavidin, Alexa Fluor™ 488 Conjugate	Invitrogen™	Cat#S32354; RRID:AB_2315383
Chemicals, peptides, and recombinant proteins		
DAPI (4',6-Diamidino-2-Phenylindole, Dihydrochloride)	Invitrogen™	D1306
Cresyl Violet acetate	Sigma Aldrich	C5042
ROTI®Histol	Carl Roth	6640.1
Osmium tetroxide EM	Science Services	E19110
Uranyl acetate EM	AL-Labortechnik	77870.02
Propylene oxide EM	Sigma Aldrich	82320

(Continued on next page)

Continued

REAGENT or RESOURCE	SOURCE	IDENTIFIER
Durucupan Component A	Sigma Aldrich	44611
Durucupan Component B	Sigma Aldrich	44611
Durucupan Component C	Sigma Aldrich	44611
Durucupan Component D	Sigma Aldrich	44611
IGEPAL® CA-630 (NP-40)	Sigma Aldrich	I3021
PPi (Sodium pyrophosphate dibasic)	Sigma Aldrich	71501
Sodium orthovanadate (Na3VO4)	Sigma Aldrich	S6508
Bromophenol Blue	Sigma Aldrich	B0126
Pierce™ DTT	Thermo Scientific™	20290
Methanol (hypergrade for LC-MS LiChrosolv®)	Supelco	1.06035
Acetonitrile (hypergrade for LC-MS LiChrosolv®)	Supelco	1.00029
Water (hypergrade for LC-MS LiChrosolv®)	Supelco	1.15333
Isopropanol (hypergrade for LC-MS)	EMD Millipore	1.02781
Formic acid (LC-MS LiChropur®)	Supelco	533002
Acetic acid (HPLC LiChropur®)	Supelco	543808
Ammonium hydroxide (25 %, w:v)	Supelco	105432
EquiSPLASH™ LIPIDOMIX® Quantitative Mass Spec Internal Standard	Avanti Polar Lipids	330731-1EA
Metabolomics amino acid mix standard	Cambridge Isotope Laboratories	MSK-A2-1.2
EBSS, no calcium, no magnesium, no phenol red	Gibco™	14155063
Bovine Serum Albumin	Sigma Aldrich	A9647
TRIzol™ Reagent	Invitrogen™	15596026
cOmplete™, Mini, EDTA-free Protease Inhibitor Cocktail	Roche	4693159001
Sodium chloride	VWR (Merck)	1.06404.1000
Sodium bicarbonate	VWR (Merck)	1.06329.1000
Potassium chloride	VWR (Merck)	26764.232
D-glucose	VWR (Merck)	1.08342.1000
Sucrose	Sigma Aldrich	16104
Magnesium chloride	Honeywell	M9272-1KG
Calcium chloride	VWR (Merck)	1.02382.0250
N-Methyl-D-glucamine	Sigma Aldrich	M2004-500G
HEPES	Sigma Aldrich	M3375-100G
di-Sodium hydrogen phosphate dihydrate	VWR (Merck)	1.06580.0500
(+)-Sodium L-ascorbate	Sigma Aldrich	11140-250G
Thiourea	Sigma Aldrich	T8656-50G
Sodium pyruvate	Sigma Aldrich	P2256-25G
Adenosine 5'-triphosphate magnesium salt	Sigma Aldrich	A9187-1G
Guanosine 5'-triphosphate sodium salt hydrate	Sigma Aldrich	G8877-100MG
EGTA	Sigma Aldrich	EO396-100G
Potassium D-gluconate	Sigma Aldrich	G4500-100G
Phosphocreatine disodium salt hydrate	Sigma Aldrich	P7936-5G
Critical commercial assays		
TruSeq Exome Library Kit	Illumina	20020614
Pierce™ ECL Western Blotting Substrate	Thermo Scientific™	32106
SuperSignal™ West Pico PLUS Chemiluminescent Substrate	Thermo Scientific™	34577

(Continued on next page)

Continued

REAGENT or RESOURCE	SOURCE	IDENTIFIER
Papain Dissociation Kit	Worthington Biochemical Corp.	LK003150
Pierce™ BCA Protein Assay Kit	Thermo Scientific™	23227
QuantSeq FWD 3' mRNA-Seq Library Prep Kits – with unique dual indexing	Lexogen	113-115 & 129-131
Agilent RNA 6000 Nano Kit	Agilent	5067-1511
Agilent High Sensitivity DNA Kit	Agilent	5067-4626
TMT10plex™ Isobaric Label Reagent Set	Thermo Scientific™	90406
iST-NHS kit	PreOmics GmbH	P.O.00026
RNA Clean & Concentrator-5 kit	Zymo Research	R1013
FD Rapid GolgiStain™ Kit	FDNeurotechnologies Inc.	PK401
RNAscope® Intro Pack for Multiplex Fluorescent Reagent Kit v2- Mm	ACD	323136
Deposited data		
Metabolomics & Lipidomics data	This paper	MetaboLights: MTBLS6578
Proteomics data	This paper	iProX: PXD038454
Bulk RNA sequencing data	This paper	GEO: GSE218713
Single cell RNA sequencing data	Di Bella et al.[72]; Yuan et al.[73]	GEO: GSM4635077, GEO: GSM4635080, GEO: GSM4635081, GEO: GSM4635078, GEO: GSM4635079, GEO: GSM5277845, GEO: GSE204759
Code	This paper	zenodo: https://doi.org/10.5281/zenodo.7358062
Experimental models: Organisms/strains		
Mouse: B6.129P2-Slc7a5tm1.1Daca/J	The Jackson Laboratory	027252; RRID:IMSR_JAX:027252
Mouse: B6.Cg-Tg(Tek-cre)1Ywa/J	The Jackson Laboratory	008863; RRID:IMSR_JAX:008863
Mouse: B6.129S2-Emx1tm1(cre)Krj/J	The Jackson Laboratory	005628; RRID:IMSR_JAX:005628
Mouse: Gt(ROSA)26Sortm4(ACTB-tdTomato,-EGFP)Luo/J	The Jackson Laboratory	007576; RRID:IMSR_JAX:007576
Mouse: MADM-8-GT	Contreras et al.[43]	N/A
Mouse: MADM-8-TG	Contreras et al.[43]	N/A
Oligonucleotides		
qPCR primer_human: Q_SLC7A5_In2-3F: CGCTCATCAGATAGCCAGGAAA	This paper	N/A
qPCR primer_human: Q_SLC7A5_In2-3R: TTGAAGCCAAACAGGAGACAGG	This paper	N/A
qPCR primer_human: Q_SLC7A5_In4-5F: GTGTGTCCTTGAGCACGGTTTC	This paper	N/A
qPCR primer_human: Q_SLC7A5_In4-5R: CCTGAGAAATGGGGATTCTTCG	This paper	N/A
qPCR primer_human: Q_SLC7A5_In5-6F: CAGAGGAAGTGTCTGGGGATCA	This paper	N/A
qPCR primer_human: Q_SLC7A5_In5-6R: CCACTCTGTGGCAGACTCCAAT	This paper	N/A
qPCR primer_human: Q_SLC7A5_In5-6F2: AGTCCAGGGCAGAGGTCATTTTA	This paper	N/A
qPCR primer_human: Q_SLC7A5_In5-6R2: GAGTCAGAGCTTGTTCAGTAGGAAGC	This paper	N/A

Continued

REAGENT or RESOURCE	SOURCE	IDENTIFIER
qPCR primer_human: Q_SLC7A5_In7-8F ACCACATTTGGGTTAAGGACAGG	This paper	N/A
qPCR primer_human: Q_SLC7A5_In7-8F AGGTCCTGGCCCTTGCTTACTA	This paper	N/A
qPCR primer_human: Q_SLC7A5_3UTR_F: CCAAGAAAGCAGGGCTTCCTAA	This paper	N/A
qPCR primer_human: Q_SLC7A5_3UTR_R: GGTTTAATGTGCGTCTCCATGC	This paper	N/A
qPCR primer_human: Q_KLHDC4_In1-2F: TGACCTTGGGGTTGAGTGTTCT	This paper	N/A
qPCR primer_human: Q_KLHDC4_In1-2R: AGGGACAAAGGACTGTGGTCAA	This paper	N/A
qPCR primer_human: Q_KLHDC4_In4-5F: AGTGAATGACCTGTGTGGTCAGTG	This paper	N/A
qPCR primer_human: Q_KLHDC4_In4-5R: CTATGGGAGAAAAAGCCCTGGA	This paper	N/A
qPCR primer_human: Q_KLHDC4_In5-6F: TGGAGTCTGTGGAACTGTGAAGTG	This paper	N/A
qPCR primer_human: Q_KLHDC4_In5-6R: CCATGGAATGTCAACCAGAAGC	This paper	N/A
qPCR primer_human: Q_KLHDC4_In7-8F: TGAGCAAGTAGAGGTGGCTTGG	This paper	N/A
qPCR primer_human: Q_KLHDC4_In7-8R: GGTGAGCAGAAGGACAAGGACA	This paper	N/A
Genotyping primer – Slc7a5fl; forward CCA TCT CGG CAG TTC AG GC	Sinclair et al.[74]	N/A
Genotyping primer – Slc7a5fl; reverse GGT GCT TTG CTG AAG GCA GGG	Sinclair et al.[74]	N/A
Genotyping primer – recombination of floxed-exon1 (Slc7a5); forward CAG CTC CTT TCT CCA GTT AAG C	This paper	N/A
Genotyping primer – recombination of floxed-exon1 (Slc7a5); reverse GAC AGC CTG AAG TAA AAT TCC C	This paper	N/A
Genotyping primer – Cre recombinase; forward GTC CAA TTT ACT GAC CGT ACA CC	This paper	N/A
Genotyping primer – Cre recombinase; reverse GTT ATT CGG ATC ATC AGC TAC ACC	This paper	N/A
RNAscope® Probe - Mm-Slc7a5-E1 - musculus solute carrier family 7 member 5 (Slc7a5) mRNA	ACD	472571
RNAscope® Probe - Mm-Slc7a5 - Mus musculus solute carrier family 7 member 5 (Slc7a5) mRNA	ACD	461031
TSA Vivid650	Tocris	7536
Software and algorithms		
VarSeq	Golden Helix Inc®	https://www.goldenhelix.com/products/VarSeq/
ZEN Digital Imaging for Light Microscopy	Zeiss	http://www.zeiss.com/microscopy/en_us/products/microscope-software/zen.html#introduction
ImageJ	Schneider et al.[75]	https://imagej.nih.gov/ij/

(Continued on next page)

Continued

REAGENT or RESOURCE	SOURCE	IDENTIFIER
Graphpad Prism 9.0	Graphpad	https://www.graphpad.com/scientific-software/prism/
Imaris Microscopy Image Analysis Software	Oxford Instruments	https://imaris.oxinst.com/
MS-DIAL	Tsugawa et al.[76]	N/A
TraceFinder	Thermo Scientific™	https://www.thermofisher.com/at/en/home/industrial/mass-spectrometry/liquid-chromatography-mass-spectrometry-lc-ms/lc-ms-software/lc-ms-data-acquisition-software/tracefinder-software.html
Compound Discoverer Software 3.0	Thermo Fisher Scientific™	https://www.thermofisher.com
MaxQuant (1.6.17.0)	Tyanova et al.[77]	https://www.maxquant.org/
limma package v4.2	Ritchie et al.[78]	http://www.bioconductor.org
topGO v2.50.0	N/A	http://www.bioconductor.org
R v4.1.2	N/A	https://www.r-project.org/
Seurat v4.1.0	Hao et al.[79]	http://www.bioconductor.org
GenBinomApps v1.2	N/A	https://cran.r-project.org/package=GenBinomApps
Origin 2018 (64 bit)	Origin Lab	https://www.originlab.com/
Clampfit v10.7	Molecular Devices	https://support.moleculardevices.com/s/article/Axon-pCLAMP-10-Electrophysiology-Data-Acquisition-Analysis-Software-Download-Page
Clampex v10.7	Molecular Devices	https://support.moleculardevices.com/s/article/Axon-pCLAMP-10-Electrophysiology-Data-Acquisition-Analysis-Software-Download-Page
NeuronStudio	Wearne et al.[80]	N/A
Galaxy web platform	Afgan et al.[81]	https://usegalaxy.org/
STAR v2.5.4	Dobin et al.[82]	https://github.com/alexdobin/STAR
DESeq2 v1.34.0	Love et al.[83]	http://www.bioconductor.org
GOstats v2.36.0	Falcon et al.[84]	http://www.bioconductor.org
FASTX toolkit v0.0.14	Hannon Lab	http://hannonlab.cshl.edu/fastx_toolkit/
Huygens Professional software v15.0	Scientific Volume Imaging	https://svi.nl/HomePage
EthoVision XT 11.5	Noldus	https://www.noldus.com/ethovision-xt
Python 3.9.4	conda	https://www.python.org/
Scikit-learn 1.1.2	Pedregosa et al.[85]	https://scikit-learn.org/stable/index.html
Pandas 1.3.5	McKinney et al.[86]	https://pandas.pydata.org/
numpy 1.22.4	Harris et al.[87]	https://numpy.org/
statsmodels 0.13.1	Seabold et al.[88]	https://www.statsmodels.org/stable/index.html
Scipy 1.7.3	Virtanen et al.[89]	https://scipy.org/
Seaborn 0.11.2	Waskom et al.[90]	https://seaborn.pydata.org/
Python-ternary 1.0.8	PyPI	https://github.com/marcharper/python-ternary
thefuzz 0.19.0	PyPI	https://github.com/seatgeek/thefuzz
Python-levenshtein 0.12.2	PyPI	https://github.com/ztane/python-Levenshtein/
Matplotlib 3.5.2	Hunter et al.[91]	https://matplotlib.org/
Jupyterlab 3.5.0	PyPI	https://jupyter.org/
Other		
CFX Connect™ Real-Time PCR Detection System	Bio-Rad	1855201

(Continued on next page)

Continued

REAGENT or RESOURCE	SOURCE	IDENTIFIER
Immobilon®-P PVDF Membrane	Millipore	IPVH00010
Tissue-Tek® O.C.T. Compound	Sakura® Finetek	4583
DAKO fluorescent mounting medium	Dako	S3023
DPX Mountant for histology	Sigma-Aldrich	06522
SuperFrost Plus™ Adhesion slides	Epredia™	10149870
ProLong™ Gold Antifade Mountant	Invitrogen™	P36930
Disposable pestles	Bel-Art®	BAF199230001
iHILIC®-(P) Classic, PEEK column, (100mm x 2.1mm, 5µm) with a precolumn	HILICON	160.102.0520
ACQUITY UPLC HSS T3 column (150 mm x 2.1 mm; 1.8 µm)	Waters Corporation	186009492
50-ml TPP® TubeSpin Bioreactor tubes	Merck	Z761028
TC20 Automated Cell Counter (Bio-Rad)	Bio-Rad	N/A
Atlantis Premier BEH Z-HILIC column (2.1 mm x 100 mm, 1.7 µm)	Waters Corporation	186009979
ACQUITY Premier CSH C18 column (2.1 mm x 100 mm, 1.7 µm)	Waters Corporation	186009461
Protein A Magnetic Beads	Abcam	ab214286
DynaMag™-2 Magnet	Invitrogen™	12321D
Protein Extraction beads	Diagenode	C20000021
13.2ml Thinwall Ultra-Clear™ Tubes	Beckmann Coulter	344059
GEN1 uPAC column	Pharmafluidics	N/A
BX-51WI microscope	Olympus	N/A
QIClickTM charge-coupled device camera	Q Imaging Inc.	N/A
Nikon Eclipse Ti2	Nikon	N/A
LSM800 Confocal	Zeiss	N/A
SlideScanner VS120	Olympus	N/A
Sliding Microtome SM2010R	Leica	N/A
Cryostat Cryostar NX70	Thermo Scientific™	N/A
Vibratome Leica VT 1200S	Leica	N/A
BioWave Pro+ microwave	Pelco	36700
Ultramicrotom UC7	Leica	N/A
Amersham Imager 680	GE Healthcare	N/A

RESOURCE AVAILABILITY

Lead contact
Further information and requests for resources and reagents should be directed to and will be fulfilled by the lead contact, Gaia Novarino (gaia.novarino@ista.ac.at).

Materials availability
This study did not generate new unique reagents.

Data and code availability
- Metabolomics and lipidomics data have been deposited at MetaboLights, proteomics data at iProX and RNA-sequencing data at GEO. All data are publicly available as of the date of publication. Accession numbers or unique identifiers are listed in the key resources table. This paper analyses existing, publicly available data. These accession numbers for the datasets are listed in the key resources table.
- All original code has been deposited at Zenodo and is publicly available as of the date of publication. DOIs are listed in the key resources table.
- Any additional information required to reanalyze the data reported in this paper is available from the lead contact upon request.

EXPERIMENTAL MODEL AND SUBJECT DETAILS

Animals

All animal protocols were approved by the Institutional Animal Care and Use Committee at ISTA and by the Bundesministerium für Bildung, Wissenschaft und Forschung, Austria (approval number: BMBWF-66.018/0015-V/3b/2019). All experiments were performed on mice ranging from embryonic day (E) 12.5 to postnatal day (P) 90. Embryonic time points were determined by plug checks after timed matings, defining E0.5 as the morning after copulation. Animals were kept on a 12 h light/dark cycle (lights on at 7:00 am) and housed in groups of 3-4 animals per cage, with food and water available ad libitum. Experiments were carried out under specific pathogen-free conditions and the health status of the mouse lines was routinely checked by a veterinarian. All transgenic mouse lines were back-crossed into C57BL/6J background >2 times. Experiments were carried out using littermate pairs of the same sex. Both, males and females were used for experiments. The *Slc7a5*$^{fl/fl}$;*Emx1-Cre* conditional line was generated by crossing *Slc7a5*$^{fl/fl}$ mice with animals expressing the Cre recombinase under the *Emx1* promoter (B6.129S2 (Emx1tm1cre)Krj/J). In the *Slc7a5*^{fl} (B6.129P2-Slc7a5tm1.1Daca/J) mouse line, exon 1, including the initiation codon, is flanked by two loxP sites. *Slc7a5*$^{fl/fl}$;*Tie2-Cre* conditional animals were generated by crossing *Slc7a5*$^{fl/fl}$ with *Tie2-Cre* mice. The generation of the *Tie2-Cre*, *Emx1-Cre* and *Slc7a5*^{fl} lines has been previously described.[13,74,92] In addition, for this study we generated mosaic *Slc7a5*-MADM (*MADM-8*$^{GT/TG,Slc7a5}$;*Emx1*$^{-Cre/+}$) mice with sparse green (eGFP$^+$) homozygous *Slc7a5*$^{-/-}$ mutant, yellow (GFP$^+$/tdTomato$^+$) heterozygous *Slc7a5*$^{+/-}$, and red (tdTomato$^+$) *Slc7a5*$^{+/+}$ wild-type cells in an otherwise unlabeled heterozygous background. To this end, *Slc7a5*^{fl} were genetically linked to the MADM-8 TG cassette via meiotic recombination as described previously.[43] The primer sequences for MADM-GT and MADM-TG cassettes for MADM-8 can be found in Contreras et al.[43] The sequence of all the other genotyping primers is given in the key resources table.

Human subjects

For the human subjects (patients and their parents), written informed consent and collection of data and samples were obtained according to a protocol approved by the Ethics Committee of the Medical University of Vienna (protocol number 1443/2020). Family 130 with two affected daughters (patients 130-1 and 130-2) was referred to genetic counseling and testing in the Institute of Medical Genetics of Medical University Vienna through a supporting Centre for Developmental Disabilities in Vienna. Trio-WES analysis of both siblings and their parents identified compound heterozygous pathogenic variants in the *SLC7A5* gene: the previously described and functionally assessed missense variant c.1124C>T, p.(Pro375Leu)[6] and a novel intragenic deletion of exons 5 to 10. Parents are heterozygous carriers. Patient 130-1 was born at term and showed microcephaly at birth (head circumference (HC) of 31 cm, -3 SD). Birth weight and height were normal. The microcephaly deteriorated progressively to -5 SD (HC of 36.6 cm) at the age of 7 months. A premature closure of fontanelles was observed from the age of 8 months. A surgical treatment (frontobasal advancement) of presumed craniosynostosis was performed at the age of 12 months. The patient displayed pronounced muscular hypotonia and motor delay. At the age of 3 years, the patient developed seizures, which could be successfully treated with valproate. Brain MRI showed, in addition to microcephaly, pontocerebellar and corpus callosum hypoplasia. At the time of the first genetic counseling, patient 130-1 was 9 years and 4 months old and presented with severe microcephaly and growth retardation (HC 43 cm, -7 SD; height 109 cm, -4.5 SD and weight 17.1 kg, -4 SD). The patient could sit independently and stand with help but could not walk and the speech was absent. The history and presentation of the younger sibling, patient 130-2, are essentially similar. The microcephaly was diagnosed at birth, progressively deteriorating to -4.5 SD by the age of 6–7 months, followed by premature closure of fontanelles. Pontocerebellar and corpus callosum hypoplasia were detectable by brain imaging. At genetic counseling, patient 130-2 was 4 years and 4 months old and displayed severe microcephaly (-6 SD), growth retardation (-5 up to -6 SD), global developmental delay (independent sitting possible, no walking, absent speech) and autistic features. The first seizures occurred at the age of 6 years and are controlled with anticonvulsive treatment. Before WES analysis an aCGH (Microarry-based Comparative Genomic Hybridization) was carried out, providing inconspicuous results for both patients.

METHOD DETAILS

Whole-exome sequencing analysis of patient samples

Whole-exome sequencing: Whole-exome sequencing was performed for both affected siblings and their healthy unrelated parents (extended Trio-WES). DNA samples were prepared following the workflow of the TruSeq Exome Library Kit (Illumina) for the enrichment of exonic regions. The final library was paired-end sequenced on an Illumina NextSeq500 sequencer. Sequencing reads were aligned to GRCh37/hg19 using the Burrows Wheeler Aligner (BWA-MEM) and further processed in house according to GATKs best practice protocol for calling single nucleotide variants, insertions and deletions. The evaluation of the called variants was performed using the program VarSeq from Golden Helix Inc®. Variants were classified according to the American College of Medical Genetics and Genomics (ACMG) guidelines.[93] In addition, a copy number variation (CNV) analysis was performed with the VarSeq software by comparing the calculated coverage of each sequenced sample of Family 130 to the coverage data of previously analyzed in-house samples. Quantitative PCR (qPCR): To verify the identified multiexonic deletion of *SLC7A5* a quantitative PCR (qPCR) was performed using CFX Connect™ Real-Time PCR Detection System (Bio-Rad) with primers spanning the deleted region. All primers were purchased from Eurofins Genomics. The specificity of each primer set was monitored by a dissociation curve. PCR reactions were performed in triplicate and normalized to *PAPD5* and *PRKD1*.

Immunofluorescence

Immunofluorescent staining of adult mouse brain: Adult littermate animals were anesthetized and transcardially perfused with 4% paraformaldehyde (PFA). After dissection, brains were post-fixed in 4% PFA overnight and dehydrated using 30% sucrose (in 1X phosphate buffered saline (PBS)). Dehydrated brains were sectioned at 30-40 μm on a Sliding Microtome SM2010R (Leica). Adult brain sections were stained free-floating. No antigen retrieval was performed unless specifically recommended in the primary antibody datasheet. Sections were washed in 1X PBS and blocked with 4% normal donkey or goat serum in 0.3% Triton X-100. Primary antibodies were diluted in blocking solution and incubated overnight on a horizontal shaker at 4°C. After 14-16h, the sections were washed and a species-specific secondary antibody was added for 2 h at room temperature (RT). For nuclear counterstaining, 300 nM DAPI (Life Technologies) in 1X PBS was applied. Sections were mounted on SuperFrost Plus™ Adhesion slides (Epredia™) using DAKO fluorescent mounting medium (Dako). Immunofluorescent staining of embryos and early postnatal brain: In brief, embryos were decapitated and the head was immersion-fixed for 24h in 4% PFA at 4°C. Pups (P0-P10) were decapitated and the brain was dissected. After dissection, the brain was immersion-fixed as described above. After fixation the samples were dehydrated in 30% sucrose (in 1X PBS) and embedded in Tissue-Tek® O.C.T. Compound (Sakura® Finetek). Brains were sliced on a CryoStar NX70 cryostat (Thermo Scientific™) and directly mounted on SuperFrost Plus™ Adhesion slides (Epredia™). Immunofluorescence stainings were performed directly on the slides using a humidity chamber. The detailed staining procedure is stated in the section above. Quantification: To examine cortical layering, the thickness of Cux1+ cell layer and the Ctip2+ cell layer was measured at three defined points of each cortical hemisphere (n= 3 littermate animals per genotype, at least 4 images per mouse). The density of upper or lower layer neurons was quantified by normalizing the number of Ctip2+ or Cux1+ cells to the total number of DAPI+ cells within a defined square. To assess the number of apoptotic cells, Cl-Caspase-3+ cells were quantified in coronal brain sections. The number of apoptotic cells located in the cortex was normalized to the total number of Cl-Caspase-3+ cells quantified in subcortical regions (n= 3 littermate animals per genotype, at least 5 images per mouse). To assess the number of inhibitory neurons, the number of Parvalbumin+ cells was quantified per cortical layer and normalized to the absolute number of Parvalbumin+ cells per cortical column (n= 3 littermate animals per genotype, at least 5 images per mouse). Potential changes in astrocyte and microglia numbers were monitored by quantifying the number of Gfap+ or Iba1+ cells per cortical column. The numbers were normalized to the size of the selected area (n= 3 littermate animals per genotype, at least 5 images per animal). Image acquisition: Images were acquired using a Zeiss LSM800 inverted confocal microscope and analyzed in ImageJ.[75]

Immunohistochemistry stainings

Nissl staining: Adult animals were transcardially perfused with 4% PFA. The brains were dissected and post-fixed overnight in 4% PFA at 4°C. P0-1 brains were immersion fixed in 4% PFA for 24h at 4°C. The fixation was followed by a dehydration step in 30% sucrose (in 1X PBS). P0-1 coronal sections were obtained at the CryoStar NX70 cryostat (Thermo Scientific™). Adult coronal sections at 40 μm thickness were obtained using a Sliding Microtome SM2010R (Leica). Sections were mounted on SuperFrost Plus™ Adhesion slides (Epredia™) and air-dried for >2h at room temperature. Sections were cleared for 10 min using RotiHistol (Carl Roth) and dehydrated using graded absolute ethanol (abs. EtOH) steps: 30%, 50%, 70%, 90%, 96%, 90% and abs. EtOH (3-5 min each). The section were stained using 1% Cresyl Violet (Sigma Aldrich) in abs. EtOH. After staining, slices were de-stained using 2% acetic acid in abs. EtOH. After several washes in EtOH, sections were immersed in RotiHistol (Carl Roth) and mounted using DPX mountant (Sigma Aldrich). Image acquisition: Images were obtained at an Olympus slide scanner VS120 and quantified using ImageJ (n=3 per genotype, at least 4 images per mouse).

Golgi-Cox staining: Golgi-Cox staining was performed using the FD Rapid GolgiStain Kit™ (FDNeurotechnologies). After three weeks of impregnation in the staining solutions provided by the kit, brains were sliced coronally (120 μm) using a Vibratome VT 1200S (Leica). The sections were mounted onto 1% gelatinized slides. After drying the samples were dehydrated through graded EtOH steps and cleared using RotiHistol (Carl Roth). Coverglasses were mounted with DPX mountant (Sigma Aldrich). Image acquisition: A Nikon Eclipse Ti2 microscope (40x objective) was used to acquire images of LII/III pyramidal neurons of the somatosensory cortex (12 neurons per brain, n=3 per genotype). For analysis, single pyramidal neurons were manually traced using Imaris software x64 v9.3.1, followed by quantification of average filament area, filament length and Sholl intersections.

RNAscope Assay

Spatial gene expression analysis was performed using the RNAscope®[94] Multiplex Fluorescent v2 Assay (ACD) kit including specific probes targeting Slc7a5 mRNA (ACD; Cat.# 472571 and Cat.# 461031). Sample preparation: P2 mice were decapitated and the brain was dissected rapidly on ice. The cerebellum was removed and the brain was embedded in pre-cooled Tissue-Tek® O.C.T. Compound (Sakura® Finetek) and stored at -80°C until further used. Tissue was sliced at 10 μm at a CryoStar NX70 cryostat (Thermo Scientific™) and directly mounted on SuperFrost Plus™ Adhesion slides (Epredia™). Sections were stored at -80°C. RNAscope® assay: The assay was performed according to the instructions provided by the RNAscope® Multiplex Fluorescent v2 Assay kit. In brief, sections were fixed in 4°C cold 4% PFA and further pre-treated employing a H_2O_{2-} and protease-digestion. After the pre-treatment, sections were incubated with the probe targeting the mRNA of interest. Probes were further hybridized to a cascade of signal amplification molecules, followed by a hybridization with a dye-labelled probe (Akyoa Sciences). After the hybridization steps, sections were stained with a nuclear counterstain and mounted using ProLong™ Gold Antifade Mountant (Invitrogen™). Image acquisition: Images were acquired at a LSM800 confocal microscope using 10x, 20x and 65x objectives.

Isolation and quantification of MADM-labelled tissue

Tissue harvesting: P0 and P5 animals were decapitated and the brain was isolated and fixed in 4% PFA overnight at 4°C. From P6 onwards, mice were transcardially perfused using 4% PFA. Brains were post-fixed in 4% PFA overnight to ensure complete fixation. Brains were cryopreserved with 30% sucrose in 1X PBS for approximately 48 h and were then embedded in Tissue-Tek® O.C.T. Compound (Sakura® Finetek). 40 μm coronal frozen sections were cut on a Sliding Microtome SM2010R (Leica), and mounted on SuperFrost Plus™ Adhesion slides (Epredia™). Next, sections were stained with 300 nM DAPI (Life Technologies). The coverglass was mounted using DAKO fluorescent mounting medium (Dako). Image acquisition: Images were acquired using a Zeiss LSM800 inverted confocal, an Olympus Slidescanner VS120 or a Nikon Eclipse Ti2. Images were post-processed and analyzed in Zen Blue 2.6 software and ImageJ. Quantification: The number of MADM-labelled green, red and yellow neurons within the somatosensory cortex was quantified according to their localization within the different cortical layers. The ratio between green and red neurons was calculated per animal (>10 hemispheres per animal; n=6 mice per genotype).

Electron microscopy

Sample preparation: P2 mice were decapitated and the brain was dissected, washed in 0.1M PB, dropped into EM suitable fixative (2.5% glutaraldehyde and 2% PFA in 0.1M PB) and fixed for 10 min using a BioWave Pro+ microwave (Pelco). Fixed brains were sliced at a Leica Vibratome VT 1200S (100 μm). Sections were placed in 1% osmium tetroxide in 0.1M PB solution, followed by 1% uranyl acetate in 50% EtOH. This step was followed by a dehydration protocol with ascending EtOH concentration (50%, 70%, 90%, 96% and 2x 100%). Samples were then placed into propylene oxide, followed by consecutive incubations in 1:2, 1:1 and 2:1 Durcupan:propylene oxide solutions and an overnight incubation in Durucupan. After the treatment, samples were mounted on siliconized coverslips, placed on a heating plate for 30 min at 37°C, followed by 48 h at 60°C to allow the polymerization of the resin. The region of interest (layer II/III somatosensory cortex) was cut and re-embedded in a resin block for further slicing. Ultrathin serial section (70 nm) ultrathin serial sections were cut using an UC7 ultramicrotom (Leica Microsytems), collected on formvar-coated copper-slot grids and examined in FE-SEM. Image acquisition: Images were acquired on a Tecnai T10 transmission electron microscope at 24000X magnification.

Western Blot

Sample preparation: Mice at different developmental time points were decapitated, the cortex was dissected on ice, snap frozen and stored at -80°C until further used. For protein extraction cortices were homogenized in ice-cold lysis buffer (20mM Tris-HCl pH:8, 137mM NaCl, 10% Glycerol, 0.1% NP-40, 1mM EDTA, 9.5mM NaF, 10mM PPi (Sodium pyrophosphate dibasic), 1mM Na_3Vo_4) plus cOmplete™ Protease Inhibitor (Roche). Samples were kept on ice for 20 min followed by a centrifugation step at 500g for 10 min at 4°C. The supernatant was transferred into a fresh tube and centrifuged at max speed for 20 min at 4°C. The lysates were again transferred into a fresh tube, aliquoted and stored at -80°C. Protein concentration was determined using the Pierce™ BCA Protein Assay Kit (Thermo Fisher). Western Blot assay: Samples were diluted with 2X Laemmli buffer (10% SDS, 20% Glycerol, 100mM Tris-Cl (pH 6.8), Bromophenol blue, 3% Pierce™DTT), denatured at 65°C for 10 min and separated using 8-12% SDS-PAGE gels. 25-50 μg of protein per sample were loaded. Proteins were blotted to an Immobilon®-P PVDF Membrane (Merck) for 1-2 h at 4°C with 300 mA constant current using a Bio-Rad immunoblot apparatus. The membranes were blocked using 2.5% Bovine serum albumin (BSA) in 1X Tris-buffered Saline + 0.1% Tween (TBST) for 1h at room temperature. Primary antibodies were diluted in blocking solution and the membranes incubated overnight at 4°C on a horizontal shaker. After several washes with 1X TBST, the membranes were incubated for 1h at RT with secondary anti-IgG antibodies coupled to horseradish peroxidase (HRP) diluted in blocking solution. Signal detection: Detection was carried out using Pierce™ ECL Western Blotting Substrate (ThermoFisher) or SuperSignal™ West Pico PLUS Chemiluminescent Substrate (ThermoFisher) in combination with the Amersham Imager 680 (GE Healthcare).

Untargeted metabolomics of whole cortical tissue

Sample preparation: Mice were decapitated and the brains dissected on ice. Cortices were collected in 2ml Eppendorf tubes, washed with 1ml ice-cold 1X PBS, weighed and stored at -80°C until further processed. Metabolite extraction: Ice-cold solvent mixture (methanol:acetonitrile:H2O (2:2:1, v/v) MS-grade; cooled to -20°C) was added to the tissue and homogenized for 1 min using Bel-Art® disposable pestles. The homogenization was followed by a sonication step of 5 min in a water bath sonicator. The samples were incubated for 1 h at -20 °C, followed by a centrifugation step at 14,000g for 3 min at 4°C. The supernatant was transferred into a 1.5-ml microcentrifuge tube and stored at -20°C and the pellet was re-suspended in ice-cold solvent (methanol:acetonitrile:H2O (2:2:1, v/v)). After vortexing, the pellet was incubated for another hour at -20°C and then centrifuged at 14,000g for 3 min at 4°C. The resulting supernatant was combined with the supernatant obtained in the previous centrifugation step and incubated for 2 h at -20°C. This was followed by a last centrifugation step at 14,000g for 10 min at 4°C. The supernatant was again transferred to a new 1.5-ml microcentrifuge tube, snap frozen and stored at -80°C. Sample analysis: Extracts were thawed on ice and centrifuged for 5 min at 15,000g. 10 μL of each sample were pooled and used as a quality control (QC) sample. Samples were randomly assigned into the autosampler and injected on the respective phase system. For HILIC (hydrophilic interaction chromatography), an iHILIC®-(P) Classic, PEEK column, (100mm x 2.1mm, 5μm) with a precolumn (HILICON) was used. A 26 min gradient from 90% A (acetonitrile) to 80% B (25 mM ammonium bicarbonate in water) was used, employing a flow rate of 100 μL/min delivered

through an Ultimate 3000 HPLC system (Thermo Fisher). After the analysis by HILIC-MS/MS, samples were analyzed with reversed phase chromatography (RP). Here, an ACQUITY UPLC HSS T3 column (150mm x 2.1mm; 1.8 μm) with VanGuard precolumn (Waters Corporation) was used. A 20 min gradient of 99% A (0.1% formic acid in water) to 60% B (acetonitrile with 0.1% formic acid) was employed using the same HPLC system and flow rate. In both cases, metabolites were ionized via electrospray ionization in polarity switching mode after HILIC separation and in positive polarity mode after RP separation. Sample spectra were acquired by data-dependent high-resolution tandem mass spectrometry on a Q-Exactive Focus (Thermo Fisher Scientific™). The ionization potential was set to +3.5/-3.0 kV, the sheet gas flow was set to 20, and an auxiliary gas flow of 5 was used. Samples were analyzed in a randomized fashion and QC samples were additionally measured in confirmation mode to obtain additional MS/MS spectra for identification. Obtained data sets were processed by Compound Discoverer software v3.0 (Thermo Fisher Scientific™). Compound annotation was performed with a mass accuracy of 3 ppm for precursor masses and 10 ppm for fragment ion masses searched in public spectral databases as well as our in-house spectral library. Experimentally obtained retention times were used for the validation of metabolite identifications.

Targeted intracellular metabolomics

Sample preparation: P2 mice were decapitated, the cortices dissected on ice and the meninges and hippocampus removed. The tissue was dissociated according to the protocol provided by the Papain Dissociation System (Worthington Biochemical Corp.) kit to obtain a single cell suspension. In brief, cortices were moved to 50 ml TPP® TubeSpin Bioreactor tubes (Merck) and incubated in papain for 30 min at 37°C in a shaking water bath. After several dissociation steps, cells were pelletized at 200g for 8 min at room temperature and re-suspended in EBSS + 1%BSA. The cell suspension was stored on ice while the live cell count was determined using a TC20 Automated Cell Counter (Bio-Rad). Metabolite extraction: 1×10^6 cells per sample were transferred into a 1.5 ml Eppendorf tube and centrifuged at 200g for 8 min at 4°C using a tabletop centrifuge. The supernatant was removed and 100μl ice-cold solvent mixture (methanol:acetonitrile:H2O (2:2:1, v/v) MS-grade; cooled to − 20°C) was added to the pellet. The cells were mechanically homogenized with a P1000 pipette for 1 min and then sonicated for 5 min in a water bath sonicator. Samples were further processed as described for the untargeted metabolomics analysis and stored at -80°C until analyzed. Sample analysis: Polar metabolites were analyzed using HILIC-LC-MS/MS. Each sample was injected onto an iHILIC®-(P) Classic, PEEK column, (100mm x 2.1mm, 5μm) with a precolumn (HILICON). An Ultimate 3000 HPLC system (Dionex, Thermo Fisher Scientific™) was used, employing a flow rate of 100 μl/min and directly coupled to a TSQ Quantiva mass spectrometer (Thermo Fisher). A 15-minute gradient from 14% B to 80% B (A: 95% acetonitrile 5% 10 mM aqueous ammonium acetate; B: 5 mM aqueous ammonium bicarbonate) was used for separation. The following transitions were used for quantitation in the negative ion mode (2.8 kV): pyruvate: 87 m/z → 43 m/z, lactate: 89 m/z → 43 m/z, taurine: 124 m/z → 80 m/z, ketoleucine: 129 m/z → 85 m/z, α-ketoglutaric acid: 145 m/z → 101 m/z, AMP: 346 m/z → 79 m/z, IMP: 347 m/z → 79 m/z, ADP: 426 m/z → 134 m/z, ATP: 506 m/z → 159 m/z, NAD: 662 m/z → 540 m/z, NADH: 664 m/z → 408 m/z, NADP: 742 m/z → 620 m/z, NADPH: 744 m/z → 426 m/z, CoA: 766 m/z → 408 m/z, Acetyl-CoA: 808 m/z → 408 m/z and in the positive ion mode (3.5kV) GSH: 308 m/z → 408 m/z, GSSG: 613 m/z → 355 m/z and SAM: 399 m/z → 250 m/z. The remaining metabolites were quantified by reverse phase LC-MS/MS, injecting 1 μl of the metabolite extract onto a RSLC ultimate 3000 (Thermo Fisher) directly coupled to a TSQ Altis mass spectrometer (Thermo Fisher) via electrospray ionization. A Kinetex C18 column was used (100 Å, 150 x 2.1 mm), employing a flow rate of 80 μl/min. A 7-minute-long linear gradient was used from 99% A (1 % acetonitrile, 0.1 % formic acid in water) to 60% B (0.1 % formic acid in acetonitrile). Liquid chromatography-tandem mass spectrometry (LC-MS/MS) was performed by employing the selected reaction monitoring (SRM) mode of the instrument in the positive ion mode, using the transitions 156 m/z → 110 m/z (histidine), 175 m/z → 70 m/z (arginine), 241 m/z → 74 m/z (cystine), 76 m/z → 30 m/z (glycine), 133 m/z → 70 m/z (ornithine), 175 m/z → 74 m/z (asparagine), 106 m/z → 60 m/z (serine) 120 m/z → 74 m/z (threonine), 147 m/z → 84 m/z (lysine), 147 m/z → 130 m/z (glutamine), 148 m/z → 84 m/z (glutamic acid) 90 m/z → 4 m/z (alanine and sarcosine), 104 m/z → 84 m/z (GABA), 176 m/z → 159 m/z (citrulline), 116 m/z →70 m/z (proline), 118 m/z → 72 m/z (valine), 150 m/z → 133 m/z (methionine), 132 m/z → 86 m/z (isoleucine and leucine), 182 m/z → 136 m/z (tyrosine), 166 m/z → 103 m/z (phenylalanine), 205 m/z → 188 m/z (tryptophane), 134 m/z → 74 m/z (aspartic acid) 177 m/z →160 m/z (serotonin) and 154 m/z → 137 m/z (dopamine). For all transitions, the optimal collision energy was defined by analyzing pure metabolite standards. LC-MSMS chromatograms were interpreted using TraceFinder (Thermo Fisher). After LC-MS/MS analysis, retention times were verified by standard addition of pure compounds to arbitrarily selected samples, validating experimental retention times with the respective pure substances. Statistical analysis: Raw peak areas were normalized using the probabilistic quotient normalization method as described in Dieterle et al.[95] implemented using pandas 1.3.5[86] and numpy 1.22.4.[87] P-values were computed using an unpaired two-tailed t-test and corrected using the Benjamini-Hochberg procedure implemented in statsmodels 0.13.1.[88]

Parallel untargeted lipidomics and metabolomics

Sample preparation: P2 mice were decapitated, cortices dissected on ice and the meninges and hippocampus removed. The left hemisphere was immediately transferred into a 1.5ml Eppendorf-tube and snap frozen for whole tissue lipidomics/metabolomics. The right hemisphere was dissociated with the Papain Dissociation System (Worthington Biochemical Corp.) kit and used to obtain the cellular lipidome/metabolome. The dissociation protocol is described in the previous section. Lipid and metabolite extraction: For lipid and metabolite extraction, samples were treated as described in the section above. Ice-cold isopropanol:H2O (90% - 10%, v/v)

was used as a solvent. EquiSPLASH™ LIPIDOMIX® Quantitative Mass Spec Internal Standards (Avanti Polar Lipids) and Metabolomics Amino Acid Mix Standards (Cambridge Isotope Laboratories) were added as internal standards to the solvent. Sample analysis: LC-MS/MS analysis was performed on a Vanquish UHPLC system coupled to an Orbitrap Exploris 240 high-resolution mass spectrometer (Thermo Fisher Scientific™) in positive and negative ESI (electrospray ionization) mode. All experimental samples were measured in a randomized manner. Pooled quality control (QC) samples were prepared by mixing equal aliquots from each processed sample. Multiple QCs were injected at the beginning of the analysis in order to equilibrate the LC-MS system. A QC sample was analysed after every 5th experimental sample to monitor instrument performance throughout the analytical sequence. For determination of background signals and subsequent background subtraction, an additional processed blank sample was recorded. Data was processed using MS-DIAL[76] and raw peak intensity data was normalized via internal standards or total ion count of all detected analytes.[96] Feature identification was based on accurate mass, isotope pattern, MS/MS fragment scoring and retention time matching to an in-house library (metabolomics) and the MS-DIAL LipidBlast library (lipidomics). Analysis of untargeted metabolomics data: Chromatographic separation was carried out on an Atlantis Premier BEH Z-HILIC column (Waters; 2.1 mm x 100 mm, 1.7 μm) at a flow rate of 0.25 mL/min. The mobile phase consisted of water:acetonitrile (9:1, v/v; mobile phase phase A) and acetonitrile:water (9:1, v/v; mobile phase B), which were modified with a total buffer concentration of 10 mM ammonium acetate (negative mode) and 10 mM ammonium formate (positive mode), respectively. The aqueous portion of each mobile phase was pH-adjusted (negative mode: pH 9.0 via addition of ammonium hydroxide; positive mode: pH 3.0 via addition of formic acid). The following gradient (20 min total run time including re-equilibration) was applied (min/%B): 0/95, 2/95, 15/50, 14/60, 14.5/50, 16.5/50, 16.8/95, 20/95. Column temperature was maintained at 40°C, the autosampler was set to 4°C and sample injection volume was 5 μL. Analytes were recorded via a full scan with a mass resolving power of 120,000 over a mass range from 60 – 900 m/z (scan time: 100 ms, RF lens: 70%). To obtain MS/MS fragment spectra, data-dependant acquisition was carried out (resolving power: 15,000; scan time: 22 ms; stepped collision energies [%]: 30/50/150; cycle time: 600 ms). Ion source parameters were set to the following values: spray voltage: 4100 V / 3500 V, sheath gas: 30 psi, auxiliary gas: 5 psi, sweep gas: 0 psi, ion transfer tube temperature: 350°C, vaporizer temperature: 300°C. Analysis of untargeted lipidomics data: Chromatographic separation was carried out on an ACQUITY Premier CSH C18 column (Waters; 2.1 mm x 100 mm, 1.7 μm) at a flow rate of 0.3 mL/min. The mobile phase consisted of water:acetonitrile (40:60, v/v; mobile phase phase A) and isopropanol:acetonitrile (9:1, v/v; mobile phase B), which were modified with a total buffer concentration of 10 mM ammonium acetate + 0.1 % acetic acid (negative mode) and 10 mM ammonium formate + 0.1% formic acid (positive mode), respectively. The following gradient (23 min total run time including re-equilibration) was applied (min/%B): 0/15, 2.5/30, 3.2/48, 15/82, 17.5/99, 19.5/99, 20/15, 23/15. Column temperature was maintained at 65°C, the autosampler was set to 4°C and sample injection volume was 5 μL (dissociated cells) and 1 μL (tissue samples). Analytes were recorded via a full scan with a mass resolving power of 120,000 over a mass range from 200 – 1500 m/z (scan time: 100 ms, RF lens: 70%). To obtain MS/MS fragment spectra, data-dependant acquisition was carried out (resolving power: 15,000; scan time: 54 ms; stepped collision energies [%]: 25/35/50; cycle time: 600 ms). Ion source parameters were set to the following values: spray voltage: 3250 V / 3000 V, sheath gas: 45 psi, auxiliary gas: 15 psi, sweep gas: 0 psi, ion transfer tube temperature: 300°C, vaporizer temperature: 275°C.

Proteomic analysis

Sample preparation for the proteomics analysis of whole cortical tissue: P5 mice were decapitated, the cortices dissected on ice, the hippocampus was removed and the samples stored at -80°C until used for further steps. Sample preparation for the proteomics analysis of Slc7a5 co-immunoprecipitation from neural cell membranes: Lysates enriched for cell membranes were obtained based on the protocol modified from Lee et al.[97] Brief, P5 Slc7a5fl/fl;Tie2-Cre+ animals were used to ensure that the precipitated Slc7a5 is derived from neural cells-only. Animals were decapitated and the brain was dissected on ice. Hippocampus and meninges were removed. The cortex was homogenized in ice-cold solution A (pH 7.4; 5mM HEPES; 0.32M sucrose; 1mM NaHCO; 1mM MgCl; 0.5 mM CaCl; ddH₂O) using a teflon-homogenizer on ice. 150 μl of the fresh lysate was transferred into a separate tube and 1% NP-40 was added (=L1- whole lysate). The remaining sample was centrifuged in a table-top centrifuge at 1400 g for 10 min at 4°C. The supernatant was transferred to a fresh 1.5 ml tube. Solution A was added to the pellet and homogenized with a pipette. The homogenate was centrifuged at 700 g for 10 min at 4°C. The two supernatants were combined, transferred into 13.2ml Thinwall Ultra-Clear™ Tubes (Beckman Coulter) and centrifuged at 13.800x g (RCF) for 10 min using an OPTIMA-XPN 100 ultracentrifuge. 150μl of the supernatant + 1%NP-40 were transferred into a fresh tube (=S2- cytosolic fraction). To obtain the membrane fraction of the sample (=M1), the pellet was re-suspended in solution B (pH8.0; 6mM Tris-HCl, 0.32M sucrose; 1mM NaHCO; ddH₂O), mechanically homogenized with a pipette and 1% NP-40 was added. The protein concentration of L1, S2 and M1 fractions was determined using the Pierce™ BCA Protein Assay Kit (Thermo Fisher Scientific). The samples were snap-frozen and stored at -80°C. Only fraction M1 was further used for the co-immunoprecipitation experiment. Co-immunoprecipitation was performed using Protein A Magnetic beads (Abcam) and a DynaMag™-2 Magnet (Invitrogen™) rack. The beads were washed and equilibrated using IP-lysis buffer (50 mM Tris-HCl (pH 8.0); 120 mM NaCl; 0.5% NP-40; 1 mM EDTA). 800μg of total protein per sample were used as input. Crude lysates were pre-cleared to eliminate proteins, which unspecifically bind to the beads. In detail, the samples were incubated with pre-washed beads for 2 hrs on a rotating rack at 4°C. After incubation, a magnetic field was applied using the DynaMag™-2 Magnet rack to collect the pre-cleared lysate. During the 2hrs pre-clearing step, pre-washed beads were incubated in lysis buffer with either normal rabbit igG control (Cell Signaling Technologies) or the anti-LAT1 (Slc7a5) antibody (25μg of antibody per sample) rotating at 4°C. After 2 hrs the conjugated beads were washed twice

and re-suspended in IP-lysis buffer w/o NP-40 (50 mM Tris-HCl (pH 8.0); 120 mM NaCl; 1 mM EDTA). After this step, the actual pull-down was performed by incubating the pre-cleared lysate over night with i) beads conjugated to the primary anti-LAT1 (Slc7a5) antibody (IP+) and ii) beads conjugated to the IgG control (IP-) at 4°C on a rotating rack. On the next day, IP+ flow through was collected using the magnetic rack. The beads were washed using IP-lysis buffer and gently vortexed. The samples were moved on the magnetic rack again and the supernatant was removed. The beads were washed and re-suspended in IP-lysis buffer w/o NP-40. The IP+ and IP- samples were further used for mass spectrometry analysis. Mass spectrometry analysis: All samples were processed with the iST-NHS kit from PreOmics GmbH. Modified protocols for on-beads digest (lysis for 10 min at 60°C) or whole tissue (sonication for 10*30s in a Bioruptor sonicator in presence of 50 mg Protein Extraction beads (Diagenode)) were used for co-IP samples and tissue samples, respectively. Digestion time was 2h for samples from co-IP experiments, 3.5 h for tissue samples. Two TMT-10plex kits were used (lot VK306785 for the whole lysate dataset, lot WC306775 for the co-IP dataset). Samples were cleaned up and combined. The whole lysate TMT sample was fractionated by offline High pH Reversed Phase fractionation into 48 fractions (A: de-ionized water + 10 mM NH4OH; B: 90% LC-grade Acetonitrile + 10 mM NH4OH; flow: 0.15 mL/min; 0-4 min: 1% B, 115 min: 25%, 140 min: 40%, 148 min: 75%, maintained for 12 min, followed by 45 min equilibration at 1% B). Unfractionated co-IP samples and whole lysate fractions were vacuum-dried overnight then re-dissolved in LC-LOAD (co-IP samples) and sent for MS analysis. LC-MS/MS analysis: All samples were analyzed by LC-MS/MS on an Ultimate 3000 nano-HPLC (Dionex) coupled with a Q-Exactive HF (Thermo Fisher Scientific™). Chromatographic method: peptide samples were loaded onto a GEN1 uPAC column (Pharmafluidics; Thermo Fisher Scientific™); solvent A: H2O, 0.1% formic acid; solvent B: 80% acetonitrile in H2O, 0.08% formic acid; gradients: tissue fractions, 2% to 44% B in 60 min; co-IP dataset, 2% to 31% (155 min) then 44% B (180 min); Mass Spectrometry method: Data-Dependent acquisition (Full MS / dd-MS2); MS1: 1 microscan, 120,000 resolving power, 3e6 AGC target, 50 ms maximum IT, 380 to 1,500 m/z, profile mode; up to 20 data-dependent MS2 scans per duty cycle, excluding charges 1 or 8 and higher, dynamic exclusion window 10s (60 min gradient) or 60s (180 min gradients); isolation window 0.7 m/z, fixed first mass 100 m/z, resolving power 60,000, AGC target 1e5, maximum IT 100 ms, (N)CE 32. Data analysis: Each dataset was independently searched in MaxQuant[77] (1.6.17.0 for whole tissues, 2.0.1.0 for co-IPs) against a *Mus musculus* fasta database downloaded from UniProtKB. Fixed modification was set to $C_6H_{11}NO$. Variable modifications were set to include Acetyl (protein N-term), Oxidation (M), Gln->pyroGlu and Deamidation (NQ) and, for whole tissue, Phospho (STY). Match-between-runs and second peptides were set to active. All FDRs were set to 5% (whole tissue) and 1% (co-IPs). Each MaxQuant output evidence.txt file was then re-processed separately in R using in-house scripts. Evidence reporter intensities were corrected using the relevant TMT lot's purity table, scaled to parent peptide MS1 intensity and then normalized using the Levenberg-Marquardt procedure. The long format evidence table was consolidated into a wide format peptidoforms table, adding up individual values where necessary. Peptidoform intensity values were log_{10} transformed. Values were re-normalized (Levenberg-Marquardt procedure). Protein groups were inferred from observed peptidoforms, and, for each group, the estimated expression values across samples were calculated by averaging individual peptidoform log_{10} intensity vectors, scaling the vector to reflect the intensity level of the most intense peptidoform according to the best flyer hypothesis (phospho-peptides and their unmodified counterpart peptide were excluded). Peptidoform and protein group log_2 ratios were calculated: to the corresponding control sample (IP- performed on the same individual) for co-IPs, or to the average reference (WT) sample (whole lysate dataset). Statistical significance was tested with the limma package[78] Seurat v4.2, performing both a moderated t-test and an F-test. The Benjamini-Hochberg procedure was applied to compute significance thresholds at various pre-agreed FDR levels. Regardless of the test, protein groups with a significant p-value were deemed to be regulated if their absolute log_2 fold change (= logFC) was greater than 95% of control to average control logFC. During the analysis phase, two out of five mutant samples from the cortical lysates dataset behaved as outliers and were excluded from further analysis. Protein groups were annotated with GO terms, applying a term if it, or one of its offspring terms, was found among the annotations of any protein accession which could explain all peptides in the group. GO enrichment analysis was performed using an in-house script built around the topGO package v2.50.0, comparing separately for each contrast all up- or down-regulated proteins, or both, against the background of all identified protein groups.

Bulk RNA-sequencing of cortical tissue

Sample preparation: P1-P2 pups were decapitated and the brains were dissected on ice under RNAse free conditions. Total RNA of one cortical hemisphere was extracted using TRIzol™ Reagent (Invitrogen™) and chloroform (Sigma Aldrich), followed by centrifugation at 12000 g for 15 min at 4°C. The upper phase was transferred to a fresh tube and 1.5 volumes of 100% EtOH were added. Total RNA was purified by using the RNA Clean&Concentrator-5 prep Kit (Zymo Research). The samples were further treated with RQ1 RNase-Free DNase (Promega) as described in the kit instructions manual. RNA concentration and quality was assessed by using the NanoDrop spectrophotometer (Thermo Fisher Scientific) and the Bioanalyzer 2100 with the RNA 6000 Nano kit (Agilent). cDNA libraries were generated with the SENSE mRNA-Seq Library Prep Kit V2 (Lexogen) using 1.5 μg total RNA. The quality of the generated libraries was monitored by using the High Sensitivity DNA Analysis Kit (Agilent) and the Bioanalyzer 2100. Libraries were sequenced on an Illumina HiSeq 2500 instrument. Analysis: De-multiplexed raw reads were trimmed before alignment using the FASTX toolkit v0.0.14. Trimmed reads were aligned to the mouse genome using STAR[82] v2.5.4 (genome: GrCm38, gene annotation: Gencode release M8). Read counts per gene were quantified using STAR. The aligned sequencing data were uploaded to the public server at usegalaxy.org.[81] Differential expression analysis was performed in usegalaxy.org using the Bioconductor package

DESeq2[83] v1.34.0 using an FDR threshold of 0.05. Gene Ontology enrichment analysis was performed using the Bioconductor package GOstats[84] v2.36.0 with a p-value cutoff of 0.001 and conditional testing enabled.

Analysis of the untargeted metabolomics dataset

<u>Combining hydrophilic interaction and reversed phase chromatography results and filtering</u>: Measurement of metabolites was done by LC-MS using hydrophilic interaction liquid chromatography (HILIC) or reversed phase chromatography (RP). The two analyses returned overlapping metabolites. Assuming quantifications in RP would align with quantifications in HILIC, we combined HILIC and RP by adding to the HILIC data those metabolites that were detected by RP but not by HILIC. Subsequently, the combined data were filtered to retain only those metabolites that were mapped to a KEGG ID. Data visualization was performed using Seaborn v0.11.2[90] and Matplotlibs v3.5.2.[91] <u>Principal component analysis</u>: Principal component analysis was conducted in Python using sci-kit-learn v1.1.2.[85] <u>Metabolite time course analysis</u>: Time course analysis was conducted on the combined and filtered metabolomics data. In brief, the mean abundance of the metabolites in WT and KO at each time point was computed and resulting averages were normalized to values between 0 and 1 such that the maximum abundance over time is 1 and the minimum abundance over time is 0. This was done for each metabolite in each genotype separately. Differential dynamics of metabolites between the genotypes were assessed by computing the Pearson correlation coefficient r between normalized trajectories in WT and KO where metabolites with $r < 0.975$ were considered to show differing dynamics.[89] For visualization purposes metabolites were manually annotated to five main metabolic pathways. <u>Grouping of metabolites based on trajectories</u>: Normalized trajectories of WT and mutants were grouped using a gaussian mixture model (GMM) with six components (implemented in scikit-learn v1.1.2[85]). The optimal number of components was assessed with the Bayesian information criterion. <u>Ternary plot generation</u>: Raw time point values for each metabolite in the combined and filtered data were averaged over replicates and normalized to sum to 1. These values were then plotted using the python-ternary library v1.0.8. <u>Metabolic pathway enrichment</u>: For classical pathway enrichment analysis, list of pathway annotations of classes 'metabolism' and 'information processing' were retrieved from the Kyoto Encyclopedia of Genes and Genomes (KEGG). Enrichment analysis was conducted by assessing the significance of overlap between a given set of metabolites and a pathway with Fisher's exact test and subsequent multiple testing adjustment using the Benjamini-Hochberg procedure using an FDR of 0.05.

Analysis of single-cell RNA sequencing data

<u>Raw data</u>: DiBella et al.[72]: Raw data was obtained from GEO (developmental age given in brackets): GSM4635077 (E16), GSM4635080 (P1), GSM4635081 (P1), GSM4635078 (E18), GSM4635079 (E18), GSM5277845 (P4). Metadata was obtained from Broad Institute Single Cell Portal (https://singlecell.broadinstitute.org/single_cell on 03/2022). Cell types CThPN, SCPN were grouped with DL CPN. Yuan et al.[73]: Raw counts and meta data was obtained from GEO, accession number GSE204759. <u>Analysis</u>: All analyses were performed using R (v4.1.2) and Seurat[79] Neuron (v4.1.0). One Seurat object was created for each sample using function CreateSeuratObject with parameters: min.cells = 3, min.features = 200. Expression data was normalized using function NormalizeData with standard parameters. Where applicable (E18, P1 DiBella et al.[72]), replicates were combined prior to normalization. Expression of *Slc7a5* was identified as fraction of cells showing a normalized expression of Slc7a5 > 0, relative to the total number of cells in that cell type. Clopper-Pearson confidence intervals were calculated using function clopper.pearson.ci (package GenBinomApps v1.2) with parameters: alpha = 0.05, CI = "two.sided".

Electrophysiology

<u>Sample preparation</u>: Acute brain slices were obtained from P6-7 and P25-P26 mice. Coronal sections (300 μm) were prepared from primary somatosensory cortex. Animals were decapitated under isoflurane anesthesia and whole brains were rapidly removed from the skull and sectioned using a VT 1200S vibratome (Leica) in ice-cold cutting solution, containing (mM): 87 NaCl, 25 NaHCO₃, 2.5 KCl, 1.25 NaH₂PO₄, 10 glucose, 75 sucrose, 7 MgCl₂, 0.5 CaCl₂ (320 mOsm, 7.2-7.4 pH). Slices were allowed to recover at room temperature for at least 1 h in regular artificial cerebrospinal fluid (ACSF), containing (mM): 125 NaCl, 2.5 KCl, 1.25 NaH₂PO₄, 25 NaHCO₃, 25 glucose, 1 MgCl₂ and 2 CaCl₂ (320 mOsm, 7.2–7.4 pH). The ACSF was continuously oxygenated with 95% O2 and 5% CO2 to maintain the physiological pH. When older mice were tested (P25-26), slices were sectioned in ice-cold cutting solution containing (mM): 93 NMDG, 2.5 KCl, 1.2 NaH₂PO₄, 30 NaHCO₃, 20 HEPES, 25 glucose, 5 sodium ascorbate, 2 thiourea, 3 sodium pyruvate, 10 MgCl₂, 0.5 CaCl₂ (320 mOsm, 7.2-7.4 pH). Slices from P25-26 mice were recovered at 32C for 10-12 minutes in the same solution and then allowed to recover at room temperature for at least 1 h in regular ACSF. Slices were visualized under infrared-differential interference contrast (IR-DIC) using a BX-51WI microscope (Olympus) with a QIClickTM charge-coupled device camera (Q Imaging Inc.). <u>Recordings</u>: Patch pipettes (4-6 MΩ; World Precision Instruments) were pulled on a P-1000 puller (Sutter Instruments) and filled with the intracellular recording solution, containing (mM): 128 K-gluconate, 10 HEPES, 10 Na₂-phosphocreatine, 1.1 EGTA, 5 MgATP, 0.4 NaGTP (osmolarity adjusted to 295 mOsm with sucrose, 7.3-7.4 pH). Current clamp recordings were performed at room temperature (24 ± 1 °C) from layer II/III pyramidal neurons. When experiments were performed in mosaic-MADM animals, patch clamp from layer II/III was visually guided by fluorescent labeling of neurons to recognize wild type (tdTomato+) and knock-out (GFP+) pyramidal neurons in the same brain slice. <u>Analysis</u>: Membrane capacitance and resting membrane potential were determined immediately after the establishment of whole-cell configuration. Neuronal membrane potential was held at approximately -60 mV (P6-7 mice) or -70 mV (P25-26 mice) by constant current injection. Current steps ranging in amplitude from -40 to +50 pA (10 pA increments; 600 ms duration) were applied to estimate the *f – I* relationship. In current clamp experiments from P25-26

mice, current steps ranging in amplitude from -300 to +400 pA (50 pA increments; 600 ms duration) were applied to estimate the $f − I$ relationship. Properties of individual action potentials (APs) were determined from the first current step necessary to elicit at least one AP. Phase-plane plot analysis was performed to evaluate the dynamic changes of the membrane potential over time (dV/dt). The threshold was set as the voltage at which the first derivative of the voltage trace reached 20 V/s. Amplitude was calculated as the difference between the threshold and the peak. AP half-width was measured at half the difference between the firing threshold and the AP peak. The inter-spike interval (ISI) ratio was calculated as the ratio of the last ISI relative to the first. Current clamp recordings were filtered at 2 kHz, sampled at 20 kHz and acquired using a MultiClamp 700B amplifier and a Digidata 1550A. Recorded signals were analyzed off-line using the Clampfit 10 software (Molecular Devices).

Biocytin filling of neurons

Sample preparation: Acute brain slices were obtained from P6-7 mice, as described in the previous section. To specifically label pyramidal neurons from layer II/III of the somatosensory cortex, patch pipettes (4-6 MΩ; World Precision Instruments) were pulled on a P-1000 puller (Sutter Instruments) and filled with the intracellular recording solution, containing (mM): 128 K-gluconate, 10 HEPES, 10 Na2-phosphocreatine, 1.1 EGTA, 5 MgATP, 0.4 NaGTP and 0.5% biocytin (osmolarity adjusted to 295 mOsm with sucrose, 7.3-7.4 pH). We dialyzed neurons for 10-15 minutes by whole-cell patch clamp. After pipette removal, slices were immediately fixed in 4% PFA overnight at 4°C. For visualization of the biocytin filling, sections were blocked in 5% normal goat serum in 1X PBS for 45 min at RT, followed by incubation with Streptavidin Alexa Fluor™ 488 Conjugate overnight at 4°C. After the incubation step a nuclear counterstain was applied and the sections were mounted on SuperFrost Plus™ Adhesion slides (Epredia™) using Dako fluorescent mounting medium (Dako). Image acquisition: Fluorescently labeled neurons were imaged with a 40x objective at a Zeiss LSM800 inverted confocal microscope. Image analysis: Images were de-convoluted using Huygens Professional software in v15.0 (Scientific Volume Imaging). Quantification of spine density and morphology was performed in NeuronStudio.[80] Sholl analysis was performed after tracing the complete dendritic tree in Imaris software x64 v9.3.1.

Behavioral analysis

All behavioral tests were performed during the light period. Mice were habituated to the test room 24 h before each test. For all studies, sex-matched littermate pairs were employed. Equipment was cleaned between each trial with 70% EtOH. Mice were given 24 h to recover between different tests. All behavioral studies were performed starting with the least aversive task first and ending with the most aversive one. Behavioral tests were carried out with P55 to P65 animals. Open field test: Exploratory behavior in a novel environment was assessed in an open field arena (45cm (L) x 45cm (W) x 30cm (H)) made out of dark plexiglas. The animal was placed in the center of the arena and videotaped for 20 min. Locomotor activity (distance traveled and velocity) in the center or periphery of the arena, as well as rearing, were tracked and analyzed using the EthoVision XT 11.5 software (Noldus). Three chamber sociability test: Mice were tested for social deficits as described previously.[98] Briefly, the behavior of the animals was monitored in a rectangular three chambers arena (60cm (L) x 40cm (W) x 20 cm (H)) made of clear plexiglas. Age- and sex-matched littermate pairs were used for all tests. Sex- and age-matched C57BL/6J mice were used as "stranger" mice. Mice were habituated to the wire cage for 2x 10 min 24h before the test. During the first session (habituation), each subject was placed into the center chamber with open access to both left and right chambers, each chamber containing an empty wire cage. After ten minutes of habituation, mice were tested in the "social phase." An age-matched stranger was placed in the wire cage of the left chamber, while a novel object was placed into the right chamber's cage. The wire cage (12cm (H), 11cm diameter) allows nose contact between the test subject and the C57BL/6J strangers. The test animal was allowed to explore the arena for 10 min freely. Locomotor activity (distance traveled and velocity) and the number of nose contacts (< 5cm proximity) with the caged mouse/object were recorded and analyzed by EthoVision XT 11.5 software (Noldus). Vertical explorative behavior was assessed by manually quantifying the number of rearings during the habituation phase. Gait measurement test: Potential gait impairments were monitored using "the footprint test."[99] In brief, the fore and hind paws were painted with dyes of contrasting colors. The mouse was placed in a narrow corridor on white paper. A darkened house was used as bait to encourage the mouse to walk in a straight line. The footprint patterns were then analyzed for stride length, sway length and stance length. Hind limb clasping test: To assess potential hind limb clasping behavior, mice were suspended by their tails for 10s. During this period, the hind limb position was monitored and scored according to the severity of the phenotype.[100] The test was repeated three times for each animal.

QUANTIFICATION AND STATISTICAL ANALYSIS

Statistical analyses were performed using Microsoft® Excel® 2013, GraphPad Prism 9.0 and Origin 2018 and Python. Shapiro–Wilk test was employed to evaluate normal distribution, means and standard deviations of the given data. Parametric data were analyzed for significance using unpaired two-tailed t-tests, 1-way or 2-way ANOVAs with Sidak's post-hoc test, using $*p<0.05$, $**p<0.01$, and $***p<0.001$ for significance. Data were presented as a bar, box and whiskers, scatter dot plots and mean ± standard deviation, unless otherwise specified. Data sets with non-normal distributions were analyzed using the two-tailed Mann–Whitney U test. Enrichment analysis for metabolomics data was performed using Fisher's exact test. Where applicable, multiple testing corrections have been performed using the Benjamini-Hochberg procedure. Illustrations were prepared using Adobe Illustrator and BioRender (BioRender.com).
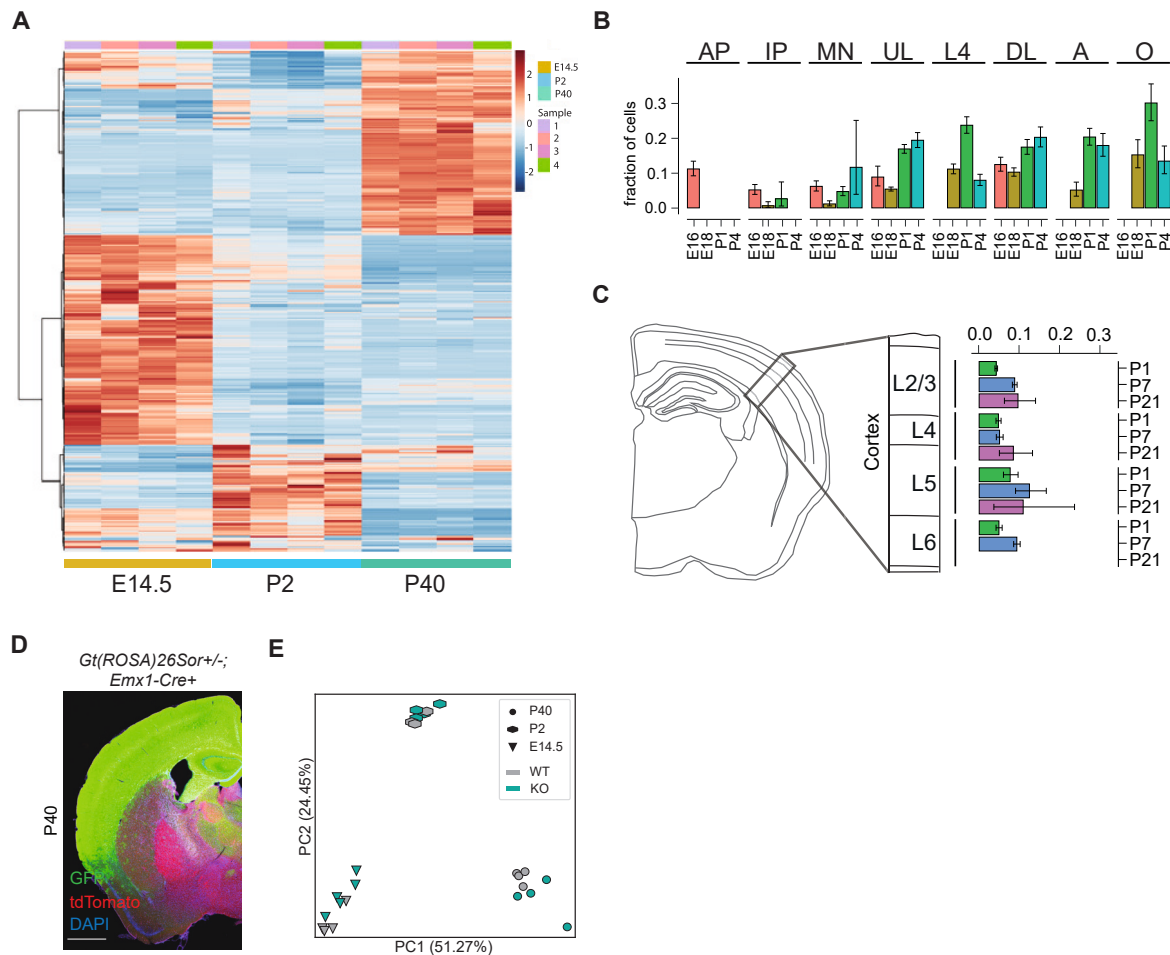
Supplemental figures

Figure S1. Untargeted metabolomic profiling of wild-type and *Slc7a5* deficient cortex, related to Figures 1 and 2

(A) Heatmap visualizing changes in metabolite levels in the wild-type cortex obtained from multiple mice at three developmental time points (E14.5, P2, and P40).

(B) *Slc7a5* expression in the murine cortex during perinatal development (E16, E18, P1, and P4); based on single-cell RNA sequencing data (DiBella et al.[72]; AP, apical progenitor; IP, intermediate progenitor; MN, migrating neuron; UL, upper layer excitatory neurons; L4, layer IV excitatory neurons; DL, deeper layer excitatory neurons; A, astrocytes; O, oligodendrocytes).

(C) *Slc7a5* expression in excitatory neurons of different cortical layers during post-natal neurodevelopment (P1, P7, and P21); based on single-cell RNA sequencing data (Yuan et al.[73]; L2/L3, layer II/III excitatory neurons; L4, layer IV excitatory neurons; L5, LV excitatory neurons; L6, layer VI excitatory neurons).

(D) *Emx1*-driven Cre recombinase expression in neural cells of the neocortex was verified by utilizing the *Gt26Sor^{mtmG}* reporter mouse line. *Gt26Sor^{mtmG};Emx1-Cre+* mice express tdTomato in all cells prior to Cre recombinase exposure. After recombination, Cre recombinase expressing cells are labeled with cell membrane-localized green fluorescent protein (GFP) (scale bar, 1,500 μm).

(E) PCA plot based on all detected metabolites of *Slc7a5* mutant and wild-type cortex at E14.5, P2, and P40.
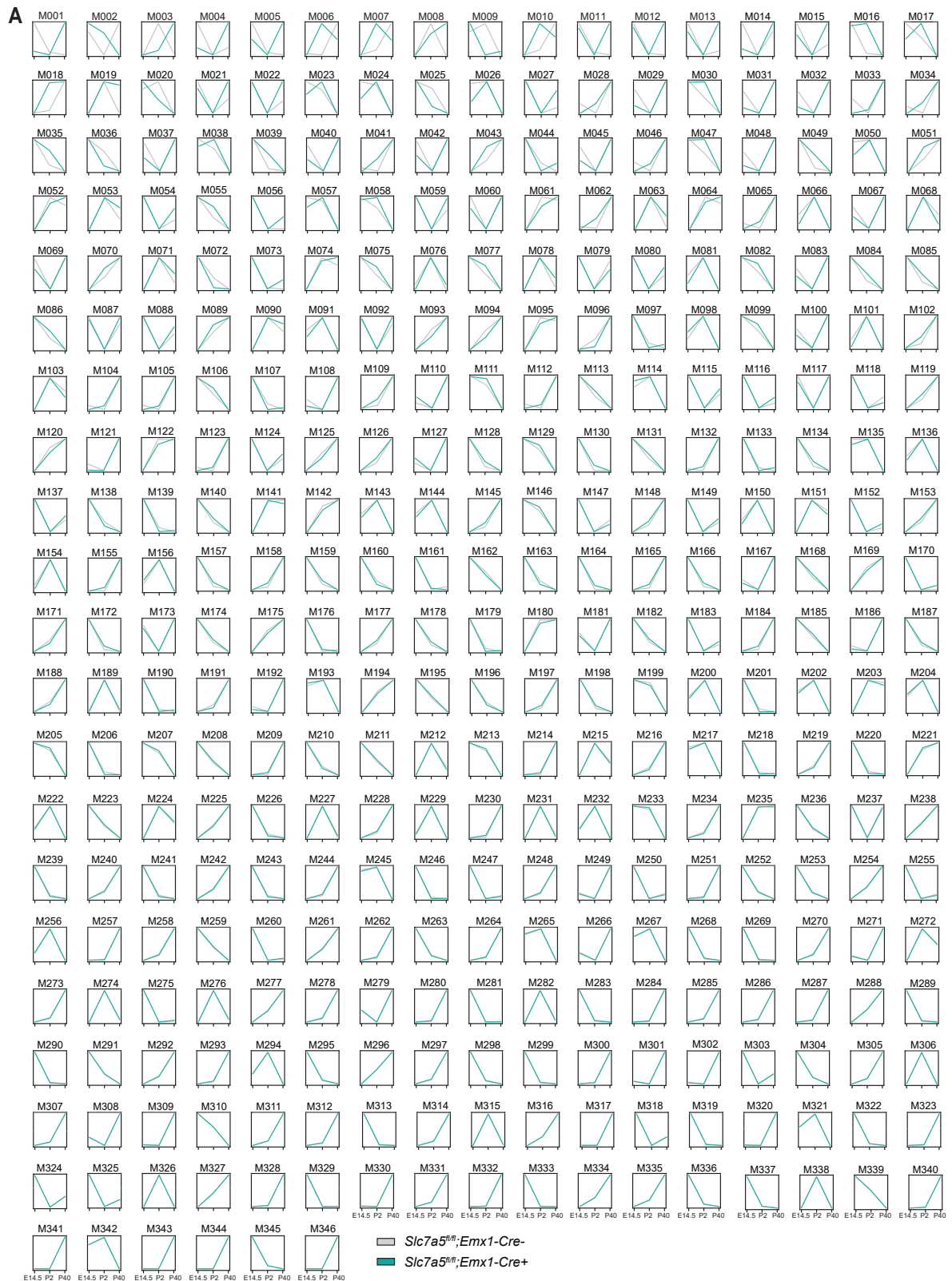
Figure S2. Developmental trajectories of metabolites detected in wild-type cortex and *Slc7a5* deficient cortex, related to Figures 1 and 2
(A) Normalized and scaled trajectories of all metabolites detected in *Slc7a5*^fl/fl^*;Emx1-Cre+* (cyan) and wild-type (gray) cortical tissue (x axis: age; y axis: scaled abundance; metabolites and Pearson's coefficient: Data S1).

Figure S3. Cellular energy homeostasis is unaffected by the loss of *Slc7a5*, related to Figure 3

(A) Volcano plot of intracellular levels of metabolic co-factors and key metabolites of ATP producing pathways (n = 7 mice per genotype; $^{ns}p > 0.05$; unpaired two-tailed t test).

(B–D) Quantification of intracellular (B) ATP (means ± SEM; n = 7 mice per genotype; unpaired two-tailed t test), (C) ATP/ADP ratio (means ± SEM; n = 7 mice per genotype; $^{ns}p > 0.05$; unpaired two-tailed t test), and (D) ATP levels over the course of development in cortical tissue of *Slc7a5^{fl/fl};Emx1-Cre+* and wild-type mice (n = 5 mice per genotype and time point; Pearson's coefficient: r > 0.9).

(E and F) Intracellular (E) NAD$^+$/NADH and (F) NADP$^+$/NADPH ratios are not changed in cortical cells of mutant mice (means ± SEM; n = 7 mice per genotype; $^{ns}p > 0.05$; unpaired two-tailed t test).

(G) The ratio of oxidized and reduced glutathione is unaffected in cortical cells of mutant mice (means ± SEM; n = 7 mice per genotype; $^{ns}p > 0.05$; unpaired two-tailed t test).

(H) PCA plot of lipid-related metabolites detected in wild-type and mutant mice over time using an untargeted metabolomics approach (n = 4 animals per genotype and time point).

(I) Protein expression (mean $\log_{10}$ expression) levels in *Emx1-Cre+* vs. wild-type cortex (n = 4 animals per genotype).

(J) GO-term enrichment analysis of upregulated genes of bulk RNA sequencing of *Slc7a5^{fl/fl};Emx1-Cre+* cortex at P2 (selected GO terms: Data S5; n = 3 mice per genotype).

(K) Comparison of the perinatal metabolic states of *Slc7a5* mutant and wild-type neurons (FA, fatty acid; KB, ketone body; OXPHOS, oxidative phosphorylation).
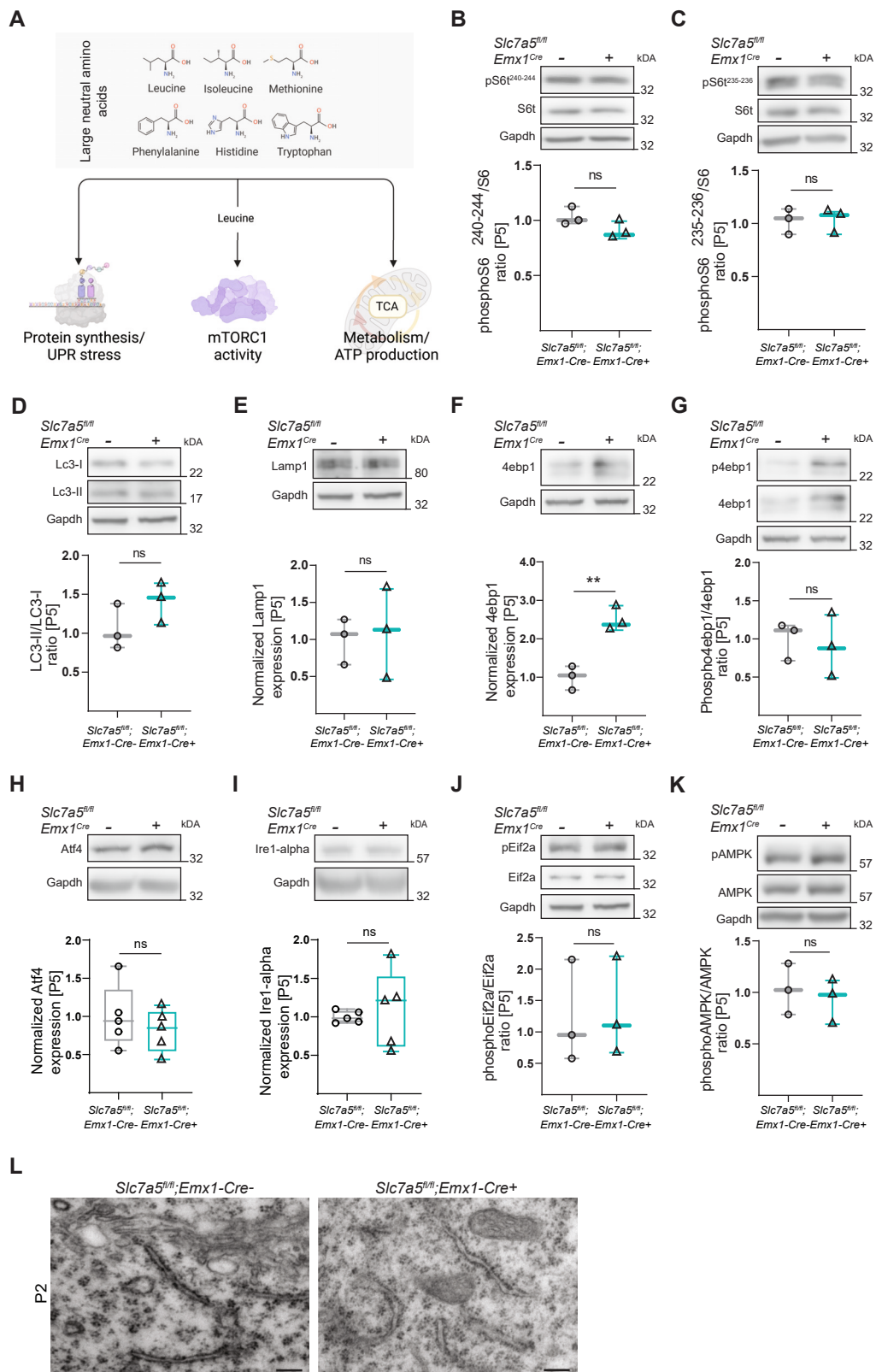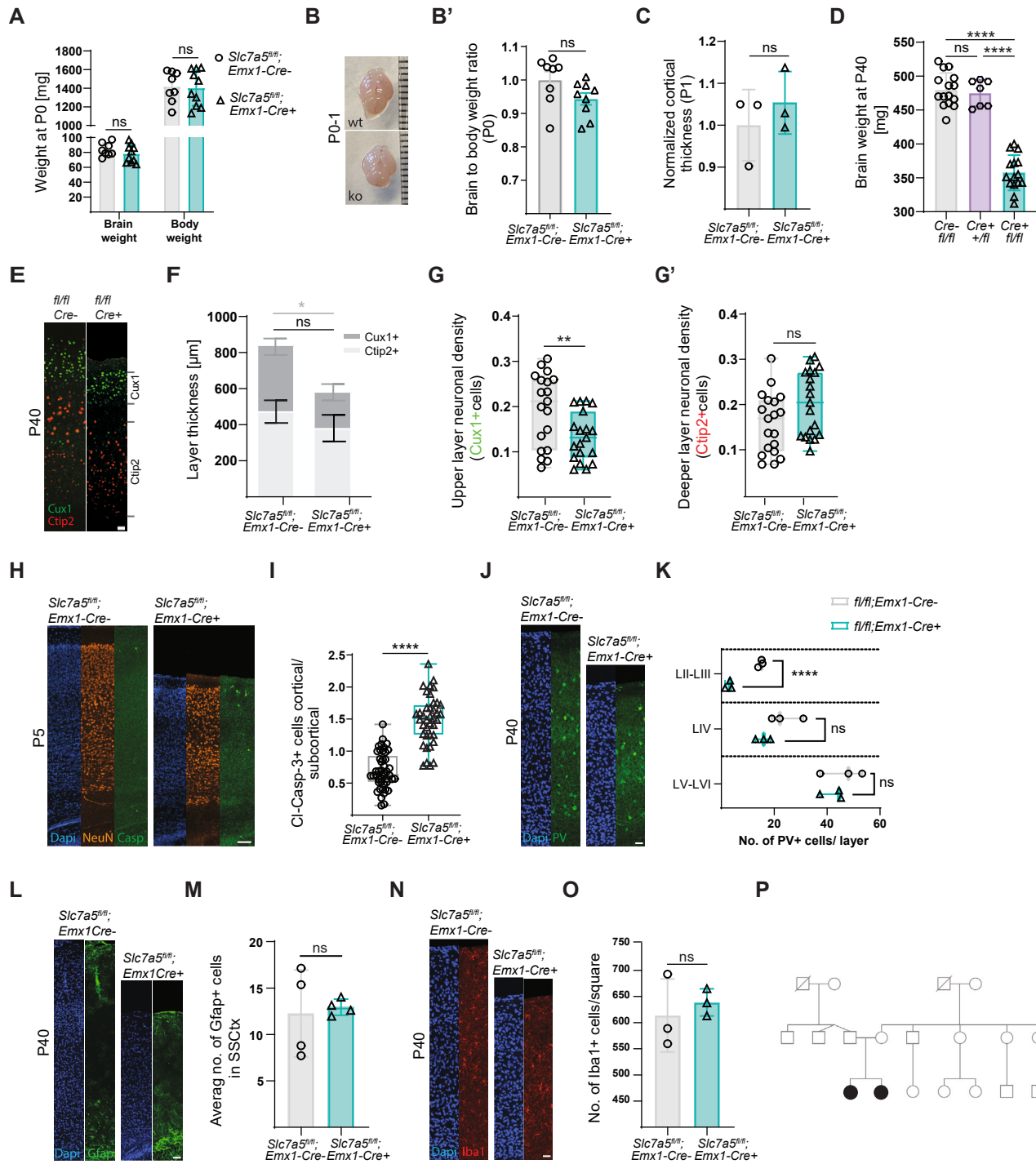
(legend on next page)

Figure S5. Characterization of the morphology and the cell-type composition of *Slc7a5*-deficient cortex, related to Figure 4

(A) Brain and body weight of newborn *Slc7a5^{fl/fl};Emx1-Cre+* and wild-type littermates (means ± SD; n = 8 animals per genotype; ^{ns}p > 0.05, unpaired two-tailed t test).

(B and B′) Images (B) and quantification (B′) of brain-to-body weight ratio of newborn (P0–P1) *Slc7a5^{fl/fl};Emx1-Cre+* and wild-type mice (means ± SD; n = 9 animals per genotype; ^{ns}p > 0.05; unpaired two-tailed t test; scale bars, 1 mm).

(C) Quantification of cortical thickness in newborn mutant and wild-type mice (means ± SD; n = 3 animals per genotype; ^{ns}p > 0.05; unpaired two-tailed t test).

(D) Brain weight of adult (P40) *Slc7a5^{fl/fl};Emx1-Cre+, Slc7a5^{fl/+};Emx1-Cre+* and wild-type littermates (means ± SD; n > 7 animals per genotype; ^{ns}p > 0.05; ****p < 0.0001; unpaired two-tailed t test).

(E) Immunostaining for upper (Cux1) and lower (Ctip2) cortical layers in adult *Slc7a5^{fl/fl};Emx1-Cre* mice (scale bars, 100 µm).

(legend continued on next page)

(F–G′) Quantification of (F) layer thickness and cell density in (G) Cux1+ or (G) Ctip2+ cell layers (means ± SD; n = 3 animals per genotype; n = 19 quantification squares for the cell density; **p < 0.01; ^{ns}p > 0.05; unpaired two-tailed t test).

(H and I) Immunostaining (H) and quantification (I) of the ratio of apoptotic cells in the cortex vs. subcortical regions of P5 mutant and wild-type mice (n = 3 animals per genotype; ****p < 0.0001; unpaired two-tailed t test; scale bars, 100 μm).

(J and K) Immunostaining (J) and quantification (K) of the number of inhibitory (parvalbumin+) neurons in the different layers of cortical columns of adult mutant and wild-type mice (n = 3 animals per genotype; ****p < 0.0001; ^{ns}p > 0.05; unpaired two-tailed t test; scale bars, 100 μm).

(L and M) Immunostaining (L) and quantification (M) of astrocytes (Gfap+) in cortical columns of adult mutant and wild-type mice (means ± SD; n = 4 animals per genotype; ^{ns}p > 0.05; unpaired two-tailed t test; scale bars, 100 μm).

(N and O) Immunostaining (N) and quantification (O) of microglia (Iba1+) in cortical columns of adult mutant and wild-type mice (means ± SD; n = 3 animals per genotype; ^{ns}p > 0.05; unpaired two-tailed t test; scale bars, 100 μm).

(P) Pedigree displays a non-consanguineous background; two affected patients (solid symbols), and unaffected members (open symbols).
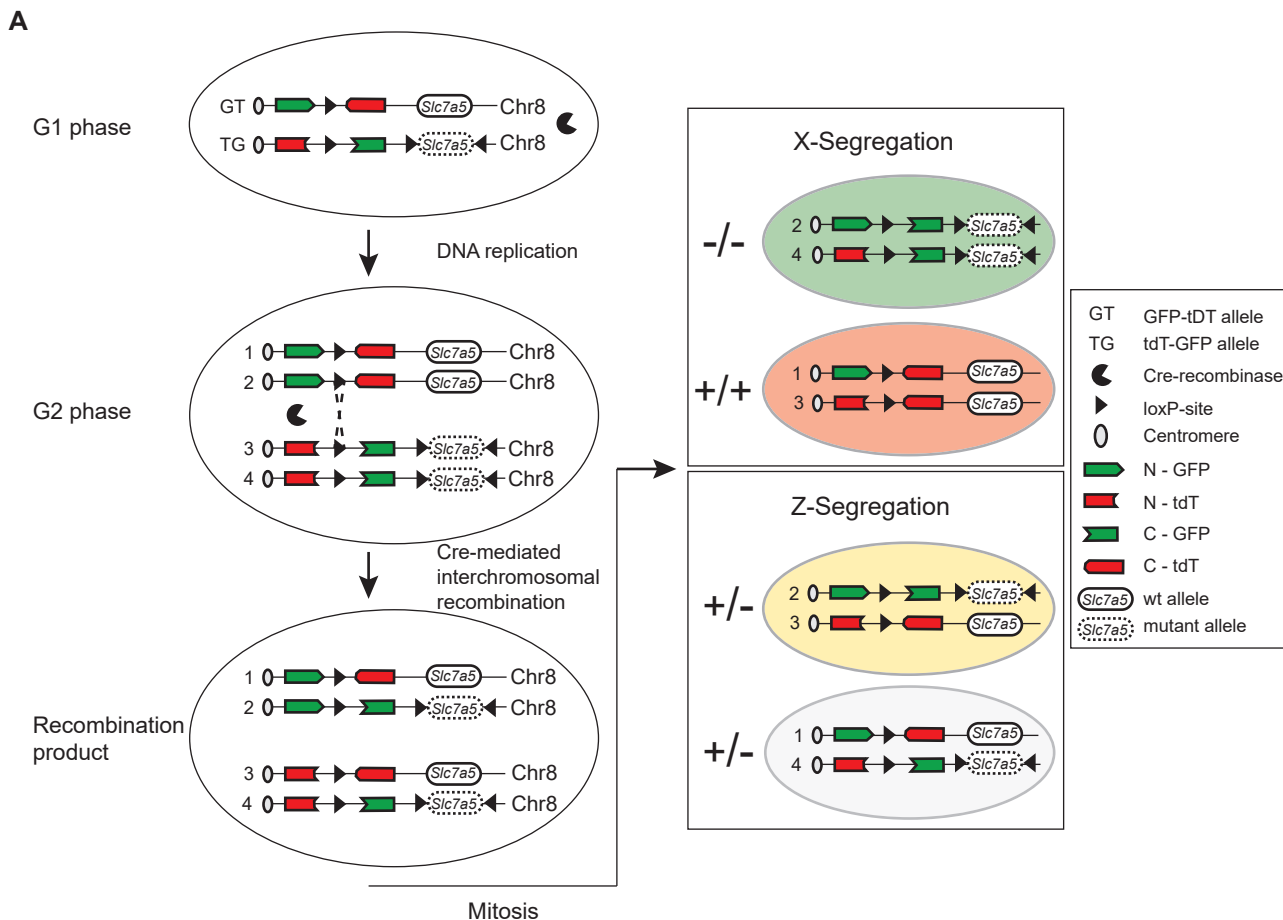
A

Figure S6. The mosaic analysis with double markers (MADM) principle, related to Figure 5

(A) Schematic of the MADM technique. Two reciprocally chimeric marker genes (MADM-8-cassettes) are inserted at two identical loci close to the centromeres distal to the *Slc7a5* gene on chromosome 8. Each cassette consists of two split coding sequences of green fluorescent protein (eGFP) and red fluorescent protein (tdTomato; cassettes are referred to as GT and TG). The N- and C-terminals of each reporter gene are separated by an intron containing a *loxP* site. This ensures that the chimeric genes do not produce functional proteins in the absence of Cre recombinase. In the presence of Cre recombinase, *cis*-recombination induces the deletion of the *floxed* exon in the *Slc7a5* gene, thereby generating a *Slc7a5* knockout. These recombination events can take place throughout all phases of the cell cycle. In G2, recombination in *trans* can mediate stochastic interchromosomal recombination events at the *loxP* sites of the MADM cassettes. This restores functional eGFP and tdTomato expression in sparse single cells. During mitosis, two potential types of chromosomal segregation can take place. X segregation generates green daughter cells homozygous for the mutation (*Slc7a5*$^{-/-}$) and red cells homozygous for the wild-type allele (*Slc7a5*$^{+/+}$), thereby creating fluorescently labeled genetic mosaic mice. Z segregation produces one daughter cell that resembles the parental cell (colorless) and a second daughter cell expressing both fluorescent proteins (double colored). Both cells are heterozygous for *Slc7a5* mutation.
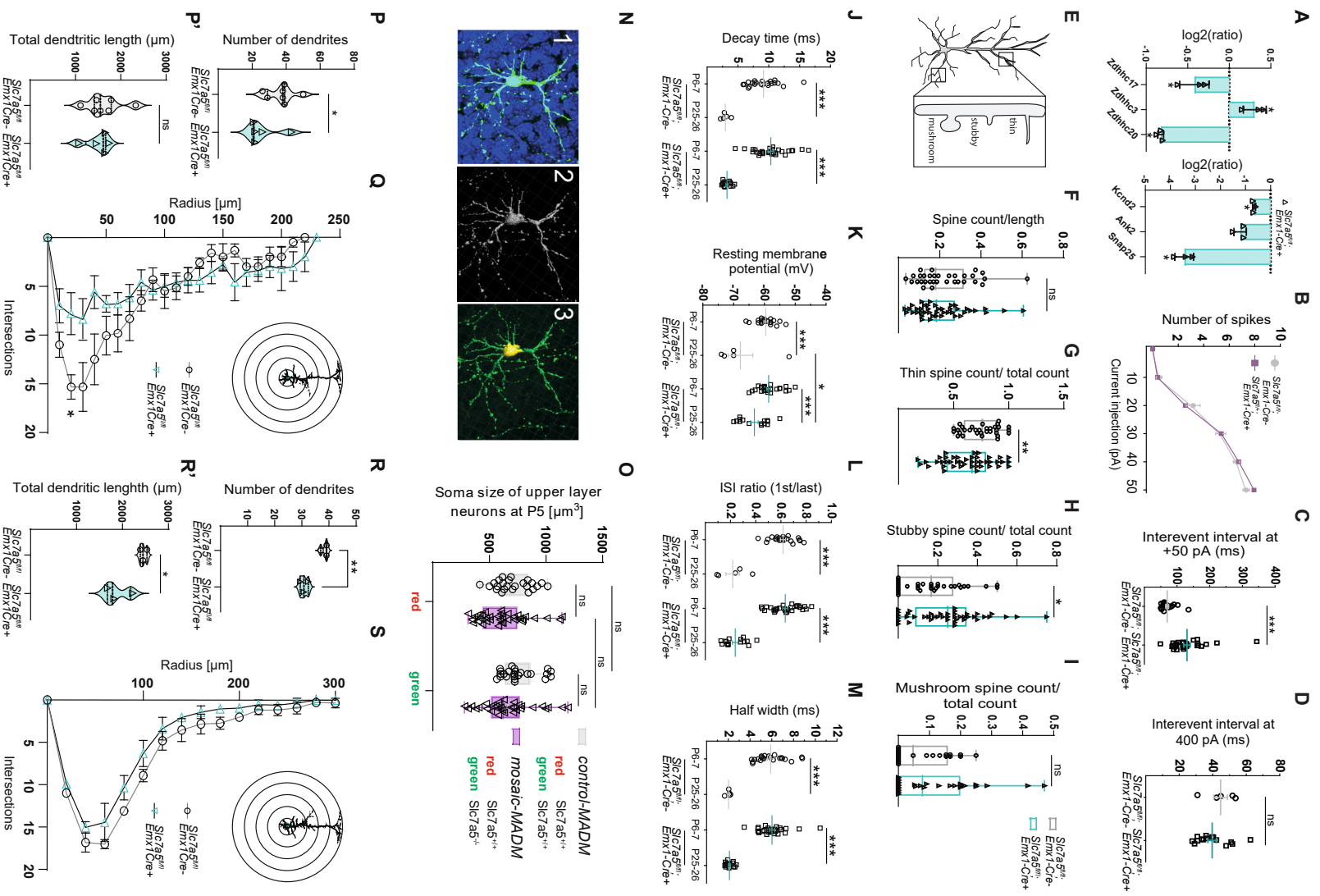
Figure S7. Electrophysiological properties of *Slc7a5^{fl/fl};Emx1-Cre* mice, related to Figure 6

(A) Fold change differences of proteins associated with the neuronal palmitoylation process of P5 *Slc7a5^{fl/fl};Emx1-Cre+* compared with *Slc7a5^{fl/fl};Emx1-Cre−* cortex (means ± SD; *significant; FDR threshold 1%, F test).

(B) Current-clamp recordings from LII/LIII pyramidal neurons in *Slc7a5^{fl/+};Emx1-Cre+* and *Slc7a5^{fl/fl};Emx1-Cre−* SSCtx at P6-P7 (*Slc7a5^{fl/fl};Emx1Cre−*: n = 12 cells/2 mice; *Slc7a5^{fl/+};Emx1-Cre+*: n = 16 cells/2 mice; two-way ANOVA: genotype $F_{(1,167)} = 0.004$; $^{ns}p > 0.5$, current step $F_{(5,167)} = 162.11$; $^{***}p < 0.001$, interaction $F_{(5,167)} = 0.6 ^{ns}p > 0.5$.

(C and D) Inter-spike interval measured in current-clamp experiments from P6 to P7 (C) and P25 to P26 (D) LII/LIII pyramidal neurons of *Slc7a5^{fl/fl};Emx1-Cre+* and *Emx1-Cre−* animals (*Slc7a5^{fl/fl};Emx1-Cre−*: n = 22 cells/3 mice; *Slc7a5^{fl/fl};Emx1-Cre+*: n = 30 cells/3 mice (P6–P7); *Slc7a5^{fl/fl};Emx1-Cre+*: n = 5 cells/3 mice; *Slc7a5^{fl/fl};Emx1-Cre−*: n = 15 cells/3 mice (P25–P26); $^{***}p < 0.001$, unpaired two-tailed t test).

(E) Different dendritic spine classes represented on pyramidal neurons (thin, stubby, mushroom).

(F–I) Analysis of the overall dendritic spine density (F) and the ratio of the different spine classes (G–I) of mutant and wild-type LII/LIII pyramidal neurons in the SSCtx at P6–P7 (n = 3 mice per genotype, n > 28 dendrites per mouse; $^{**}p < 0.01$, $^{*}p < 0.05$, $^{ns}p > 0.05$; unpaired two-tailed t test).

(J–M) Decay time (J), resting membrane potential (K), ISI ratio (L), and half width (M) are not affected perinatally (*Slc7a5^{fl/fl};Emx1-Cre−*: n = 22 cells/3 mice; *Slc7a5^{fl/fl};Emx1-Cre+*: n = 30 cells/3 mice (P6–P7); *Slc7a5^{fl/fl};Emx1-Cre−*: n = 5 cells/3 mice; *Slc7a5^{fl/fl};Emx1-Cre+*: n = 15 cells/3 mice (P25–P26). Two-way ANOVA for AP decay time: genotype $F_{(1,71)} = 1.28 ^{ns}p > 0.5$, time point $F_{(1,71)} = 107.51 ^{***}p < 0.001$, interaction $F_{(1,71)} = 0.5 ^{ns}p > 0.5$, Holm-Sidak post hoc $^{***}p < 0.001$. Two-way ANOVA for resting membrane potential: genotype $F_{(1,70)} = 4.89 ^{*}p < 0.5$, time point $F_{(1,70)} = 20.35 ^{***}p < 0.001$, interaction $F_{(1,70)} = 2.14 ^{ns}p > 0.5$, Holm-Sidak post hoc $^{*}p < 0.05$, $^{***}p < 0.001$. Two-way ANOVA for ISI ratio: genotype $F_{(1,70)} = 0.42 ^{ns}p > 0.5$, time point $F_{(1,70)} = 181.02 ^{***}p < 0.001$, interaction $F_{(1,70)} = 0.002 ^{ns}p > 0.5$, Holm-Sidak post hoc $^{***}p < 0.001$. Two-way ANOVA for half width: genotype $F_{(1,71)} = 0.08 ^{ns}p > 0.5$, time point $F_{(1,71)} = 132.15 ^{***}p < 0.001$, interaction $F_{(1,71)} = 0.002 ^{ns}p > 0.5$, Holm-Sidak post hoc $^{***}p < 0.001$).

(N and O) Soma size measurements of LII/LIII pyramidal neurons of mosaic-MADM and control-MADM mice at P5. (N) LII/LIII MADM-labeled pyramidal neurons (1, left) were 3D-reconstructed using Imaris software (2, middle), and the soma size was determined (3, right). (O) Quantification of the soma size of MADM-labeled pyramidal neurons in mosaic-MADM and control-MADM mice at P5 (mosaic-MADM: *Slc7a5^{−/−}* (green), *Slc7a5^{+/+}* (red); control-MADM: *Slc7a5^{+/+}* (green and red); n = 4 animals per genotype; n = 6 neurons per color and genotype; $^{ns}p > 0.05$; one-way ANOVA and Sidak's multiple comparison test).

(P–S) Analysis of the morphology of mutant and wild-type LII/LIII pyramidal neurons at P6–P7 (P and Q) and P40 (R and S). Quantification of (P and R) the number of dendrites, (P′ and R′) total dendritic length, and (Q and S) the number of dendritic intersections (sholl analysis; top: scheme; bottom: quantification) (n = 3 mice per genotype, at least 6 cells per animal; $^{*}p < 0.05$, $^{ns}p > 0.05$; one-way ANOVA and Sidak's multiple comparison test).